Solar Energetic Electron Spectra Observed with Solar Orbiter

Master's thesis
University of Turku
Physics
2022
B.Sc. Annamaria Fedeli
Examiners:
Prof. Rami Vainio
Dr. Nina Dresing

The originality of this thesis has been checked in accordance with the University of Turku quality assurance system using Turnitin Originality Check service.

UNIVERSITY OF TURKU
Department of Physics and Astronomy

Fedeli, Annamaria Solar Energetic Electron Spectra Observed with Solar Orbiter

Master's thesis, 87 pp.
Physics
October 2022

The Sun produces eruptive events that release protons, electrons as well as heavier nuclei (e.g. He-Fe) into the heliosphere. These particles are accelerated up to relativistic energies in at least two distinct processes, i.e., solar flares and shocks driven by coronal mass ejections (CMEs) or their interplanetary counterparts (ICMEs). Particles in the interplanetary (IP) space are known as solar energetic particles (SEP). The energy spectrum of SEPs contains the footprint of the acceleration process. The spectrum can, however, be disrupted by transport effects.

In this thesis we study the energy spectrum of solar energetic electrons (SEE) measured by the Energetic Particle Detector (EPD) on board the Solar Orbiter (SolO) spacecraft. We use the orthogonal distance regression (ODR) to fit the spectrum of 43 SEE events observed between November 2020 and March 2022. We fit the spectrum with four different mathematical models used in previous studies: a single power-law, a single power-law with an exponential cutoff, a broken power-law and a broken power-law with an exponential cutoff. We then choose the best model to describe each event.

The broad energy range of EPD (25-475 keV) allows us to conduct a detailed analysis of the spectra and investigate the possible presence of separate spectral breaks and their relationship to two specific transport effects, for example Langmuir wave generation and pitch-angle scattering. In order to study whether the SEE spectra have more than one break we employ an indirect method of restricting the energy range used in the fits to the separate instruments or combinations of instruments of EPD. The combinations of instruments used in our analysis are STEP (2-80 keV), EPT (25-475 keV), STEP+EPT (2-475 keV) and EPT+HET (25 keV-30 MeV). We compare our results to previous observational and modeling studies that discuss the presence and underlying mechanism of different spectral breaks.

We found strong evidence of the presence of two distinct spectral breaks at $\sim 20 \pm 13.2$ keV and $\sim 70.0 \pm 30.5$ keV. We also found evidence that the lower energy spectral break is caused by Langmuir wave generation. We could not, however, find the expected dependencies for the higher break in terms of pitch-angle scattering.

Keywords: Solar Energetic Particles, Solar Energetic Electrons, Energy Spectra, Spectral Break, Spectral Index, Transport Effects, Pitch-Angle Scattering, Langmuir Wave Generation.

Contents

1 Introduction **2**

2 Theoretical Background **5**

2.1 Solar Energetic Particle Spectra 5

2.2 The Effects of Transport on Energetic Particle Spectra 7

3 Methodology **13**

3.1 The Solar Orbiter Mission 13

3.1.1 The Energetic Particle Detector 15

3.2 Event Selection 16

3.3 Determining and Fitting a Peak Intensity Spectrum 19

3.3.1 Finding the Intensity Peak 20

3.3.2 Fitting the Energy Spectra 27

4 Data Analysis **33**

4.1 Unexpected Hardening of the Spectra 33

4.2 Searching for Different Spectral Breaks 34

4.3 Intensity Offset Between STEP and EPT 38

4.4 Selection of the Best Time Averaging 40

5 Results **44**

6 Discussion and Conclusion **54**

7 Outlook **59**

References **61**

Appendix A **72**

Appendix B **75**

Abbreviations

au Astronomical Unit

CME Coronal Mass Ejection

DOF Degrees Of Freedom

EPD Energetic Particle Detector

ESA European Space Agency

EPT Electron Proton Telescope

HET High Energy Telescope

HXR Hard X-Ray

ICME Interplanetary Coronal Mass Ejection

IP Interplanetary

NASA National Aeronautics and Space Administration

ODR Orthogonal Distance Regression

RS Solar radius

SEE Solar Energetic Electron

SEP Solar Energetic Particle

SEPT Solar Electron and Proton Telescope

SolO Solar Orbiter

STEP Supra Thermal Electrons and Protons sensor

STIX Spectrometer/Telescope for imaging X-rays

1 Introduction

The Sun produces eruptive events that release particles into the heliosphere and accelerate them in at least two processes, i.e., solar flares and shocks driven by coronal mass ejections (CMEs) or their interplanetary counterparts (ICMEs). These energetic particles (i.e., protons, electrons and heavier ions) in the interplanetary (IP) space are known as solar energetic particles (SEP) and the processes that accelerate such particles are known as solar energetic particle events (e.g. Reames, 2013; Desai and Giacalone, 2016; Miteva et al., 2017; Bruno et al., 2019). SEP events are distinct into two main categories: impulsive and gradual. Impulsive SEP events accelerate particles as a result of reconnection in solar flares in the low corona and are associated with short time scales, while gradual SEP events accelerate particles over large angular extents in near-Sun CME-driven shocks, are generally long-lasting and have larger fluences (the time integral of flux) (Masuda et al., 1994; Reames, 1999, 2013; Desai and Giacalone, 2016; Vlahos et al., 2019; Chiappetta et al., 2021). This is shown in the intensity time profile of Figure 1 as a low, gradual and long lasing rise. On the other hand, impulsive SEP events last only a short period of time (see intensity-time profile in Figure 1).

During the early observations of SEP event it was believed that solar flares were their sole source. This assumption, along with later observations, lead to the formation of a phenomenon known as the solar flare myth (Gosling, 1993; Reames, 1999). Later findings of a possible close association between SEP events and type II and IV radio bursts lead to a new theory according to which SEPs could also be accelerated by shock waves that accompany the solar flares (e.g. Wild et al., 1963; Lin, 1970; Desai and Giacalone, 2016). The two-phase acceleration process, however, took years to be accepted by the scientific community and only after detailed multi-spacecraft analysis of flares and their association to radio bursts, researchers started welcoming the two-class theory (Gosling, 1993; Reames, 1999; Desai and Giacalone,

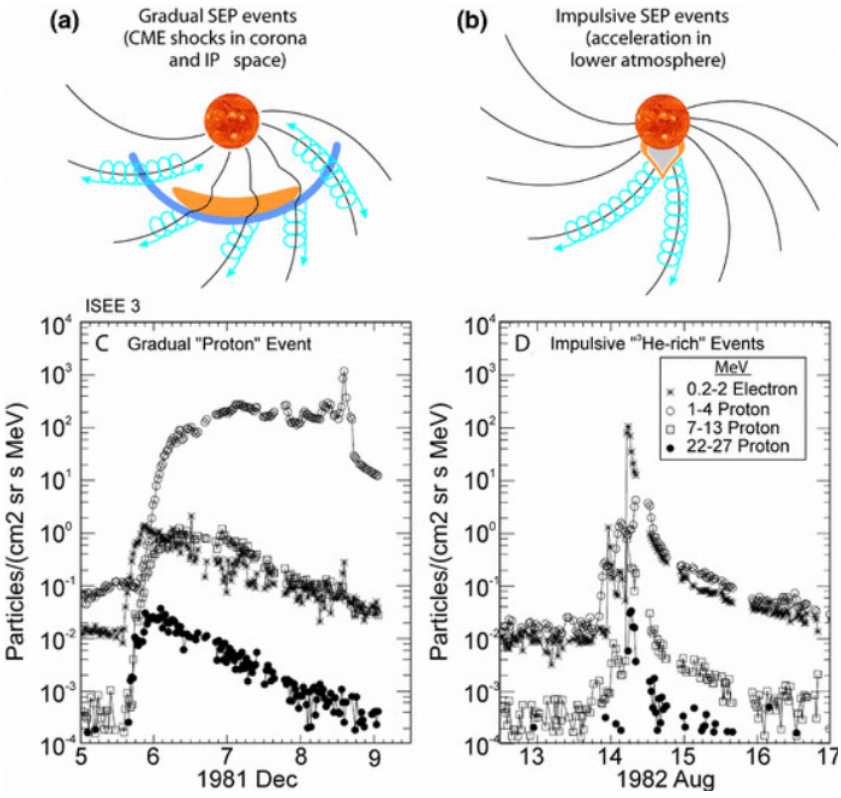

Figure 1. The historical two-class picture of SEP events showing the difference between gradual and impulsive SEP events. On the top right (a) an illustration of an event with wide angular extent associated with CME-driven shocks. Below this, the flux time profile with a long lasting gradual rise. On the top left (b) the illustration of a flare-associated event. This type of event requires a magnetic connection to the source in order to be seen because of its limited angular range. Below, the time profile of such event with a clear limited time extent. (Reames, 1999)

2016). And so, the historical two-class picture had emerged (see Figure 1).

Furthermore, flare related events were believed to be the primary acceleration mechanism for solar energetic electrons (SEE) whereas ions were believed to be primarily accelerated by CME-driven shocks (Cane et al., 1988; Masuda et al., 1994; Reames, 1999; Barnard and Lockwood, 2011). It is, however, challenging to make a clear distinction between flare-accelerated particles and particles accelerated by CME-driven shocks, as most gradual SEP events are also associated with an impulsive part (Vlahos et al., 2019). Figure 2 illustrates the close association between the reconnection region of flares and the CME-driven shocks that produce type II radio bursts (Cliver et al., 2004; Kahler, 2007).

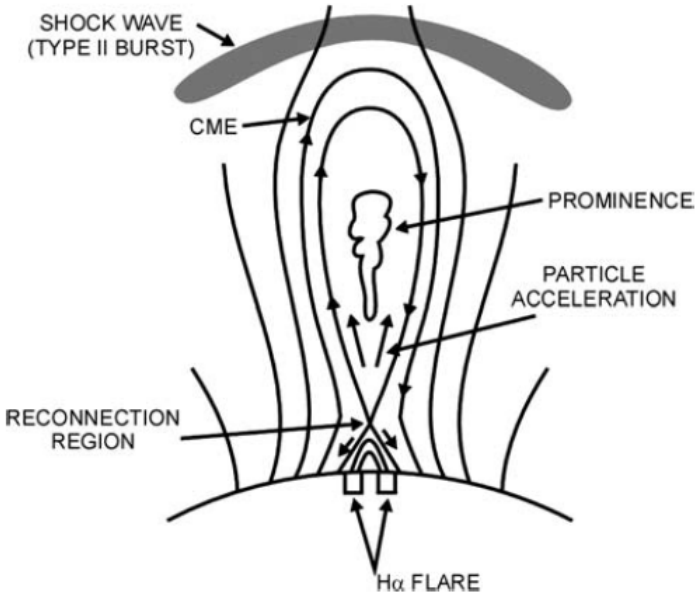

Figure 2. Illustration showing the close association between the reconnection region of flares and the CME-driven shocks that produce type II radio bursts. Electrons are accelerated in the flare region over short time scales. (Cliver et al., 2004; Kahler, 2007)

The role of CME-driven shocks in accelerating SEEs is still under debate. Nevertheless, their ability to accelerate electrons to a few keV is demonstrated by the presence of type II radio bursts (Aschwanden, 2002; Krucker et al., 2010; Guo and Giacalone, 2012; Laurenza et al., 2016; Dresing et al., 2022). The small and large

extents of SEP events are not yet clearly associated with the extent of the source region. During widespread events, it is also hard to disentangle whether the wide particle spread is caused by the field line spread close to the Sun, i.e., the injection process, acceleration or transport effects (Dresing et al., 2014; Gómez-Herrero et al., 2015; Kouloumvakos et al., 2015; Lario et al., 2016; Dresing et al., 2018; Mann et al., 2018; Dresing et al., 2021). There are still many unknowns in terms of the underlying acceleration process, but thanks to the new and highly sophisticated technologies of recently launched missions, such as Solar Orbiter, we are on our way to shed more light on this.

2 Theoretical Background

2.1 Solar Energetic Particle Spectra

When we talk about particle energy spectra, we refer to intensity as a function of energy (see Figure 3). During an SEP event particles are injected into the interplanetary space and their intensity or flux can be measured by a spacecraft for different energies. For each energy channel of an energetic particle detector we can measure a corresponding intensity for a certain particle population. A particle energy spectrum can be determined in various ways either by integrating the intensity over the whole duration of the event (fluence spectrum), by taking the intensity at a specific time or by taking the peak intensity at each energy channel. The energy spectrum is the collection of these intensities as a function of the corresponding energy. The intensity peak at different energies is not expected to happen at the same time. Due to velocity dispersion, particles at lower energies can be delayed by minutes or even hours compared to the higher energy particles (Lin et al., 1995).

The characteristics and variability of SEP energy spectra can provide important information about the acceleration processes involved (Klein and Trottet, 2001; Vla-

hos et al., 2019). Typically an SEP spectrum is associated with a power-law shape. Ellison et al. (1985) argued that the power-law spectrum of protons accelerated by a shock should have an exponential cutoff at high energies caused by an increasing diffusion coefficient. The diffusion coefficient used by Ellison et al. (1985) was inferred from observations of interplanetary shock acceleration (e.g. Ellison, 1981; Ellison and Eichler, 1984). Cohen et al. (2005) argued that the presence of this rollover or spectral break in fluence spectra should depend on the type of diffusion process. Generally, the shapes of fluence spectra and peak intensity spectra are similar and the power-law indices agree within 0.2 (Krucker et al., 2007). Mewaldt et al. (2012) found that the fluence spectrum of energetic protons does in fact present a break and a double power-law is more suitable to represent it (see Figure 3). The term spectral break implies a sudden change in spectral index. This, however, can be misleading as the change in spectral index can be quite smooth at times (Strauss et al., 2020). The relationship between the steepening of the spectrum and the physics of the shock remains still unclear (Mewaldt et al., 2013; Vlahos et al., 2019). It is also unclear whether shocks accelerate electrons up to higher energies and what the energy spectrum of such acceleration process should look like (Yu et al., 2022). The energy spectrum contains the footprint of the acceleration process. The spectrum can however be disrupted due to a variety of effects such as transport effects (Laurenza et al., 2016; Mewaldt et al., 2005; Dresing et al., 2021; Fraschetti, 2021).

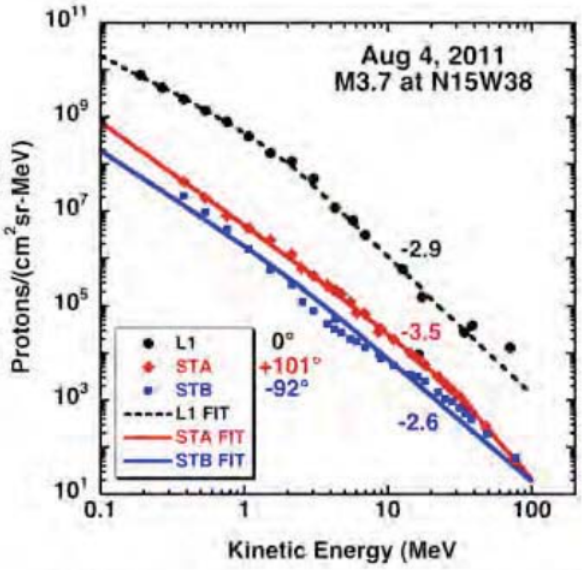

Figure 3. Example of proton fluence spectrum from Mewaldt et al. (2013) with a double power-law fitting function from Band et al. (1993).

2.2 The Effects of Transport on Energetic Particle Spectra

Investigating the transport of SEPs and more specifically solar energetic electrons (SEE) in the heliospheric plasma is important in order to understand the role that these effects have on observed spectra and spectral properties (Kontar and Reid, 2009; Strauss et al., 2020). These effects can make the distinction between acceleration processes and transport effects extremely challenging (Laurenza et al., 2016; Dresing et al., 2021).

Solar flares are known to efficiently accelerate electrons and the spectrum of the accelerated SEEs usually displays double power-law shape with a spectral softening after the break (Krucker et al., 2009; Kontar and Reid, 2009; Desai and Giacalone, 2016). The spectrum of SEEs is comparable to hard X-ray (HXR) spectra. Both are characterized by double power-law shape and display spectral breaks at similar energies. It is also commonly accepted that HXR spectra contain the footprint of the acceleration mechanism (Kontar et al., 2002; Krucker et al., 2009; Dresing et al., 2021). This correlation is often viewed as support to the theory that electrons

propagate scatter-free to 1 astronomical unit (au) (Wang et al., 2006). Krucker et al. (2009) argue that, although it might be true that these spectral breaks are a direct reflection of the acceleration mechanism of SEEs, we cannot rule out the possibility of other processes being involved. Energy dependent transport effects, such as Langmuir waves, could significantly distort the observed electron spectrum (Kontar, 2001). Krucker et al. (2009) studied the spectral shapes of SEE events measured by the Wind spacecraft between 1 and 300 keV. They found that the majority of the SEE spectra displayed a double power-law shape. The mean energy of the spectral breaks was $\sim$ 60 keV. Figure 4 shows the distribution of the break energies found in the study.

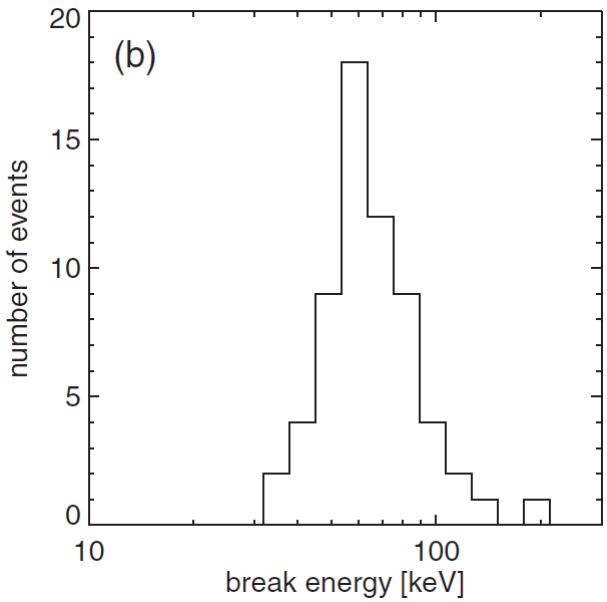

Figure 4. Histogram of the break energies in the 2009 statistical survey of 62 SEE events. (Krucker et al., 2009)

On the one hand, the close association between the spectral indices of in situ observed SEE spectra and HXR spectra points towards the scatter-free propagation theory, but on the other hand, the close association of such events to Type III radio bursts suggests otherwise, as an electron beam can excite Langmuir waves (Ginzburg and Zhelezniakov, 1958; Lin et al., 1981; Kontar, 2001; Gosling et al.,

2003; Cane, 2003; Ledenev et al., 2004). Kontar and Reid (2009) studied the effects of electrostatic electron plasma waves (i.e., Langmuir waves) on the propagation of solar energetic electrons via modeling. They found that for an injected single power-law spectrum the overall observed spectrum was closer to a broken power-law. The lower energy electrons below the break energy do not propagate freely but are rather limited by the generation and absorption of Langmuir waves. This results in a harder spectrum below a certain energy where the particle-wave interactions are important and cause energy loss in the lower energy electrons. In the study, Kontar and Reid (2009) found that for all the simulations the break energy ranged between 4 keV and 80 keV, which is consistent with the observational results found by Krucker et al. (2009). So, the 60 keV break could be explained by Langmuir wave generation. Figure 5 shows an example of a modelled SEE spectrum with a break caused by Langmuir wave generation found by Kontar and Reid (2009). Kontar and Reid (2009) also found that the break energy and the respective fluence at the break energy are clearly correlated. This dependence is shown in Figure 6. They argue that this correlation should be present in case the break is caused by Langmuir wave generation. The energy loss caused by the transfer of energy from the electrons to the Langmuir waves is what causes the break in the spectrum. They also mention this correlation should be taken with care, since the break energy depends on various factors such as the spectral index of the injected solar electrons.

Another statistical study that analyzed the SEE spectra was conducted by Dresing et al. (2020) using STEREO observations. The electrons were measured between 45 and 425 keV and the break energy found in this study, $\sim$ 120 keV, was significantly higher compared to the previous results of $\sim$ 60 keV found by both Krucker et al. (2009) and the simulations done by Kontar and Reid (2009). The break energy is, however, similar to the results found by Lin et al. (1982). The distribution of the break energies found by Dresing et al. (2020) are shown in Figure

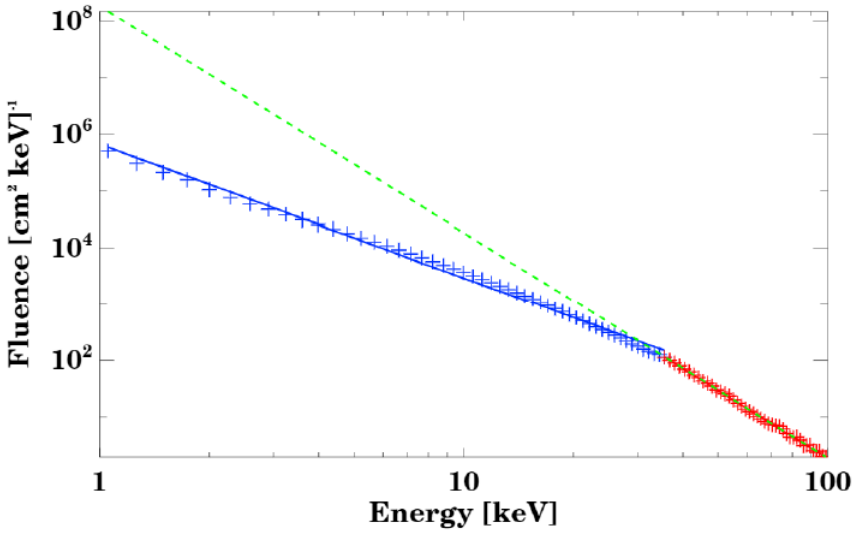

Figure 5. Example of an SEE spectrum with a break caused by Langmuir wave generation by Kontar and Reid (2009).

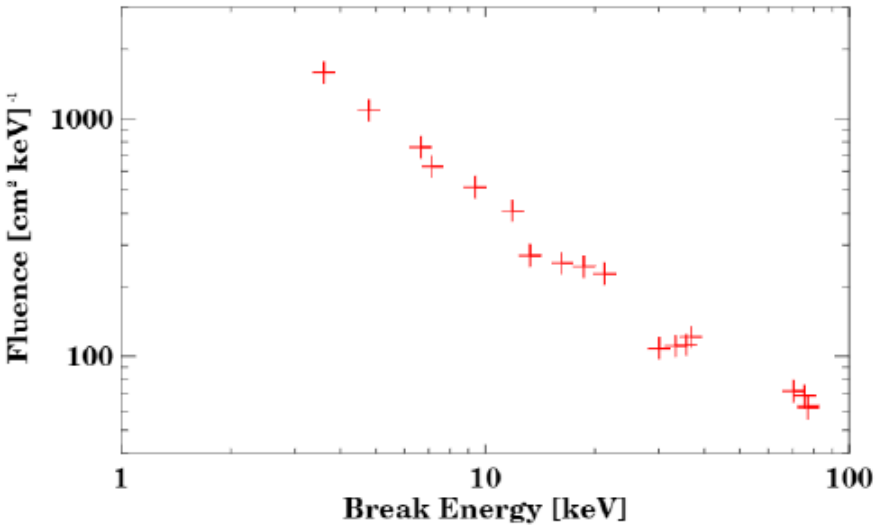

Figure 6. Example of the dependence between the fluence at the break energy and the break energy of an SEE spectra with a spectral break caused by Langmuir wave generation. (Kontar and Reid, 2009)

7.

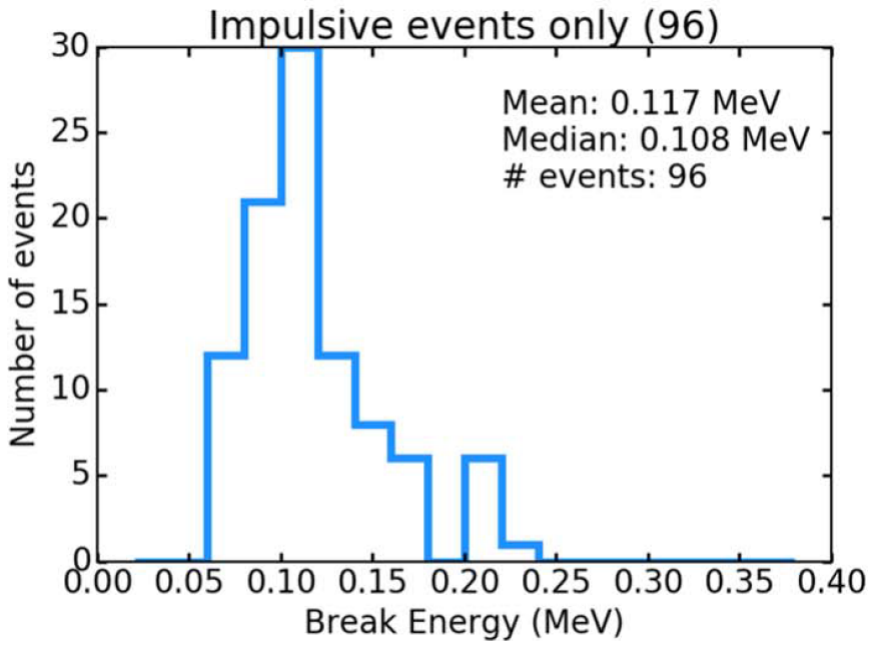

Figure 7. Histogram of the break energies in the 2020 statistical study of impulsive events observed with STEREO/SEPT. Dresing et al. (2020)

As suggested by Kontar and Reid (2009), if a spectral break is caused by Langmuir wave generation, there should be an anti-correlation present between fluence at the break break energy and the break energy itself. No such anti-correlation was found by Dresing et al. (2020). The lack of such correlation could mean that another effect is responsible for the spectral break at higher energies. Dresing et al. (2020) pointed out that the energy range the Solar Electron and Proton Telescope (SEPT) makes it impossible to detect spectral breaks below 70 keV and so, limits the position of the break to higher energies. This makes unclear whether the higher energy spectral break actually corresponds to a possible second break.

Strauss et al. (2020) studied the effects of pitch-angle scattering on the spectrum of the same sample of events as Dresing et al. (2020) through modelling. In their study, Strauss et al. (2020) focused on the energies above the spectral break and neglected the energy-loss processes that affected the lower energy part of the spectra ($<$60 keV) in the study conducted by Kontar and Reid (2009). Strauss et al. (2020)

studied their transport model for various spacecraft distances from the Sun and different energies. They found that for smaller distances ($<$ 1 au) and energies below 100 keV, the originally injected spectra remains the same. On the contrary, at higher energies and 1 au when pitch-angle scattering becomes significant, this manifests as a spectral break. Observational results by Dröge et al. (2018) also confirmed that lower energies suffer little pitch-angle scattering.

Strauss et al. (2020) point out that, for SEE spectra, since the lower energy particles below 60 keV suffer energy losses due to Langmuir wave generation and higher energy particles above 100 keV are affected by pitch-angle scattering, the energy spectrum in between these energies should be the most accurate reflection of the acceleration mechanism involved. Figure 8 illustrates an energy spectrum with two spectral breaks, where the middle part would be the least affected by transport effects (Dresing et al., 2021).

In practice this distinction is not so straightforward. If we compare the distributions of the break energies found by Krucker et al. (2009) and Dresing et al. (2020) shown in figures 4 and 7 we can clearly see that the energy range where the breaks occur do overlap. This can make it fairly difficult to distinguish between breaks that may be caused by Langmuir wave generation and pitch-angle scattering.

In situ measurements of SEEs are essential to study and understand SEP transport, acceleration and injection (Dresing et al., 2021). Recently launched space missions such as Solar Orbiter (SolO) will allow us tackle these questions thanks to its large energy range and varying distance from the Sun.

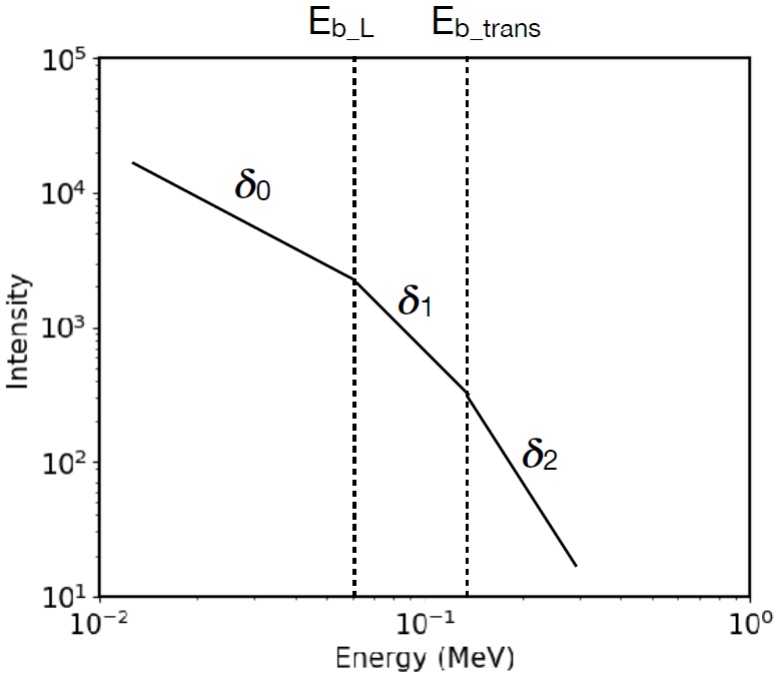

Figure 8. Illustration of an energy spectrum with two spectral breaks. The part of the spectrum below the first break suffers from energy loss by Langmuir wave generation, while the part of the spectrum above the second break is affected by pitch-angle scattering. The middle part is the least affected by transport effects. (Dresing et al., 2021)

3 Methodology

3.1 The Solar Orbiter Mission

In this thesis we will be using data from the Energetic Particle Detector (EPD) on board the Solar Orbiter (SolO) spacecraft. Solar Orbiter is a Sun-observing spacecraft developed by the European Space Agency (ESA) in collaboration with National Aeronautics and Space Administration (NASA) designed to obtain detailed in situ measurements of the plasma properties, electromagnetic fields and energetic particles in the inner heliosphere (Müller, D. et al., 2020). SolO makes observations of the Sun from a varying eccentric orbit moving as close as $\sim$ 60 solar radii (RS) to the Sun, or 0.284 au (Müller, D. et al., 2020). During the mission the orbital inclination will be raised to about 24° (Müller, D. et al., 2020). The close distance to

the Sun will make the measurements less distorted by transport effects (Rodríguez-Pacheco et al., 2020).

Solar Orbiter combines in situ measurements with high-resolution remote-sensing observations of the Sun to resolve some of the most fundamental science questions in the field (Müller, D. et al., 2020). These include investigating the sources of the solar wind, the causes of eruptive releases of plasma and magnetic field from the Sun, often in the form of CMEs, the evolution of CMEs and their interaction with the ambient solar wind flow, and the origins, acceleration mechanisms, and transport of solar energetic particles that will advance our understanding of their spectral properties (Rodríguez-Pacheco et al., 2020).

The in situ instruments that provide combined measurements include the Energetic Particle Detector (EPD; Rodríguez-Pacheco et al., 2020), the Magnetometer (MAG; Horbury et al., 2020), the Radio and Plasma Wave analyser (RPW; Maksimovic et al., 2020) and the Solar Wind Analyser (SWA; Owen et al., 2020). The remote-sensing instrumentation includes the Polarimetric and Helioseismic Imager (PHI; Solanki et al., 2020), the X-ray Spectrometer (STIX; Krucker et al., 2020), the Extreme Ultraviolet Imager (EUI; Rochus et al., 2020), the Spectral Imaging of the Coronal Enviroment instrument (SPICE; Anderson et al., 2020), the Visible light and ultraviolet coronal imager (METIS; Antonucci et al., 2020) and the Heliopheric Imager (SoloHI; Howard et al., 2020).

The combination of in situ and remote-sensing observations is one of the key features of SolO. In particular the combination of EPD (Rodríguez-Pacheco et al., 2020) and STIX (Krucker et al., 2020) allows for a comparison between the electron spectrum observed in situ and the electron spectrum at the solar flare inferred from X-ray measurements (Krucker et al., 2007). This is one of the main research topics of the combined STIX and EPD working group to which this thesis will contribute. The EPD (see Section 3.1.1) onboard Solar Orbiter is a suite of multiple sensors,

which measure particle intensities over a wide range of energies (from suprathermal to relativistic energies) and for different species (e^-, protons, and heavy ions) in different directions (Carcaboso-Morales et al., 2021). STIX is a hard X-ray imaging spectrometer, which covers the energy range from 4 to 150 keV. STIX observes hard X-rays bremsstrahlung emissions from solar flares and provides diagnostics of the hottest ($\geq$ 10 MK) flare plasma while quantifying their location, spectrum and energy content of flare accelerated non-thermal electrons.

3.1.1 The Energetic Particle Detector

The Energetic Particle Detector (EPD) is an instrument suite comprising different sensors that measure the properties of electrons and protons from suprathermal energies up to low-energy galactic cosmic rays with high temporal resolution up to 1 s. These measurements are performed over a partially overlapping energy range. EPD consists of the following units: The SupraThermal Electrons and Protons (STEP) sensor, the Electron Proton Telescope (EPT), the High Energy Telescope (HET), the Suprathermal Ion Spectrograph (SIS), and an Instrument Control Unit (ICU). The lower energy ions and electrons are covered by STEP and EPT, while HET measures the high energy range. (Rodríguez-Pacheco et al., 2020; Müller, D. et al., 2020; Wimmer-Schweingruber et al., 2021)

In this thesis we will be using STEP, EPT and HET electron data. STEP measures electrons at supra-thermal energies (2-100 keV) (Mueller et al., 2008; Rodríguez-Pacheco et al., 2020). The gap between the low-energy particles measured by STEP and the high-energy particles measured by HET, is covered by the EPT that measures electrons between 40 keV and 400 keV (Rodríguez-Pacheco et al., 2020). Its detection principle is similar to previous missions such as the SEPT sensor on board STEREO. The EPT is integrated together with HET and consists of two double-ended telescopes, one pointing sunward and anti-sunward along the nominal

Parker spiral and the other pointing southward and northward (Rodríguez-Pacheco et al., 2020). HET covers the high energy range and measures electrons between 300 keV and 15 MeV (Rodríguez-Pacheco et al., 2020). STEP does not directly measure electron flux. In order to get the electron count rate, the data needs to go through a subtraction method (Rodríguez-Pacheco et al., 2020).

Table I summarizes the key electron measurement capabilities and data products of STEP, EPT and HET. The table includes important information such as the cadence of the data, the number of energy channels for each instrument as well as the number of fields of view and their energy ranges.

Table I. Summary of key EPD measurement capabilities for electrons for STEP, EPT and HET.

	STEP	EPT	HET
Energy range	2-80 keV	25-475 keV MeV	0.3-30 MeV
# of FoVs	1 (15 sectors)	4 (sunward, anti-sunward, north, south)	4 (sunward, anti-sunward, north, south)
FoV size per aperture	$28° \times 54°$	$30°$	$54°$
Geometric factor [cm^2sr]	8×10^{-3}	0.01	0.27
Max. time resolution	1 s	1 s	1 s
# of energy channels	48	34	4

3.2 Event Selection

The event selection for the analysis in this thesis is based on a combined event list of EPD and STIX on board the SolO spacecraft.

The main criteria for the event list, compiled by a dedicated working group, is an observed SEP event in EPD and a corresponding flare observed in STIX. The

overall goal will be to compare EPD and STIX spectra to learn about the acceleration and transport effects of SEPs and understand their connection and effect on SEP spectra. Numerous studies in the past have investigated the correlation between spectral characteristics of hard X-ray spectra and in situ observed spectra and have found correlations of as high as 0.8 between the two (Kahler, 2007; Miteva et al., 2017; Dresing et al., 2021). These past studies have been limited by energy range and energetic particle instrument resolution (Lin et al., 1982; **?**; Krucker et al., 2009; Dresing et al., 2021). SolO may help solve these limitations.

Instrumental issues regarding STEP, EPT and HET have also been taken into account during event selection. Although most of the analysis in this thesis was done by excluding the first HET channel, which was clearly not following the trend of the rest of the data and is known to suffer from issues with preliminary calibration, we later decided that it is best not to use HET data before October 12th 2021 due to connection and instrumental issues. The instrument team uploaded a patch with a new calibration to fix the aforementioned issues. We use solo-epd-loader (`https://github.com/jgieseler/solo-epd-loader.git`) to download the data from Solar Orbiter's archive (SOAR, `http://soar.esac.esa.int/soar/`). The EPD team changed the data product of STEP after October 2021 and the loader is not yet updated towards this. Thus, we do not use STEP data after this date.

Table II includes the 43 events that have been used in the analysis along with an approximate peak time of each event.

Table II. The table shows the event number as well as the date and an approximate peak time of the 43 events used in the analysis.

Event Number	Event Peak Time	Event Number	Event Peak Time
1	2020-11-17 09:32	23	2021-09-28 06:23
2	2020-11-17 18:26	24	2021-10-09 06:33
3	2020-11-18 13:14	25	2021-10-28 15:26
4	2020-11-18 14:15	26	2021-11-01 01:28
5	2020-11-19 05:48	27	2021-11-09 16:39
6	2021-02-15 13:11	28	2021-12-04 05:01
7	2021-03-05 16:15	29	2021-12-04 13:13
8	2021-04-17 16:17	30	2021-12-05 07:13
9	2021-05-07 18:52	31	2021-12-05 19:25
10	2021-05-09 13:53	32	2021-12-06 05:34
11	2021-05-22 01:24	33	2022-01-01 13:43
12	2021-05-22 02:52	34	2022-01-08 01:28
13	2021-05-22 06:48	35	2022-01-13 12:59
14	2021-05-22 15:53	36	2022-01-13 14:02
15	2021-05-22 21:31	37	2022-01-18 17:31
16	2021-05-23 04:34	38	2022-01-20 05:55
17	2021-05-23 09:19	39	2022-01-29 23:09
18	2021-05-23 11:03	40	2022-02-08 21:38
19	2021-07-24 00:25	41	2022-03-05 23:52
20	2021-08-26 18:07	42	2022-03-10 20:50
21	2021-08-26 23:18	43	2022-03-14 17:14
22	2021-08-28 05:01		

3.3 Determining and Fitting a Peak Intensity Spectrum

To study the shape of SEE spectra measured by SolO we first need to determine the peak intensity at each energy channel of the three electron-measuring EPD instruments (i.e., STEP, EPT and HET) and then fit the spectrum with a suitable function.

Figure 9 shows an example of an SEE spectrum measured by SolO. The lower and fainter points correspond to the pre-event background and the the higher points correspond to the background-subtracted peak intensity measured by STEP, EPT and HET. The gray points represent data that are excluded from the spectrum and the later fit. Points are excluded either because the peak intensity does not rise above the background by at least three standard deviations (3σ), the relative error in determining the intensity is high (over 50%) or if there are too many data gaps in the temporal coverage of a certain channel so that these gaps cover more than 10 % of the observation time in the channel.

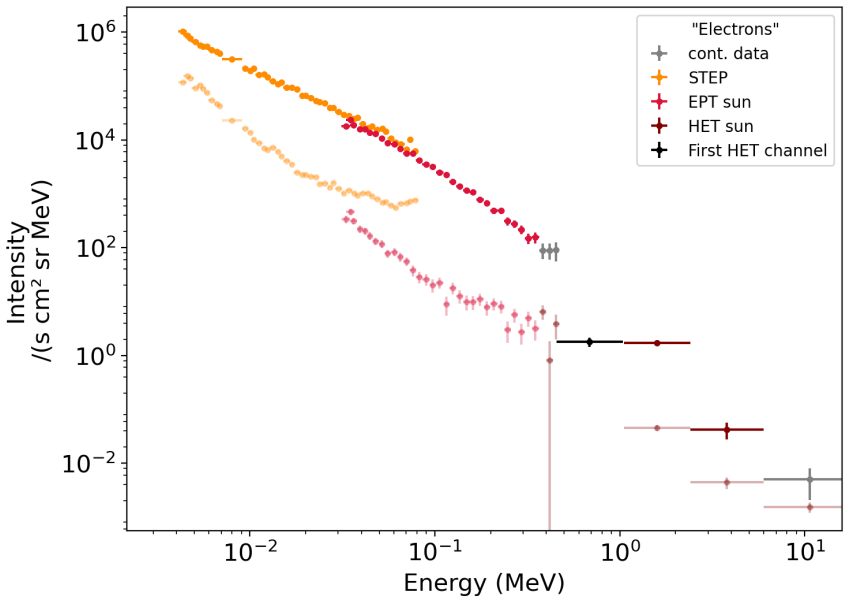

Figure 9. Example of an SEE spectrum measured by SolO on 07 May 2021. The lower and fainter points represent the background, while the higher points represent the intensity measured by STEP, EPT and HET. The gray points represent discarded data.

To make sure we are analysing the right peak we produce time series plots to visualize the event. When determining the peak we need to take into account effects such as velocity dispersion. We also subtract the background from each energy channel and correct for ion contamination for EPT by using the simulated response functions of the telescope. These responses tell us how much each ion channel contributes to each of the electron channels. We then calculate this contribution for each time step and subtract the ion contributions from all the electron channel. The method was provided to us by the instrument team (F. Espinosa, private communication). We repeat this process for one-, two- and five-minute averaged data and choose the best time averaging after each fit (see Section 4.4). The process of determining the peak intensities and making the fit is explained in detail in the following subsections.

3.3.1 Finding the Intensity Peak

For each event listed in table II we choose to analyze peak spectra and, therefore, we determine the peak intensity (Krucker et al., 2009; Dresing et al., 2020) at each energy channel of STEP, EPT and HET. To make sure that we are analysing the right peak, as there might be multiple peaks in the data and following the event, we produce separate time series plots for the three EPD sensors to visualize the event. The STIX/EPD common event list also provides us with an approximate flare time observed by STIX. We assume that the observed flare corresponds to the parent acceleration region of the SEE event observed by EPD. The flare time helps us narrow down the time at which the event is measured by SolO. Knowing the spacecraft distance from the Sun and assuming the solar wind speed to be for example 400 km/s we can calculate an approximate travel time of the particles from the Sun to the spacecraft along the Parker spiral (Dresing et al., 2020). We define a small time window around the time SolO sees the event and take the maximum

intensity within this window. Figure 10 shows an example of a time series of the electron intensity measured by EPT. The gray area marks the background window that is used to determine the mean background value. This is then subtracted from the peak intensities. The black vertical lines define the beginning and end of the search window. The green vertical line defines the maximum (peak) intensity within that window. If the peak intensity does not rise significantly above the background (3σ) the peak is marked with a blue dashed line. If the relative error of the intensity after the background subtraction is high (over 50%) the peak is marked with an orange line and, finally, if the data gaps within the search window cover more than 10 % of it, the peak is marked with a gray line.

The search window in Figure 10 is defined as fixed non-shifting search window, meaning that the search start and end time marked by the vertical black lines and the time interval in between the black lines, are the same for all energy channels. This fixed non-shifting search window is not ideal in all cases. Often, especially in the STEP energy range, we need to take into account velocity dispersion, which causes electrons at lower energies to arrive to the spacecraft much later than their high-energy counterparts and are, therefore, detected with a certain delay. Figure 11 is an example of such case for STEP. In the figure we can clearly see that by using a fixed non-shifting search window the peak wanders out of the search window. In the upper part of the figure (lower energies) the search window covers the peak, while at higher energies (the lower part of the image) the peak remains on the left of the search window, since the higher energy electrons arrive to the spacecraft sooner. In this special case, we can also see a second peak, which corresponds to another event. The second peak is detected at the higher energies instead of the real peak.

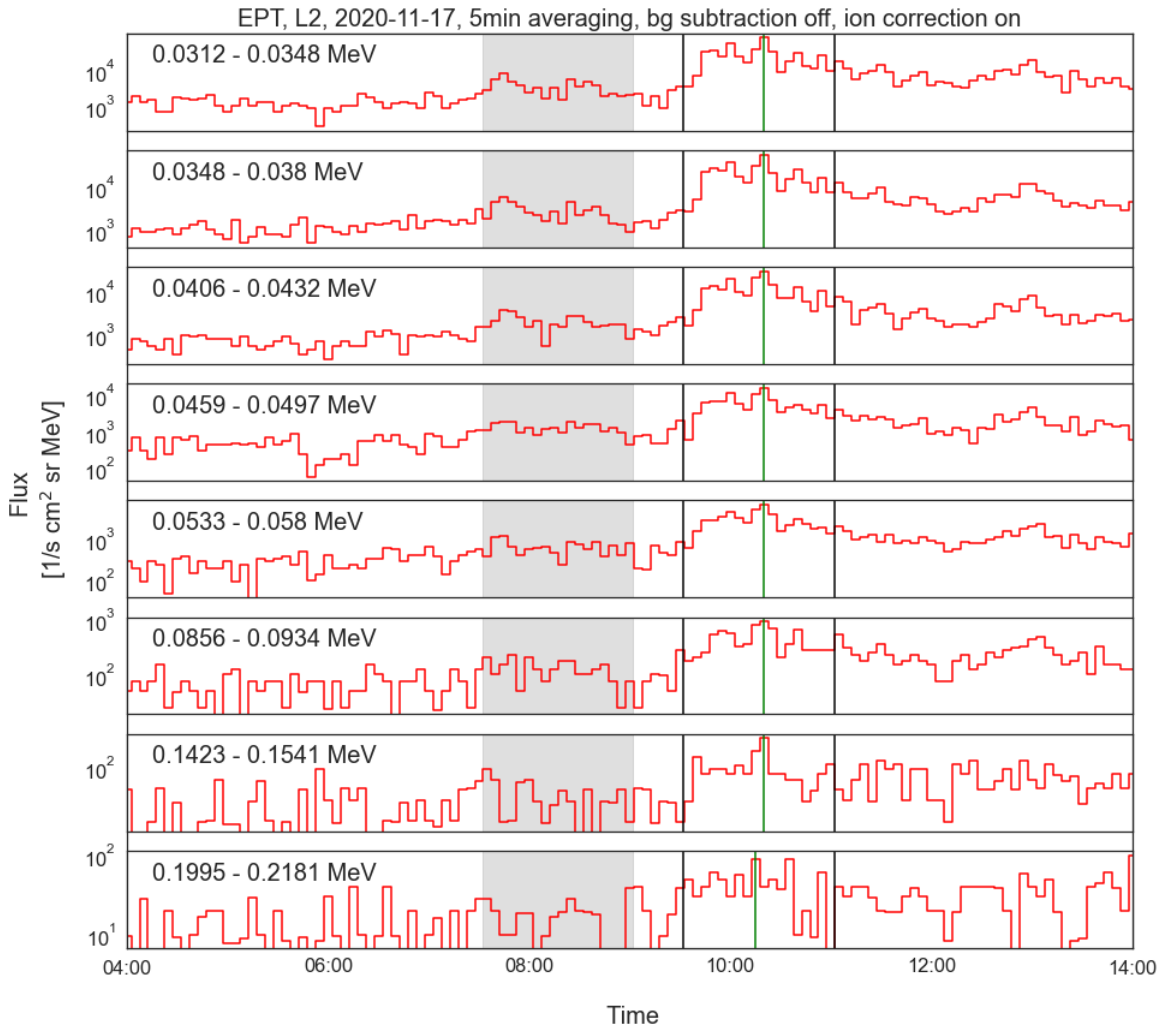

Figure 10. Example of a time series of the electron intensity measured by EPT. The figure only shows part of the available energy channels. In the figure the black vertical lines define the beginning and end of the search window used to find the intensity peak. The green line marks the maximum (peak) intensity within that window. The gray area marks the background window that is used to determine the mean background value. This is then subtracted from the peak intensities.

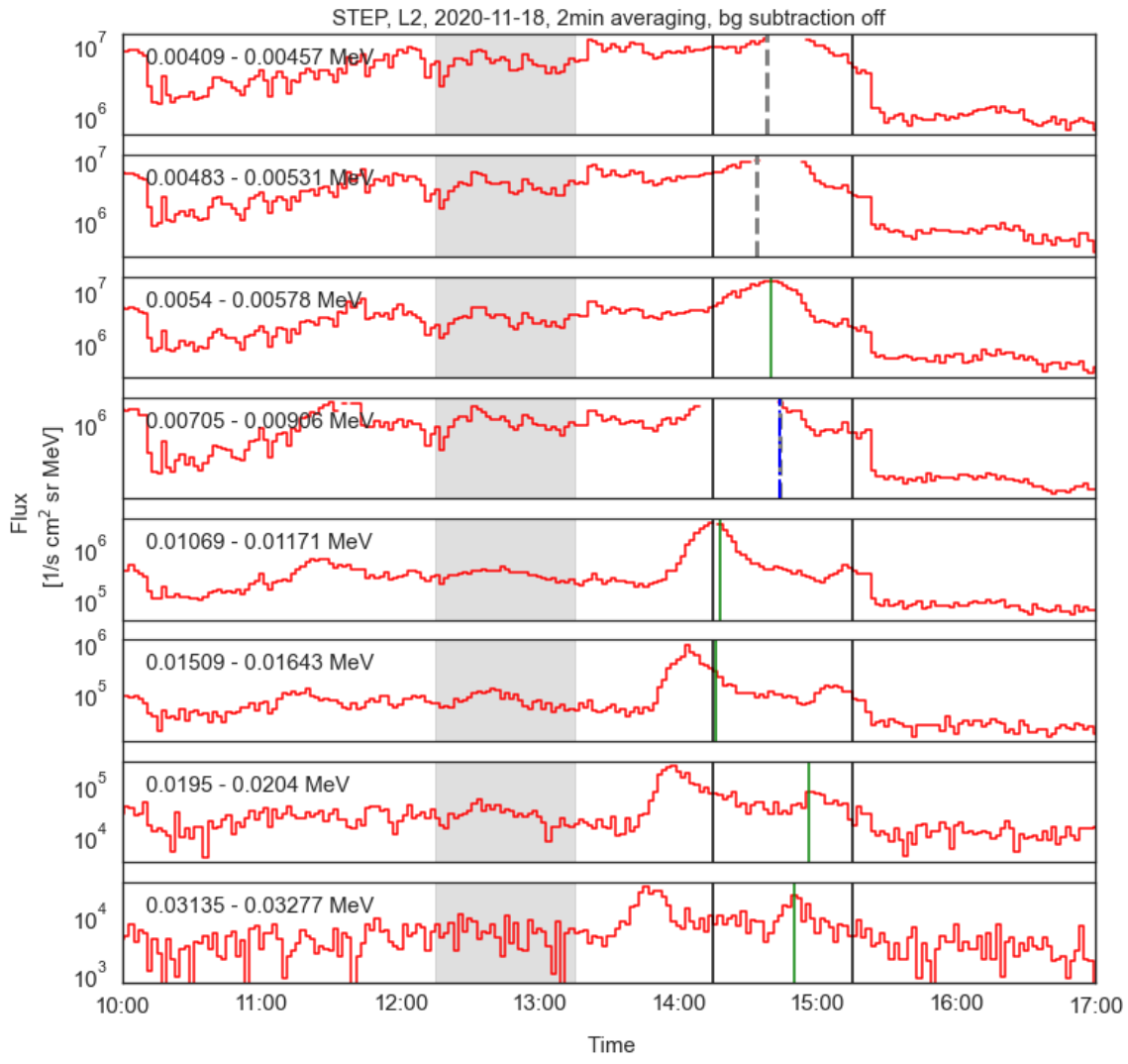

Figure 11. Example of a fixed non-shifting search window for an event with clear velocity dispersion in the STEP energy range. The figure only shows part of the available energy channels. In the picture we can also notice a second event close by. The real peak is detected at lower energies (upper part of the image), but the peak remains on the left of the search window in the lower part of the image. In cases such as this one, a fixed non-shifting window is not ideal because the electrons at lower energies arrive to the spacecraft much later than their high energy counterparts. The peaks are marked by differently colored lines if they don't fulfill all our quality requirements and the energy channels corresponding to the peak are then automatically excluded from the spectrum.

To avoid this problem the search window should move according to the velocity dispersion. Firstly, we need to determine an approximate value for the Parker spiral length. The charged particles travel along the spiral to arrive to the spacecraft so the spiral length provides a lower limit to the travel distance. The Parker spiral length L is calculated as follows (Parker, 1958):

$$L = \frac{1}{2}\frac{v_{sw}}{\Omega} \cdot \left[\frac{\Omega}{v_{sw}}(r - r_S)\sqrt{(r - r_S)^2 \left(\frac{v_{sw}}{\Omega}\right)^2 + 1} + \ln\left(\frac{\Omega}{v_{sw}}(r - r_S) + \sqrt{\left(\frac{\Omega}{v_{sw}}\right)^2 (r - r_S)^2 + 1} \right) \right] \tag{1}$$

where Ω is the solar rotation frequency, v_{sw} is the solar wind speed (we assume it to be 400 km/s), r is the distance from the Sun's surface and r_S is the radius of the Sun.

Next, we determine the correction coefficient β for electrons with a certain energy and then calculate their speeds:

$$\beta = \sqrt{1 - \left(\frac{m_{e,0}c^2}{E_k + m_{e,0}c^2}\right)^2} \tag{2}$$

$$v = \beta \cdot c \tag{3}$$

here E_k is the kinetic energy of the electrons, $m_{e,0}$ is the rest mass of an electron, c is the speed of light and v is the speed of an electron with kinetic energy E_k. Knowing the travel distance L and the particle velocities, along with the injection time at the Sun, we can calculate an approximate time of arrival of the electrons to the spacecraft for each energy channel:

$$T = T_{inj} + \frac{L}{v} \tag{4}$$

where T_{inj} is the injection time at the Sun, L is the travel distance (equal to the Parker spiral length) and v is the velocity of an electron with kinetic energy E_k. These calculations are done for each energy channel of STEP, EPT and HET using the geometric mean energy to find the best possible search window for each energy

bin and correct for the spectral shape within each energy channel. Figure 12 shows an example of a fixed moving window for the same event as in Figure 11. The window is fixed in terms of length but is moving, meaning it has a different start and end time for each energy channel according to velocity dispersion. The start and end time of the search window are denoted by black vertical lines. The green vertical line denotes the peak intensity and the blue line marks the excluded peak as explained for figure 10. The gray area is the part of the background that will be subtracted from the peak intensity and follows the velocity dispersion as well.

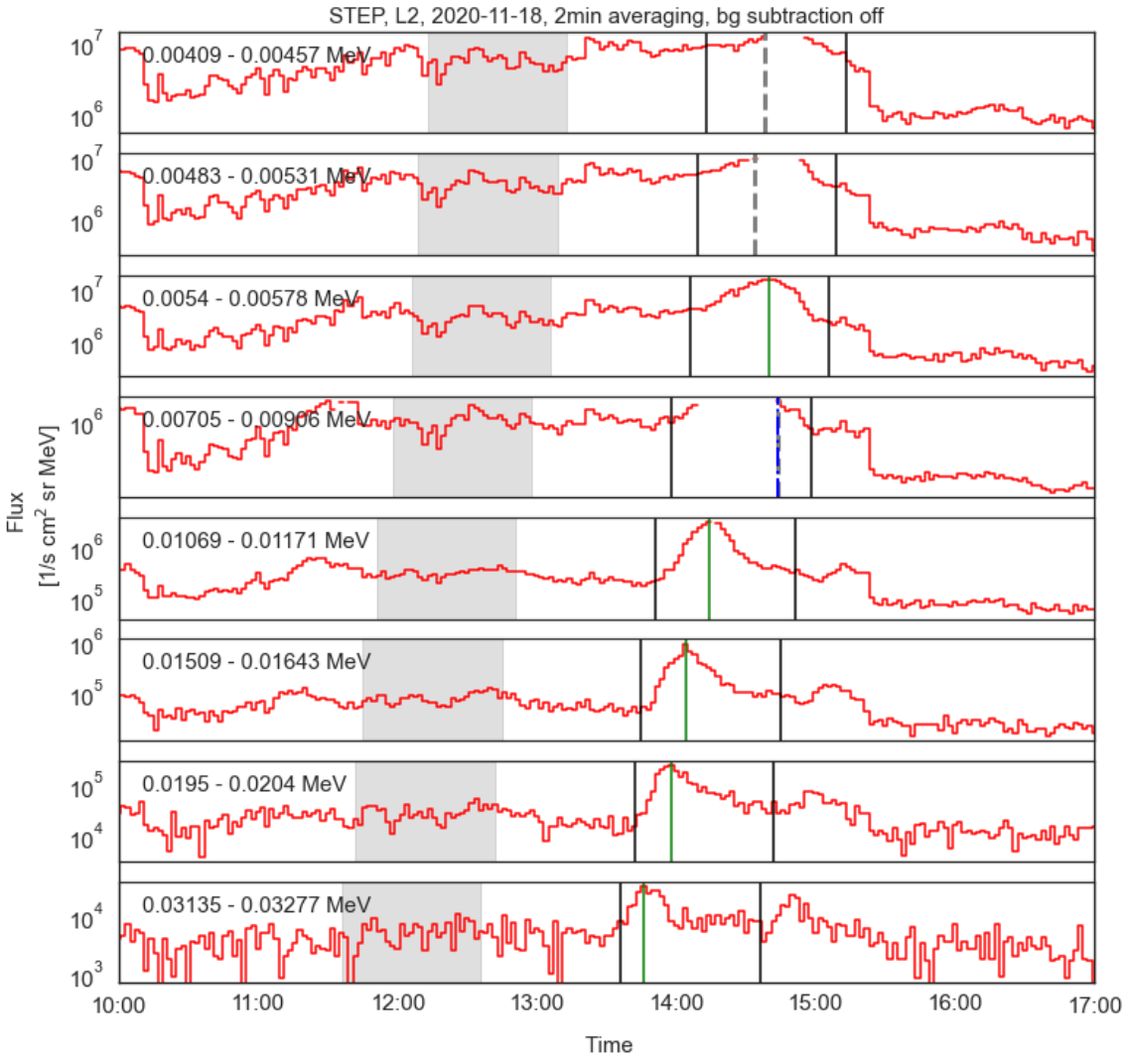

Figure 12. Example of a time series with fixed moving window. The black vertical lines define the beginning and end of the search window (for details see Figure 11).

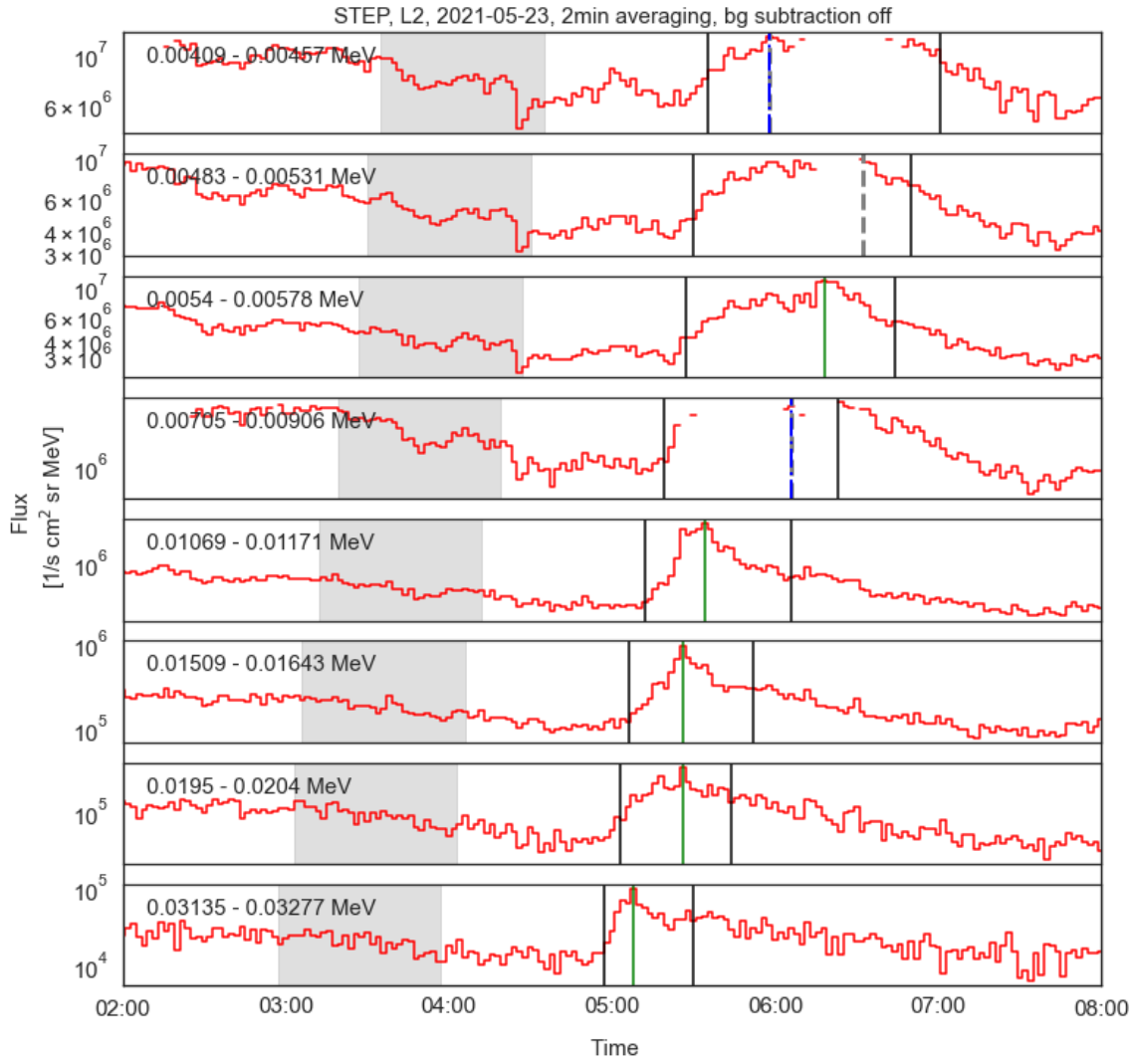

Figure 13. Example of a moving search window to identify the intensity peak with varying length (for details see Figure 11).

Velocity dispersion combined with particle scattering can cause the intensity peaks to spread out at lower energies. To tackle this problem, we can define a second slope to make the search window wider at lower energies. This option creates a moving search window which also changes length depending on the energy channel. Figure 13 shows an example of such moving search window. As seen from the figure, the intensity peak spreads out significantly at lower energies and gets much narrower at higher energies. The non-fixed window guarantees that we find the actual intensity peak at all energy channels without cutting it off or including a

potential different and unrelated peak.

3.3.2 Fitting the Energy Spectra

One of the key parts of this thesis and in general in analyzing SEP, or more specifically SEE, spectra is the fitting process. We wrote a Python-based program that enables us to fit four different functions to the spectra and choose the most suitable model to describe its shape. As previously mentioned, we defined the peak intensity spectra using one-, two- and five-minute averaging. The reason for this is to check whether or not a bigger averaging introduces a bias to the fit results. This will be explained in more detail in section 4.4.

We use the `scipy.odr` package of Python to fit the data including uncertainties for both energy and intensities. The energy bin width serves as uncertainty for the energy and each intensity value has an uncertainty based on counting statistics. We also fit both together and separately each instrument (i.e. STEP, EPT and HET) because we want to study the possible effects this may have on a spectral break. This will be explained in section 4.2.

The possible fitting functions The software contains four different functions that can be fit to the peak spectrum:

$$I(E) = I_0 \left(\frac{E}{E_0}\right)^{\gamma_1} \tag{5}$$

$$I(E) = I_0 \left(\frac{E}{E_0}\right)^{\gamma_1} \left(\frac{E^\alpha + E_b^\alpha}{E_0^\alpha + E_b^\alpha}\right)^{\frac{\gamma_2-\gamma_1}{\alpha}} \tag{6}$$

$$I(E) = I_0 \left(\frac{E}{E_0}\right)^{\gamma_1} \cdot e^{-\left(\frac{E}{E_c}\right)^2} \tag{7}$$

$$I(E) = I_0 \left(\frac{E}{E_0}\right)^{\gamma_1} \left(\frac{E^\alpha + E_b^\alpha}{E_0^\alpha + E_b^\alpha}\right)^{\frac{\gamma_2-\gamma_1}{\alpha}} \cdot e^{-\left(\frac{E}{E_c}\right)^2} \tag{8}$$

equation (5) corresponds to a single power-law with power-law index γ_1 (see Figure 14), equation (6) is a broken power law transitioning between power-law indices γ_1 and γ_2 about the break energy E_b (see Figure 15), equation (7) is a single power law function with power-law index γ_1 and an exponential cutoff point at an energy of E_c (see Figure 16) and equation (8) is a broken power law transitioning between power-law indices γ_1 and γ_2 about E_b with an exponential cutoff point at an energy of E_c (see Figure 17). I_0 is a differential flux defined at the reference energy of E_0 =0.1 MeV and α describes the sharpness of the transition between power-law indices (the higher the value of α the sharper the transition).

These equations are a revisitation of the equations introduced by Ellison et al. (1985). Equations (6) and (7) are the same equations used by Strauss et al. (2020). In contrast to the single power-law function with a cutoff used by Ellison et al. (1985) we square the energy in the exponent to make the cutoff more pronounced. Equation (8) also has a squared energy in the exponent and is the only function that might be able to detect two breaks in the spectrum among the four models that we are using.

As previously mentioned, we also produce fits to each instrument separately and also to combinations of them (e.g. STEP+EPT, STEP+EPT+HET and EPT+HET). Figure 14 and 16 are examples of fits to only STEP data with two different functions, single power-law and single power-law plus cutoff respectively. Figure 15 is an example of a combined fit to STEP and EPT data and Figure 17 is an example of a combined fit to STEP, EPT and HET data. The dashed purple line in Figures 16 and 17 marks the cutoff energy and the dashed blue line in Figures 15 and 17 marks the spectral break energy.

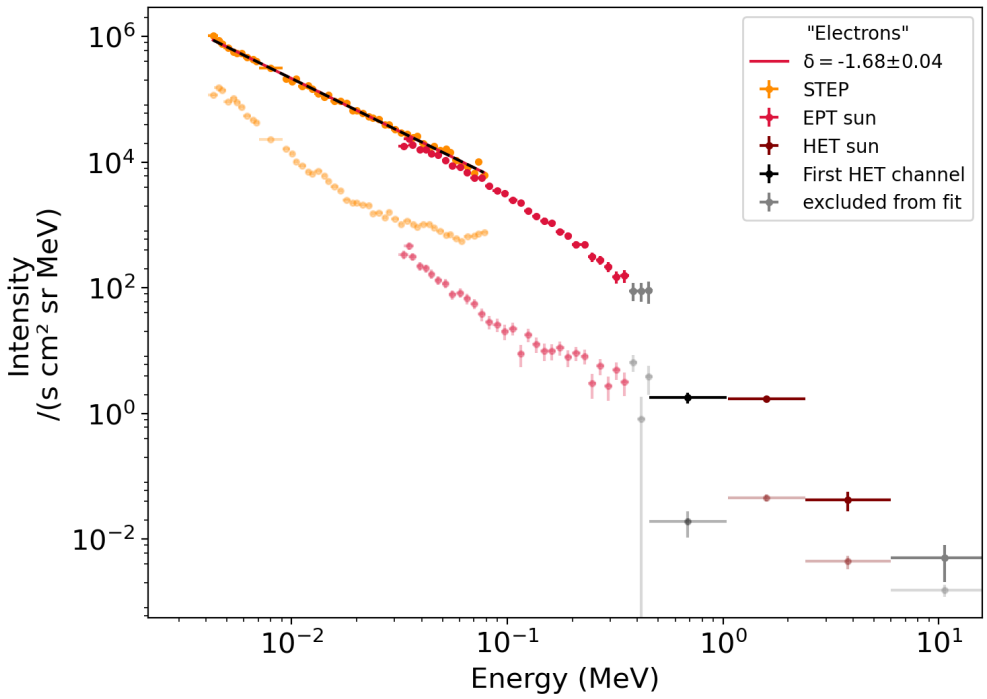

Figure 14. Example of a single power-law fit to STEP data corresponding to an event on 07 May 2021. For more details see Figure 9.

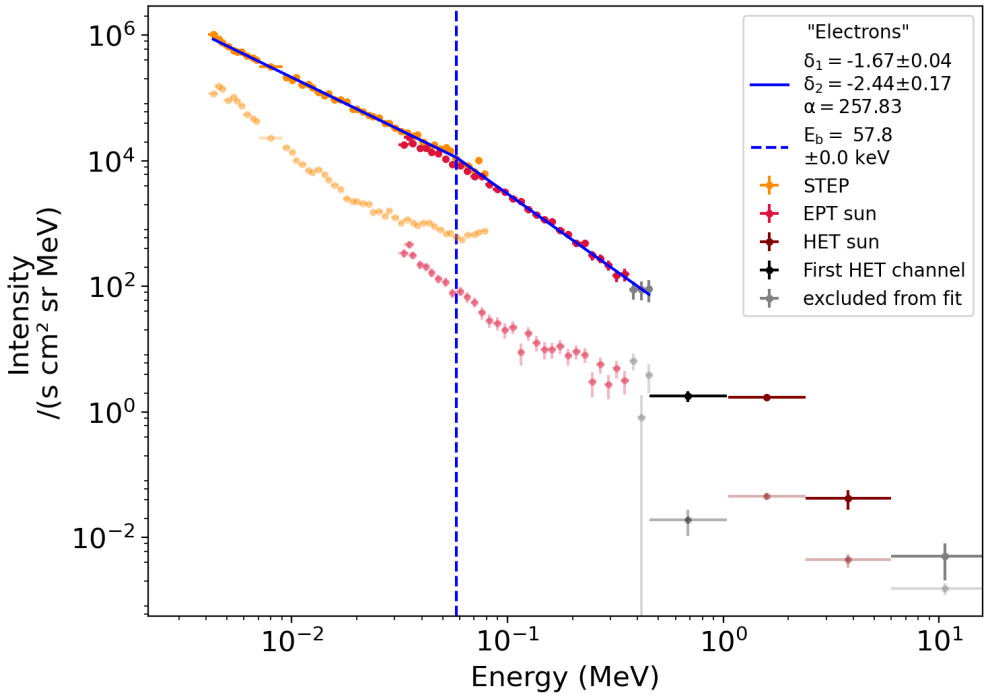

Figure 15. Example of a broken power-law fit to STEP+EPT data corresponding to an event on 07 May 2021. The dashed blue line marks the spectral break energy. For more details see Figure 9.

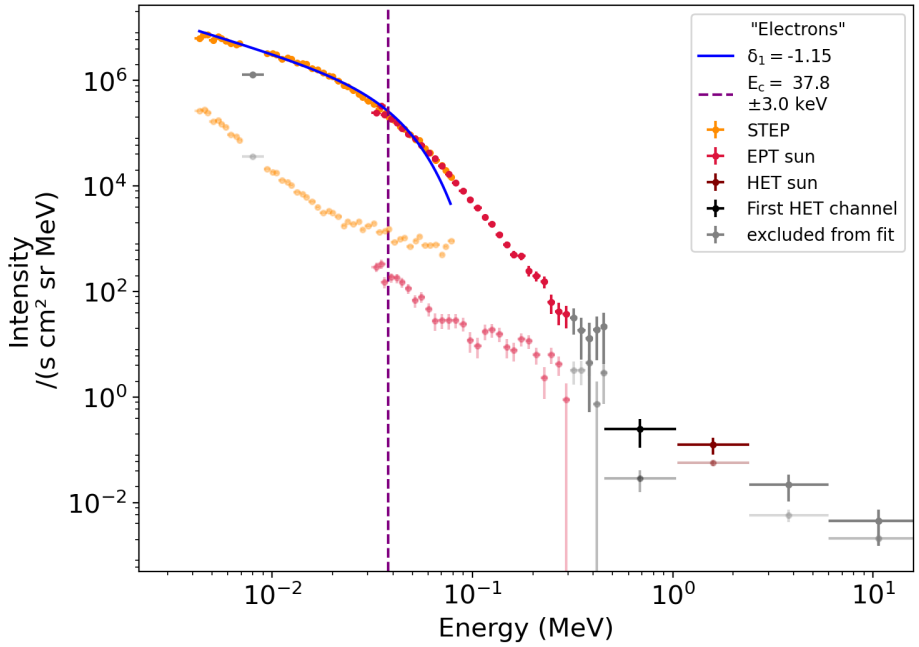

Figure 16. Example of a single power-law+cutoff fit to STEP data corresponding to an event on 26 August 2021. The dashed purple line marks the cutoff energy. For more details see Figure 9.

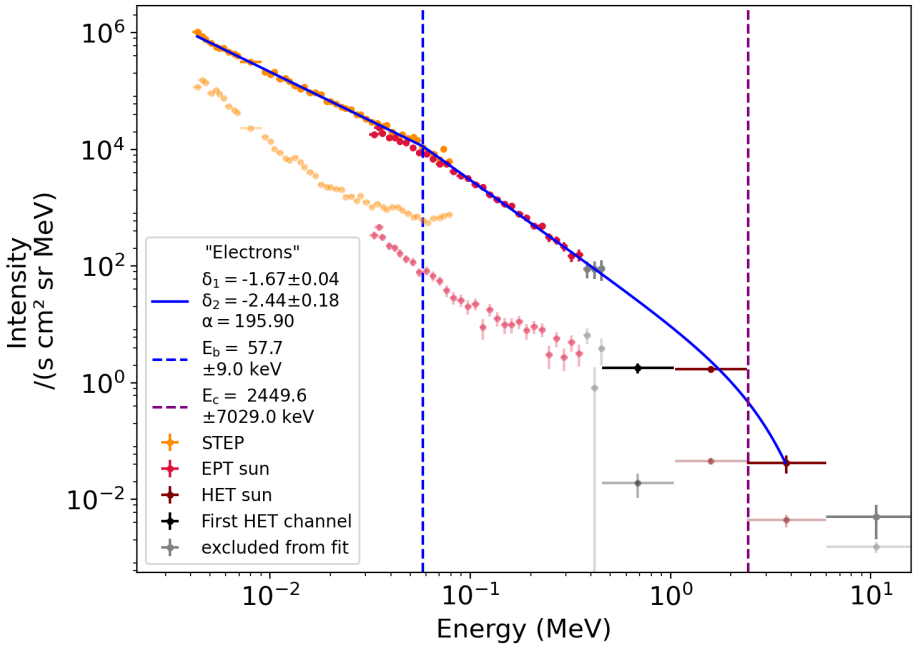

Figure 17. Example of a broken power-law+cutoff to STEP+EPT+HET data corresponding to an event on 07 May 2021. The dashed purple line marks the cutoff energy and the dashed blue line marks the spectral break energy. For more details see Figure 9.

Guess values, random values and the choice of the best fit In order to make a fit we first need to provide, what we would call, guess values for each variable in the possible fitting functions (eqs. (5)-(8)). The choice of the values for each parameter should not be random. We chose the guess values based on findings from previous studies (Krucker et al., 2007; Krucker et al., 2009; Kontar and Reid, 2009; Dresing et al., 2020; Strauss et al., 2020).

The spectral index γ_2 should always be smaller than γ_1. Kontar and Reid (2009) found γ_1 to be between -2 and -2.5 in their simulations and γ_2 to be between -3 and -5. This is close to what Krucker et al. (2009) found in their study, where the mean value for γ_1 was -1.9 and γ_2 was -3.6. The value found by Dresing et al. (2020) for γ_1 was slightly different with a mean of -2.94, while the mean value for γ_2 was -3.55, almost the same as what Krucker et al. (2009) found. Kontar and Reid (2009) found the spectral break energies to be between 4 keV and 80 keV. The break energy found by Krucker et al. (2009) was within that range, 60 keV, while Dresing et al. (2020) found it to be 120 keV. Strauss et al. (2020) found various values for α from as small as 3 in the smoothest transitions to as high as 46 in the sharper ones. By definition the cutoff energy should be higher than the break energy. I_0 is the intensity at a fixed energy E_0 close to the break energy. We fix this energy to be 0.1 MeV.

Each fit is done using the following fixed set of guess values:

1. γ_1 = -1.9
2. γ_2 = -2.5
3. α = 7.16
4. E_b = 0.06 MeV or 0.1 MeV
5. E_c = 0.12 MeV

6. $I_0 = 1000$ /(s cm^2 sr MeV)

As a next step we use the software to choose the best mathematical model between equations (5)-(8) to fit the data. The software fits, for each event, the four equations and chooses the best fit based on the reduced χ^2 ($=\chi^2/DOF$, Degrees Of Freedom). The output of the ODR function includes the residual variance, which corresponds to χ^2/DOF.

Instead of just using the fit resulting from the guess values, we programmed the software to iterate through a randomly selected combination of values for each parameter listed above. Each parameter (γ_1, γ_2, α, E_b, E_c and I_0) has a pre-defined list of values based on results from previous studies (Krucker et al., 2009; Kontar and Reid, 2009; Dresing et al., 2020; Strauss et al., 2020) from which these random values will be chosen. The random values are not chosen from one extreme of a list to the other. We take into account the guess value and choose the random part within 20 % of the list's length from the guess value. Each one of the mathematical models is fit again to the data using the randomly selected combination of values. The reduced χ^2 resulting from the fit is compared to the one from the previous fit. The result with the smaller reduced χ^2 value is be chosen as the so-far best result. This process can be repeated an *iteration*-amount of times. So, the program itself does a certain number of iterations per fit run. In our case we chose the number of iterations to be 20.

4 Data Analysis

4.1 Unexpected Hardening of the Spectra

During our analysis of the fitting results, we came across a few cases in which instead of having the usual spectral break, where γ_2 is smaller than γ_1, we found the opposite. This resulted in an unexpected upturn, where the spectrum hardens after the break. Usually, this could be a sign of ion contamination, but we correct for it when we determine the peak intensities (see section 3.3.1). Other explanations for this could be further instrumental issues or a combination of two acceleration mechanisms. Since our main focus is studying spectral breaks that could be related to findings in previous studies, we exclude these cases as they are related to a different scenario. Figure 18 shows an example of such upturn.

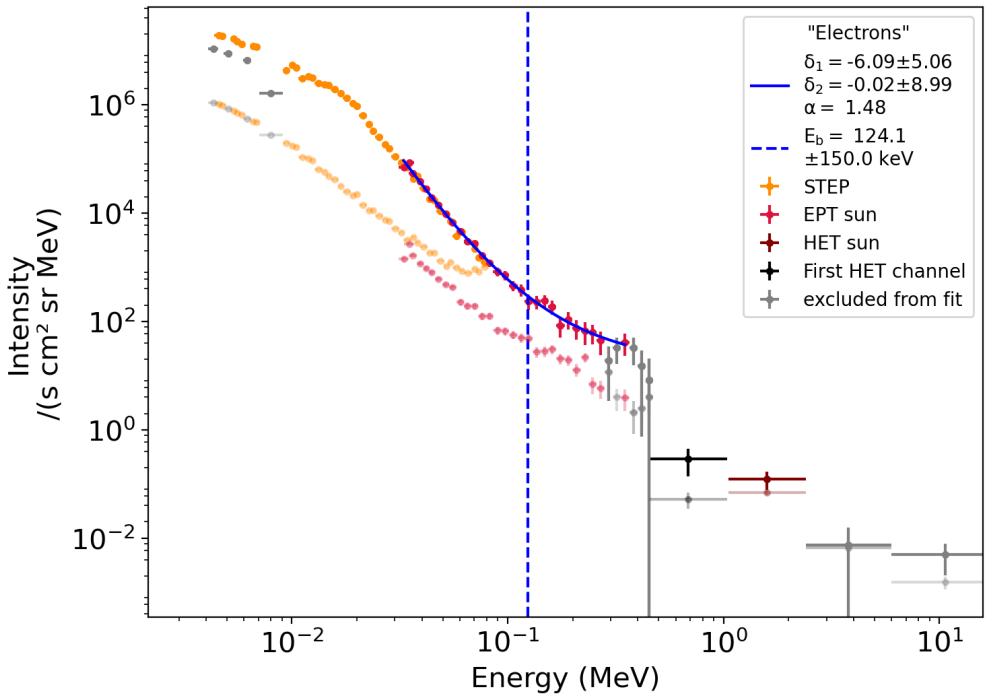

Figure 18. Example of fit with spectral hardening after the break corresponding to an event on 17 November 2020 (at $\sim$ 9:30). The fit is applied to EPT data. The gray points are excluded from the fit (see section 3.3 for more detail).

4.2 Searching for Different Spectral Breaks

In our analysis we investigate the presence of two separate spectral breaks. We study the effects that fitting instruments (STEP, EPT and HET) separately or together have on the spectral shape and the chosen mathematical model. There are cases in which the spectrum might have two separate breaks, one at lower energies in the STEP energy range and one at higher energies in the EPT (or HET) energy range. An example of such case is shown in Figures 19-21, which show the same measured spectrum with a fit to different energy ranges. By fitting only STEP data, the software finds the break to be at 23.1 ± 3.0 keV (Figure 19), if we fit only EPT data instead we find a break at 60.4 $\pm$13.0 keV (Figure 20). When we fit the data together, the software points towards the more prominent break, in this case the one at lower energies (Figure 21).

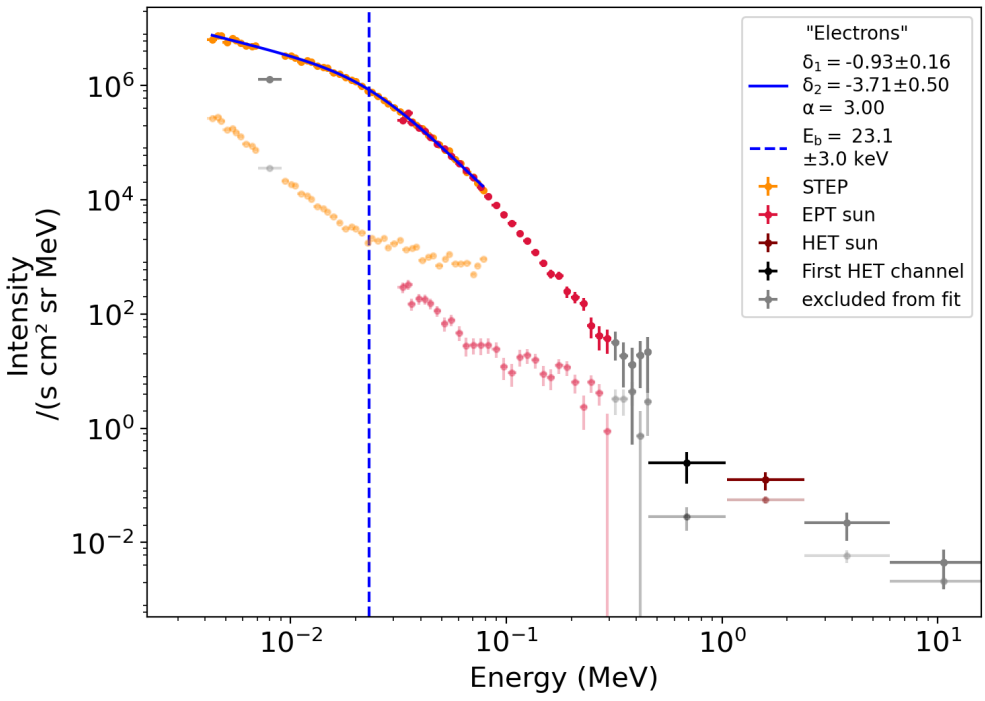

Figure 19. Example of fit to STEP data with a spectral break at 23.1 ± 3.0 keV . The gray points are excluded from the fit (see section 3.3 for more detail). The spectrum corresponds to an event on 26 August 2021.

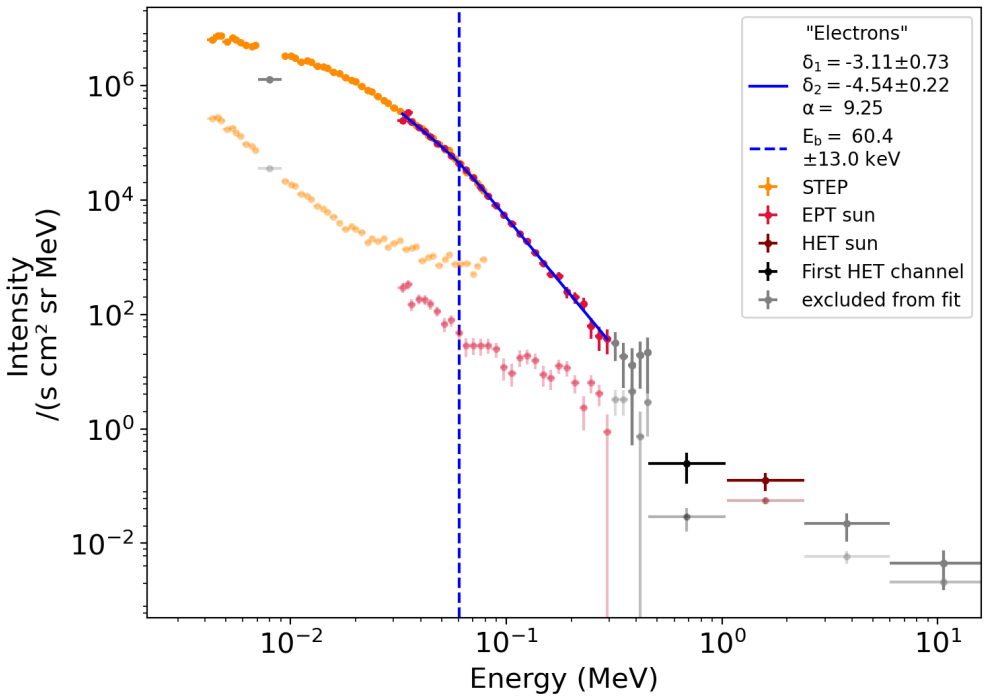

Figure 20. Example of fit to EPT data with a spectral break at 60.4 ±13.0 keV. The gray points are excluded from the fit (see section 3.3 for more detail). The spectrum corresponds to an event on 26 August 2021.

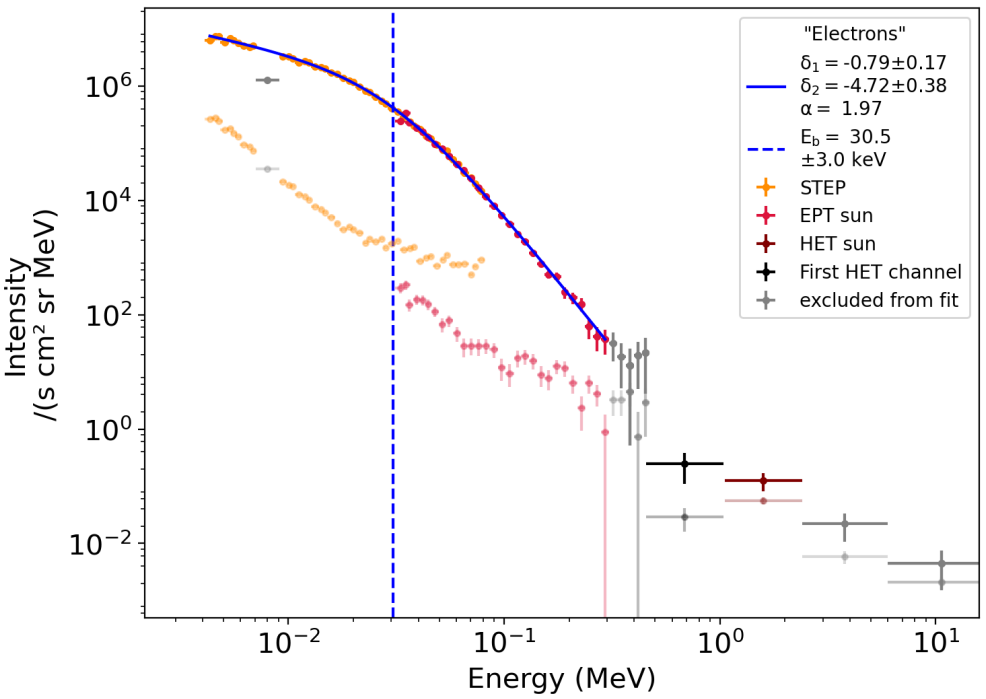

Figure 21. Example of fit to STEP and EPT data with a spectral break at 30.5 ±13.0 keV The gray points are excluded from the fit (see section 3.3 for more detail). The spectrum corresponds to an event on 26 August 2021.

The only mathematical model out of the four listed in section 3.3.2 that could possibly point toward a second break is the broken power-law with the exponential cutoff (eq. (8)). In this case, the software could not locate the second break with equation (8), since the high-energy behavior is well represented with a power-law. Thus, it still remains an open issue if the spectrum in this event hosts two breaks or not..

Figures 22-23 show another example of an event where we find two possible spectral breaks at 22.2 ±3.0 keV (Figure 22) in the STEP energy range and at 69.2 ±23.0 keV (Figure 23) in the EPT energy range. In this case, when we fit both instruments together, the software finds the best mathematical model to describe the shape of the spectrum to be a broken power-law with the exponential cutoff (Figure 24). We see that the break energy found when fitting STEP and EPT together is the same as if we fit only STEP data. The cutoff energy is 208.9 ±37.0 keV, far from the break found when fitting only EPT data.

Fitting multiple instruments together could potentially hide a second less prominent break, as it is clear that our fitting method tends to choose only the most prominent one. For this reason, it was important for our analysis to also fit the data for each instrument separately.

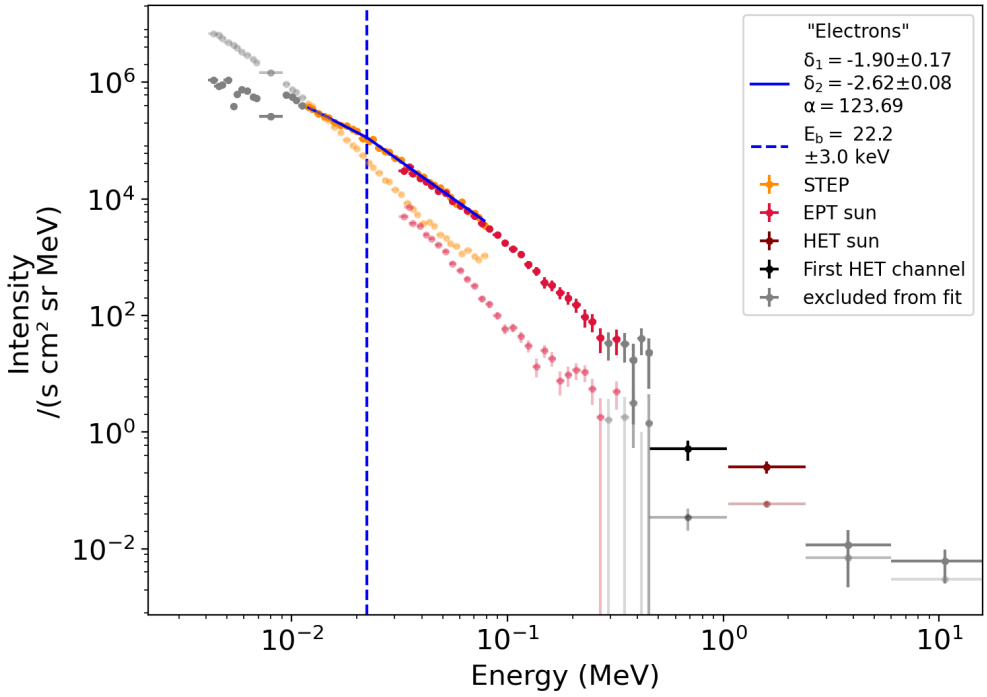

Figure 22. Example of fit with spectral hardening after the break. The fit is done to EPT data. The gray points are excluded from the fit (see section 3.3 for more detail). The spectrum corresponds to an event on 22 May 2021.

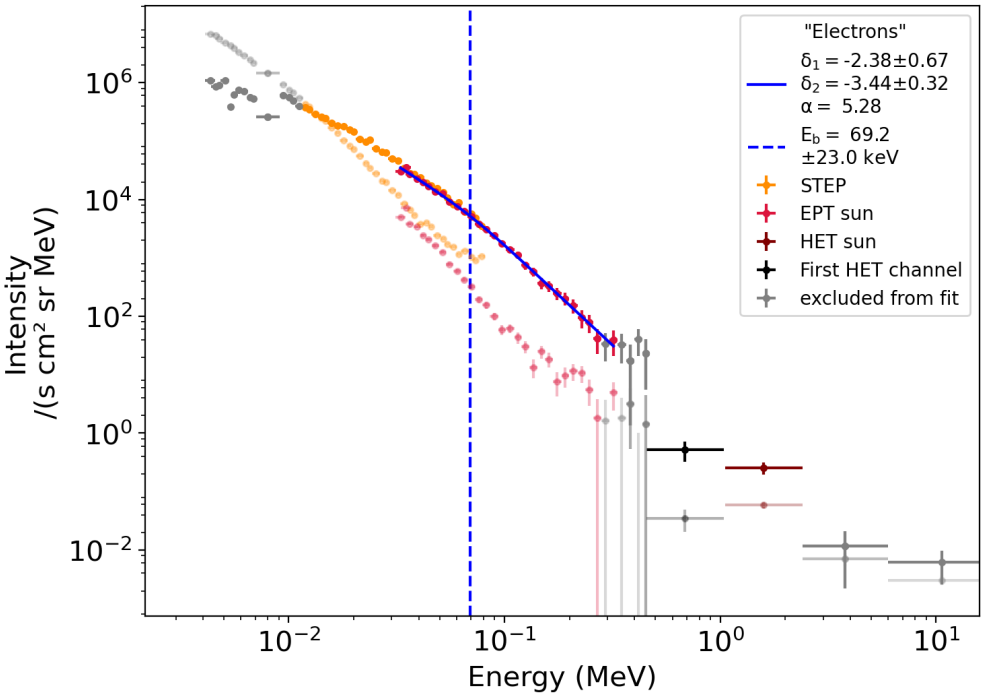

Figure 23. Example of fit with spectral hardening after the break. The fit is done to EPT data. The gray points are excluded from the fit (see section 3.3 for more detail). The spectrum corresponds to an event on 22 May 2021.

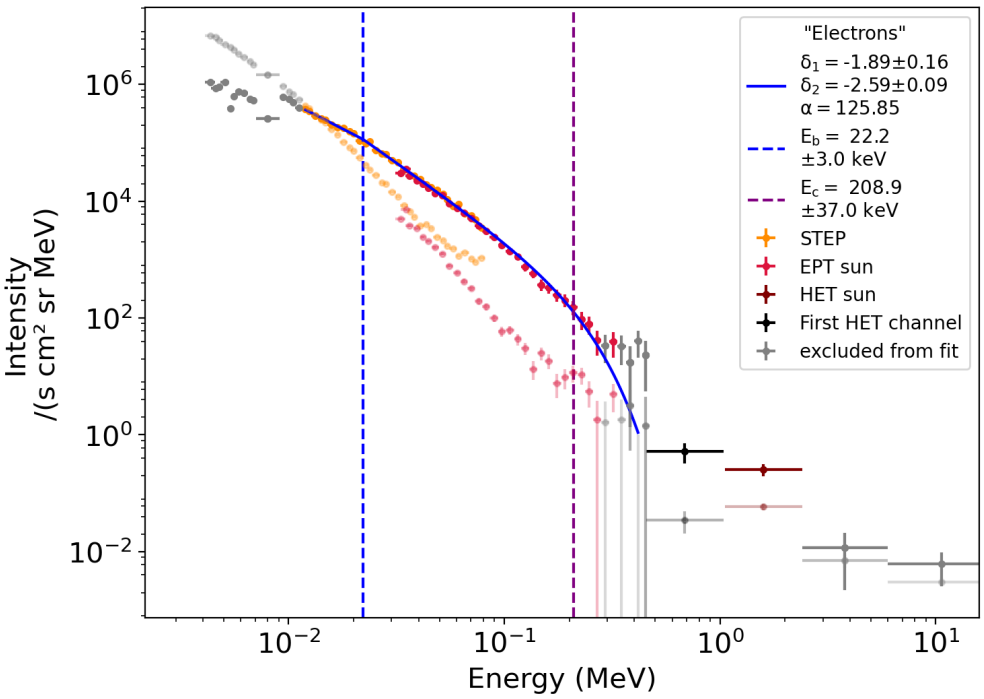

Figure 24. Example of fit with spectral hardening after the break. The fit is done to EPT data. The gray points are excluded from the fit (see section 3.3 for more detail). The spectrum corresponds to an event on 22 May 2021.

4.3 Intensity Offset Between STEP and EPT

Another important issue to take into account when fitting data from two separate instruments, is cross-calibration. From Figure 25 we can clearly see that the STEP and EPT energy channels that are overlapping are actually observing different intensities (marked by a blue square in the figure). This could influence the fit results. From Figure 27 and 26 we can see the difference between the break energies and the other parameters of a fit to the original data (Figure 26) and a fit to spectra where STEP intensity data has been shifted by a factor of 0.8 to align it to EPT data (Figure 27). In this case, as for almost all events, which have been analyzed in this thesis, with a clear shift, the differences are within the fitting uncertainties, but the actual uncertainty of the parameters could still be larger. Given that the shift does not affect the parameters significantly, we do not apply a shift to the data in the further analysis.

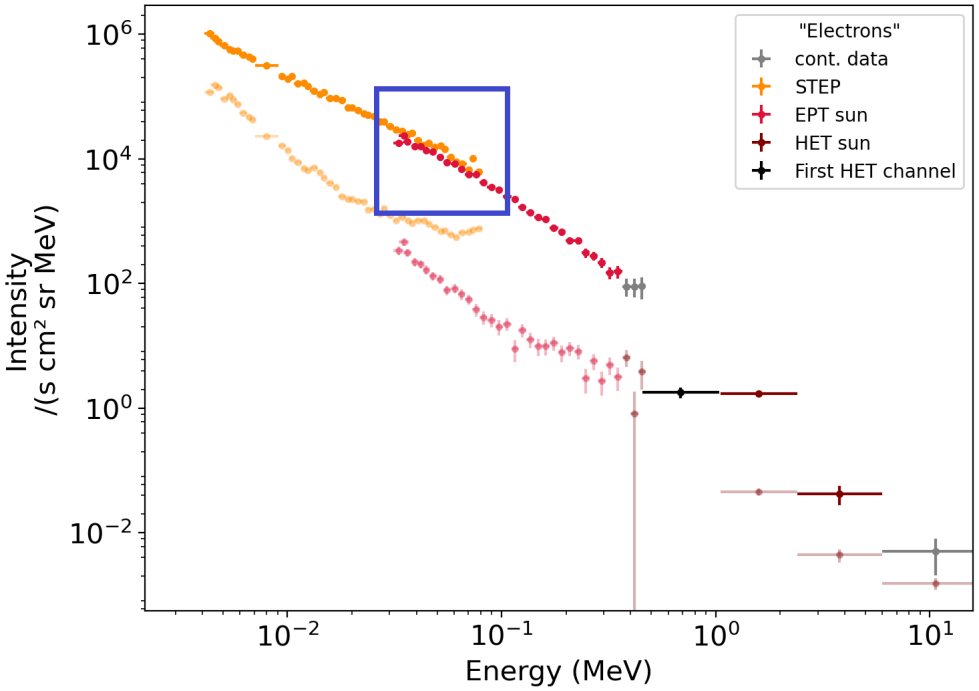

Figure 25. Example of a spectrum in which the STEP and EPT energy channels are not aligned (marked by the blue square). The spectrum corresponds to an event on 07 May 2021.

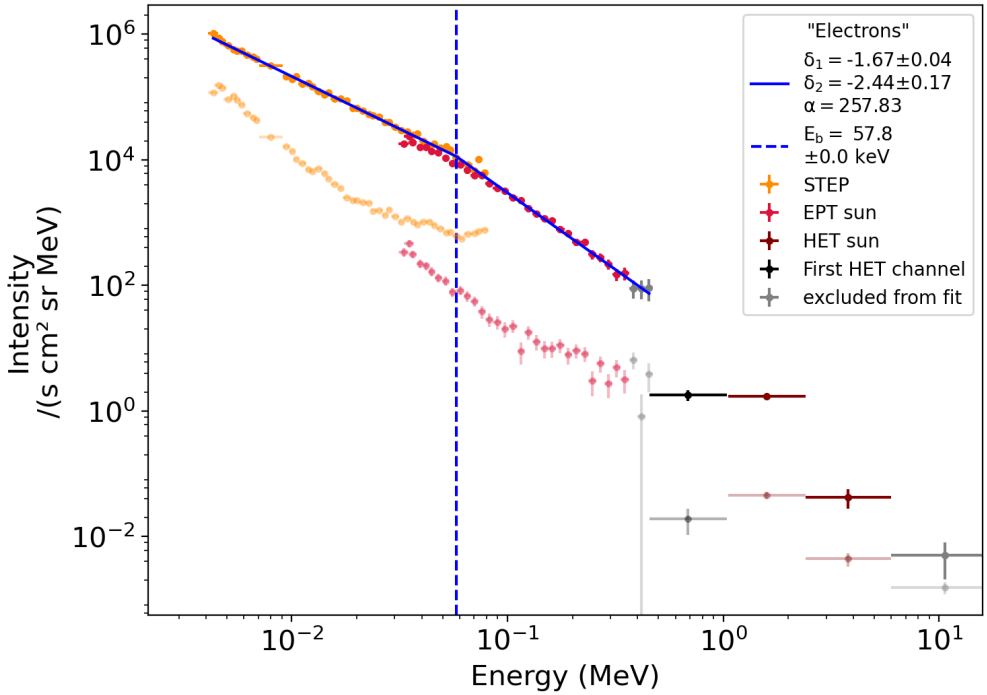

Figure 26. Example of a fit to a spectrum in which the STEP and EPT energy channels are not aligned.The spectrum corresponds to an event on 07 May 2021.

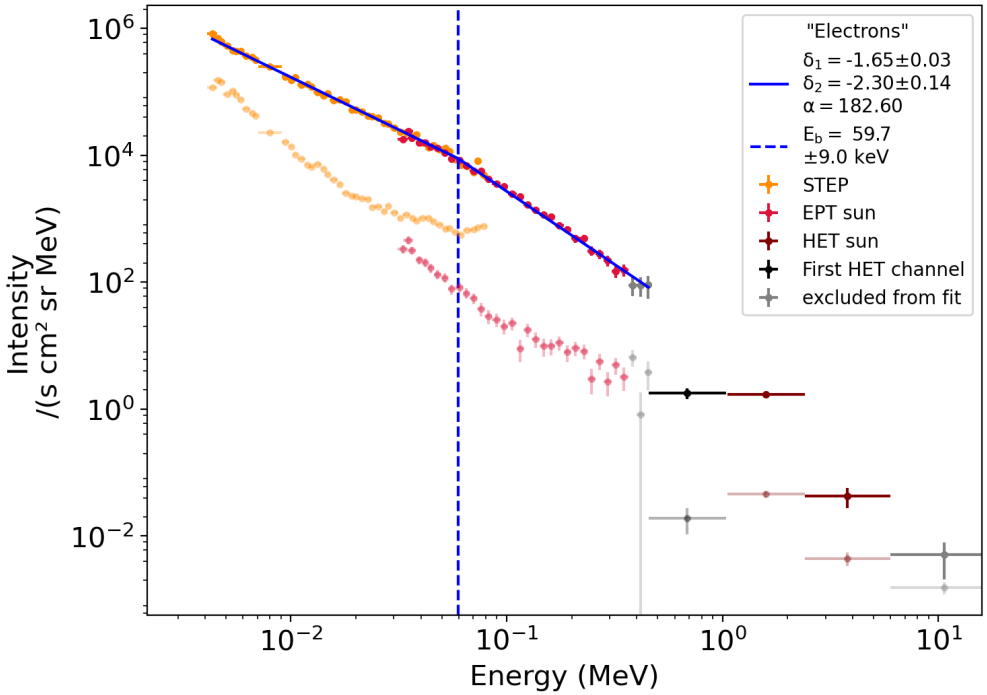

Figure 27. Example of a spectrum in which the STEP and EPT energy channels are aligned by appling a shift factor of 0.8 to EPT intensity data. The spectrum corresponds to an event on 07 May 2021.

4.4 Selection of the Best Time Averaging

The spectral fitting was done using three different time averagings of the intensity data: one minute, two minutes and five minutes. The main reason for this is that different events have different statistics and one time resolution may not work for all events. To make sure that a certain averaging does not introduce a systematic bias to the fitting results or hide the real peak of the event by averaging too much, we compared the values we get for the break energy E_b when fitting the spectra with differently averaged data. We repeated the same process also for the spectral index γ_1 and reduced χ^2 (see Appendix A), but focused on E_b as it is the most relevant parameter for our analysis.

We calculated the difference between the value we get for one averaging and another (e.g., the difference between E_b for one minute averaged data and E_b for two minutes averaged data). The smaller this difference is, of course, the better the

values agree with each other, meaning there is no significant difference between the two averagings. We also calculated the standard deviation of the differences to see how much the values vary from each other.

We plotted the values to visualize the differences, these are shown in Figure 28. Each row in the figure represents a fit to a different instrument or their combination (EPT, STEP, STEP+EPT and EPT+HET, respectively). The first column represents the values we get from one-minute averaged data (x axis) versus the ones we get for two-minute averaged data (y axis). The second column represents the values we get from on- minute averaged data (x axis) versus the ones we get for five-minute averaged data (y axis). And, lastly, the third column represents the values we get from two-minute averaged data (x axis) versus the ones we get for five-minute averaged data (y axis). Above each panel we write the number of events we have for each type of fit. The numbers vary because some events cannot be fit in the lower or higher energy range. The diagonal black line in each panel represents the zero or equality line, where the value for two different averagings would be the same. The diagonal blue line represents the mean value of the difference between the value for one averaging and another (e.g. the difference between E_b for one-minute averaged data and E_b for two-minute averaged data). The blue area represents the standard deviation of the differences of the values from the mean value.

A significant shift (i.e., outside the standard deviation range) of the blue line representing the mean of the difference, either upwards or downwards, would indicate the presence of a bias, while the closer the data points are to the black line, the better the values agree with each other. We also point out that the axis in the panels do not always have the same range.

We note from Figure 28 that there is no systematic difference between the averagings. Since there was no noticeable deviation or bias introduced by the different averagings, for each event we chose the fit to use in the analysis by comparing the

reduced χ^2. This means that the final data set is not based on a specific time averaging but rather contains the fit with the lowest reduced χ^2 value out of the three time averagings.

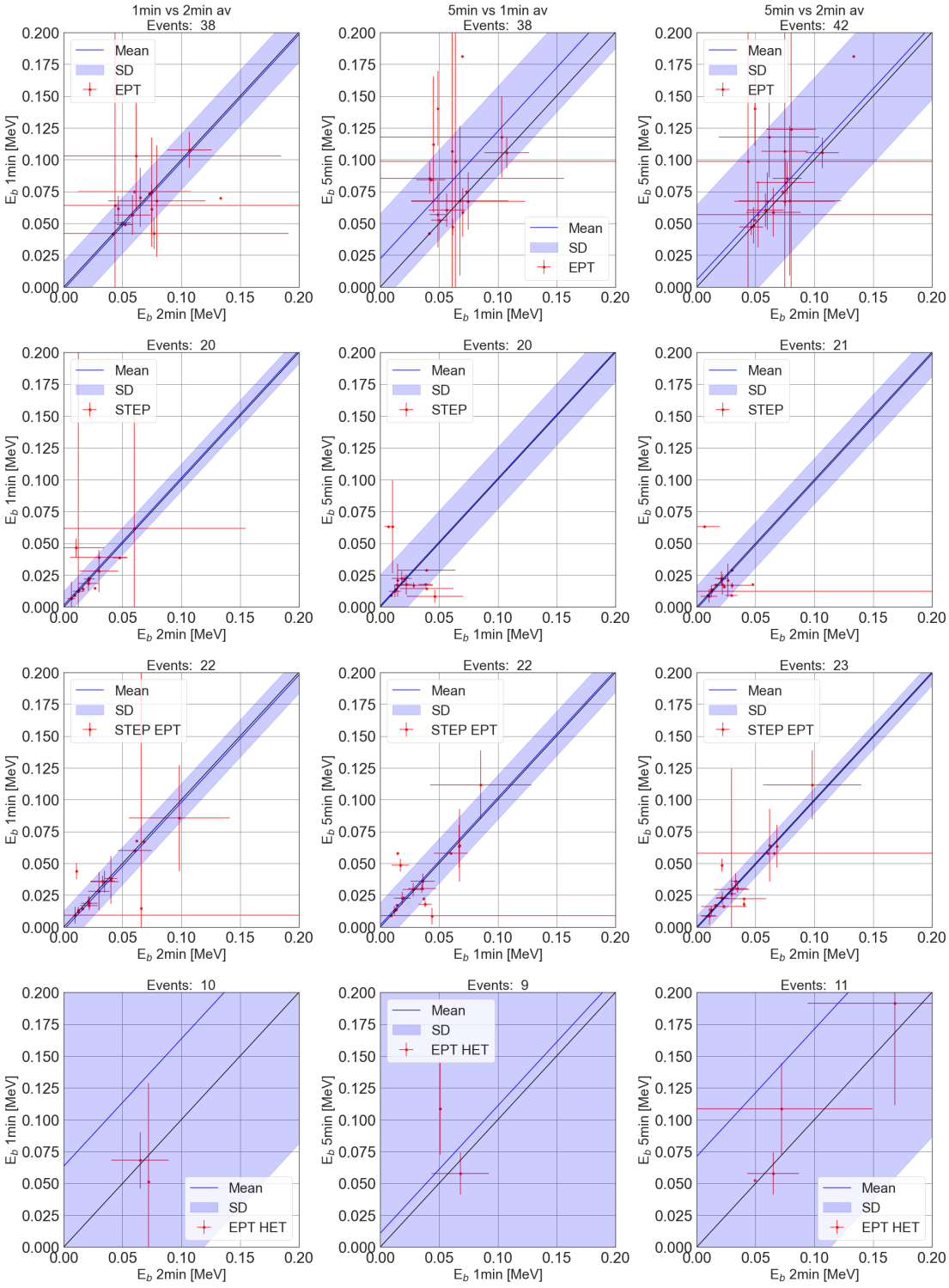

Figure 28. The Figure shows the comparison between the values of the break energy E_b for different averagings of the data: one, two and five minutes. Each column of panels shows the values of E_b found for the different averagings compared to each other. Each row represents the fit to a different combination of instruments: EPT, STEP, STEP+EPT and EPT+HET, respectively. The black line represents equality. So, the closer the data points are to the line, the more similar they are. The blue line represents the mean value of the difference of the E_b values. The blue area represents the standard deviation of the difference between the E_b values in each panel.

5 Results

In this section we summarize the results of our analysis. For all the 43 events in our list we fit STEP, EPT, STEP+EPT, STEP+EPT+HET and EPT+HET data. However, HET data before October 2021 cannot be used due to instrumental issues, which affect the relative intensity levels of the different energy channels. Also, we do not have STEP data for events after October 2021 since the data products have changed after this date. For these reasons, we decided not to use the STEP+EPT+HET fits in our analysis.

The main focus of our analysis is studying spectral breaks. By fitting different energy ranges we want to test if there are different break points in the spectrum and if so, study how the break energies are distributed in our sample of energy spectra and their possible connection to a specific transport effect by comparing them to previous results and predictions. Table III summarizes the mathematical model that best describes the spectrum measured by each instrument or combination of instruments. The gaps in the table indicate that the data was either not good enough to be fit or that there was no data available for that specific event. A fit is excluded from the analysis if it shows a spectral hardening after the break, which results in an upturn at high energies. Out of the fits to STEP data 15 have a broken power-law, two a single power-law, three a broken power-law with an exponential cutoff and one a single power-law with an exponential cutoff. The fits to STEP+EPT data produced 18 broken power-law fits and five broken power-law with an exponential cutoff fits, but no single power-law nor single power-law with an exponential cutoff. Six of the fits to EPT+HET data were broken power-laws, three were broken power-laws with an exponential cutoff and one was a single power-law with an exponential cutoff. Out of the fits to EPT data 25 have a broken power-law, 16 a single power-law, one a broken power-law with an exponential cutoff and one a single power-law with an exponential cutoff.

Table III. Event list with final type of fit.

Event yyyy-mm-dd-hhMM	STEP [2-80 keV]	STEP+EPT [2-475 keV]	EPT [25-475 keV]	EPT+HET [25 keV-30 MeV]
2020-11-17-0932	Broken pl	Broken pl	Broken pl	
2020-11-17-1826	Broken pl	Broken pl	Broken pl + exp cutoff	
2020-11-18-1314	Broken pl	Broken pl	Broken pl	
2020-11-18-1415	Single pl	Broken pl	Single pl	
2020-11-19-0548	Broken pl	Broken pl	Single pl	
2021-02-15-1311	Broken pl	Broken pl	Broken pl	
2021-03-05-1615	Broken pl	Broken pl + exp cutoff	Broken pl	
2021-04-17-1617	Broken pl	Broken pl	Broken pl	
2021-05-07-1852	Broken pl	Broken pl	Single pl	
2021-05-09-1852	Single pl	Broken pl	Broken pl	
2021-05-22-0124	Broken pl	Broken pl	Broken pl	
2021-05-22-0252	Broken pl	Broken pl	Broken pl	
2021-05-22-0648	Broken pl	Broken pl + exp cutoff	Broken pl	
2021-05-22-1553	Broken pl	Broken pl	Single pl	
2021-05-22-2131	Broken pl	Broken pl + exp cutoff	Broken pl	
2021-05-23-0434		Broken pl	Broken pl	
2021-05-23-0919	Broken pl	Broken pl	Exp cutoff	
2021-05-23-1103	Exp cutoff	Broken pl + exp cutoff	Broken pl	
2021-07-23-0025	Broken pl + exp cutoff	Broken pl + exp cutoff	Single pl	
2021-08-26-1807	Broken pl + exp cutoff	Broken pl	Broken pl	
2021-08-26-2318	Broken pl + exp cutoff	Broken pl	Broken pl	
2021-08-28-0501		Broken pl	Broken pl	
2021-09-28-0623	Broken pl	Broken pl	Single pl	
2021-10-09-0633			Broken pl	
2021-10-28-1526			Single pl	Broken pl
2021-11-01-0128			Broken pl	Broken pl
2021-11-09-1639			Single pl	Broken pl
2021-12-04-0501			Single pl	
2021-12-04-1313			Broken pl	Broken pl
2021-12-05-0713			Single pl	
2021-12-05-1925			Single pl	Exp cutoff
2021-12-06-0534			Broken pl	Broken pl + exp cutoff
2022-01-01-1343			Single pl	
2022-01-13-1402			Single pl	
2022-01-14-1313			Broken pl	
2022-01-16-1924			Broken pl	
2022-01-18-1731			Broken pl	Broken pl
2022-01-20-0555			Broken pl	Broken pl + exp cutoff
2022-01-29-2309			Single pl	
2022-02-08-2138			Single pl	
2022-03-05-2352			Broken pl	
2022-03-10.1830			Broken pl	Broken pl + exp cutoff
2022-03-14-1714			Single pl	Broken pl

For events before October 2021, the spectrum always shows a double power-law shape or a double power-law shape with an exponential cutoff. The events where, e.g., EPT shows a single power-law shape, a break is found either when fitting STEP data alone or when fitting STEP and EPT data together, and vice versa. Only for events after October 2021, for which we only have EPT and HET data, we find cases were the spectrum does not present a spectral break, but has single power-law shape.

Table IV shows the mean values and standard deviation of the break energy E_b, the energy corresponding to the exponential cutoff E_c and the spectral indices γ_1 and γ_2 for different types of fits. For the break energies and γ_2 we include together both the break found by a broken power-law fit and a broken power-law fit with an exponential cutoff. For E_c we include together the exponential cutoff from both a single and double power-law with an exponential cutoff. The first value of γ_1 in the table is the mean of all the γ_1 values found for all events regardless of the type of mathematical model. We also count the spectral index found in single power-law fits as γ_1 in this case. For the second, third and fourth values of γ_1 we separate between broken power-law or broken power-law with an exponential cutoff, a single power-law and a single power-law with an exponential cutoff, respectively.

From table III we can see that when we fit STEP and EPT data separately for a same event, we still find, in most cases, the best mathematical model to describe the spectrum to be a broken power-law. From the values of E_b in the table it is clear that there seem to be at least two separate breaks in the spectra, one at ~ 20 keV in the STEP energy range and one at ~ 70 keV in the EPT energy range. The standard deviation of the breaks indicate that there is significant variation, especially in the fits to EPT data. In this case, we are most likely combining different breaks together (i.e. the ones at lower energies and the ones at higher energies). The high mean break energy found in EPT+HET fits might be partially caused by a few outliers in

the high HET energies. The sparse energy coverage by HET, with only four energy channels, might also play a role. Also, we only fit eight events with this combination of instruments. So, poor statistics can influence the result as well as is reflected by the standard deviation, which is almost as large as the mean value itself.

Figure 29 shows the distribution of all break energies. The left panel compares the distributions of the break energies found in STEP fits and STEP+EPT fits. As we already saw from the mean break energies, the distributions are similar and overlapping. The right panel shows instead the distribution of the the spectral breaks in EPT and STEP+EPT fits. As expected from the mean values in table IV there is a clear distinction in the two distributions, which might be an indication of two separate spectral breaks. In our analysis we are only using equations from previous studies. For this reason, we do not have a mathematical model that can fit two separate spectral breaks. When we fit STEP and EPT data together the software usually finds only the most prominent break, which is why we also fit the two instrument data separately.

Table IV. This table summarizes the mean values plus/minus the standard deviation of the break energy E_b, the energy corresponding to the exponential cutoff E_c and the spectral indices γ_1 and γ_2 found by fitting different instrument combinations to all the events in our study. For the break energies and γ_2 we include together both the break found by a broken power-law fit and a broken power-law fit with an exponential cutoff. The first value of γ_1 in the table is the mean of all the γ_1 values of all events regardless of the type of mathematical model. We also count the spectral index found in single power-law fits as γ_1 in this case. For the second, third and fourth values of γ_1 we separate between broken power-law or broken power-law with an exponential cutoff, a single power-law and a single power-law with an exponential cutoff, respectively. For two values of γ_1 (STEP and EPT fits for γ_1 of sigle power-law with an exponential cutoff) it was not possible to calculate the standard deviation because there was only one event with that specific type of fit.

Fit Parameters	Type of Fit			
	STEP	EPT	STEP+EPT	EPT+HET
E_b [keV]	19.4 ± 13.2	72.9 ± 30.5	34.0 ± 26.7	164.8 ± 147.3
E_c [keV]	63.0 ± 6.4	84.7 ± 2.7	150.7 ± 44.1	779.4 ± 599.1
γ_1 all fits	-1.79 ± 0.7	-2.46 ± 0.7	-1.67 ± 0.8	-3.18 ± 3.3
γ_1 broken pl & broken pl + cutoff	-1.83 ± 0.8	-2.36 ± 0.8	-1.67 ± 0.8	-2.59 ± 2.3
γ_1 single pl	-1.89 ± 0.5	-2.65 ± 0.7		
γ_1 single pl + cutoff	-0.91	-1.76		-2.24 ± 0.3
γ_2	–3.46 ± 1.1	-4-05 ± 1.0	-3.77 ±1.2	-5.36 ± 4.9

Figure 30 shows the comparison between the spectral breaks found by fitting either STEP and EPT separately or together for the same events. The blue diagonal line represent equality, i.e., where the value of the break is the same for the two fits. From the first panel on the left (break energy of STEP vs EPT fit) and middle panel (break energy of STEP+EPT vs EPT fit) we can see that only a few points seem to agree on the values of the break energies, these correspond to the overlapping parts of Figure 29. While it is clear from the third panel, which shows the break found in a fit to STEP data vs STEP+EPT data, that almost all the values agree with each other. We can conclude that, most of the time, the most prominent break seems to be the one at lower energies. This does not mean that there is not a break in the

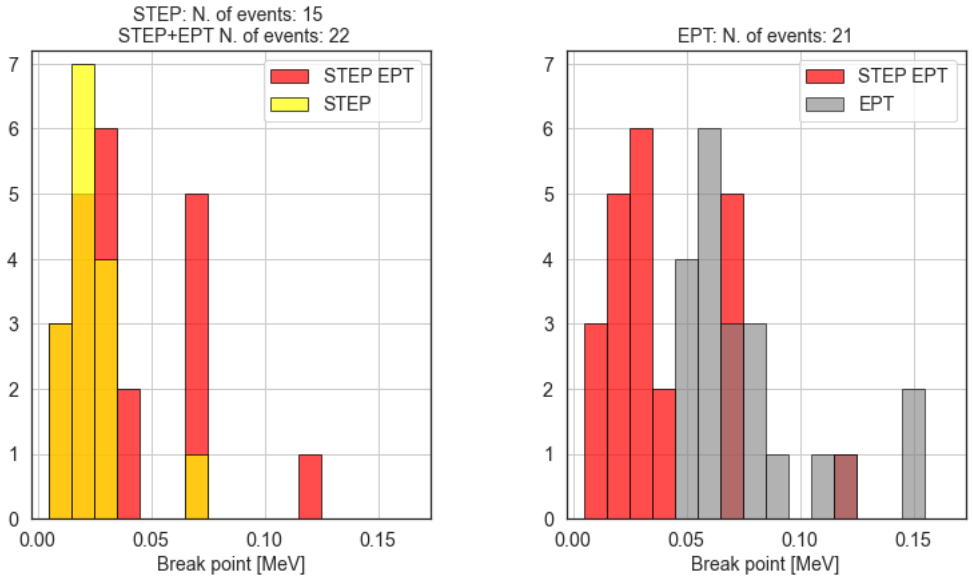

Figure 29. Distribution of the break energies. Left panel: the distribution of the break in STEP fits in yellow and the distibution of of the spectral breaks in STEP+EPT fits in red. Right panel: the distribution of the break in EPT fits in gray and the distibution of of the spectral breaks in STEP+EPT fits in red.

EPT energy range, but rather that the break is less prominent and not identified when fitting the data of both instruments together.

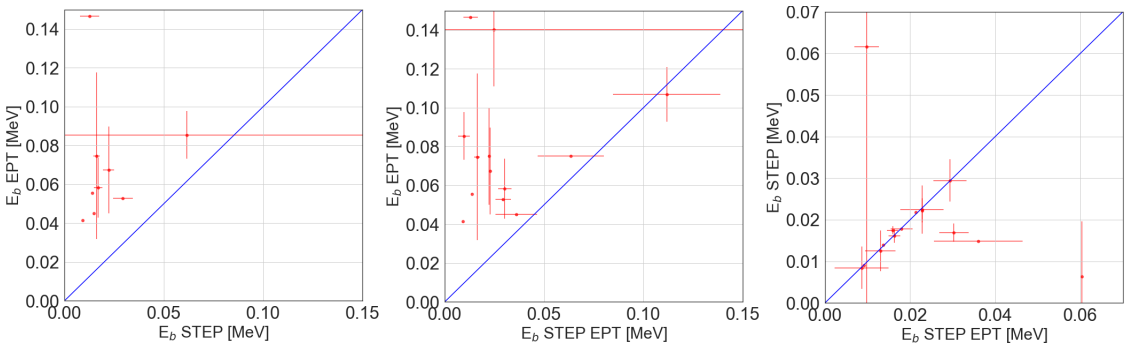

Figure 30. The left panel shows the break energy found by fitting only EPT data vs the break found by fitting STEP data. The middle panel shows the break energy found by fitting EPT data vs the one found by fitting STEP+EPT data. The right panel shows the break found when fitting STEP and EPT data together vs the one found when fitting only STEP data.

Since we found evidence that there might be two different breaks in the spectrum, we investigated whether these breaks could be related to the processes proposed in the literature, as discussed earlier in this thesis (see Section 2.2). An anti-correlation

between the intensity at the break energy and the corresponding break energy would be consistent with the break being related to Langmuir wave generation. Whereas an anti-correlation between the radial distance from the Sun and the break energies or a positive correlation of the radial distance and the difference of the spectral indices ($\gamma_2 - \gamma_1$) would be an indication of a break caused by pitch-angle scattering.

Figure 31 shows the correlation between the intensity at the break energy and the corresponding break energy for the fits to different instruments: STEP (top left panel), STEP+EPT (lower left panel), EPT (top right panel) and EPT+HET (lower right panel). ρ is the Spearman correlation coefficient (Spearman ρ) calculated with a Monte Carlo method. The Spearman correlation coefficient is usually calculated without taking into account the uncertainties. To get a more accurate description of the correlation between two parameters, given that we sometimes have large uncertainties, we use a Monte Carlo method to take the uncertainties into account. This is done by choosing a value for each parameter randomly within their uncertainty range and by calculating the correlation coefficient by iterating through these values multiple times, in our case 10000 iterations. The uncertainty of ρ is the standard deviation of all the ρ value found in the 10000 iterations of our Monte Carlo method. We consider a coefficient of over 0.6 within the error bars to be significant.

In the lower left panel we see that for the fits to STEP and EPT data together we clearly find a significant anti-correlation between the break energy and the intensity at the break energy. As previously mentioned, this anti-correlation is usually seen as an indication of a break caused by Langmuir wave generation. It is surprising however, that, as we see a correlation for STEP+EPT fits, we do not see any correlation for fits to STEP data, since the break energies found for the two types of fit are similar. One explanation for this could be that the one point in the lower left corner of the top left panel affects the correlation. Furthermore, it seems that also the presence of EPT together with STEP is needed to find this kind of breaks,

which are at higher energies compared to the STEP energy range.

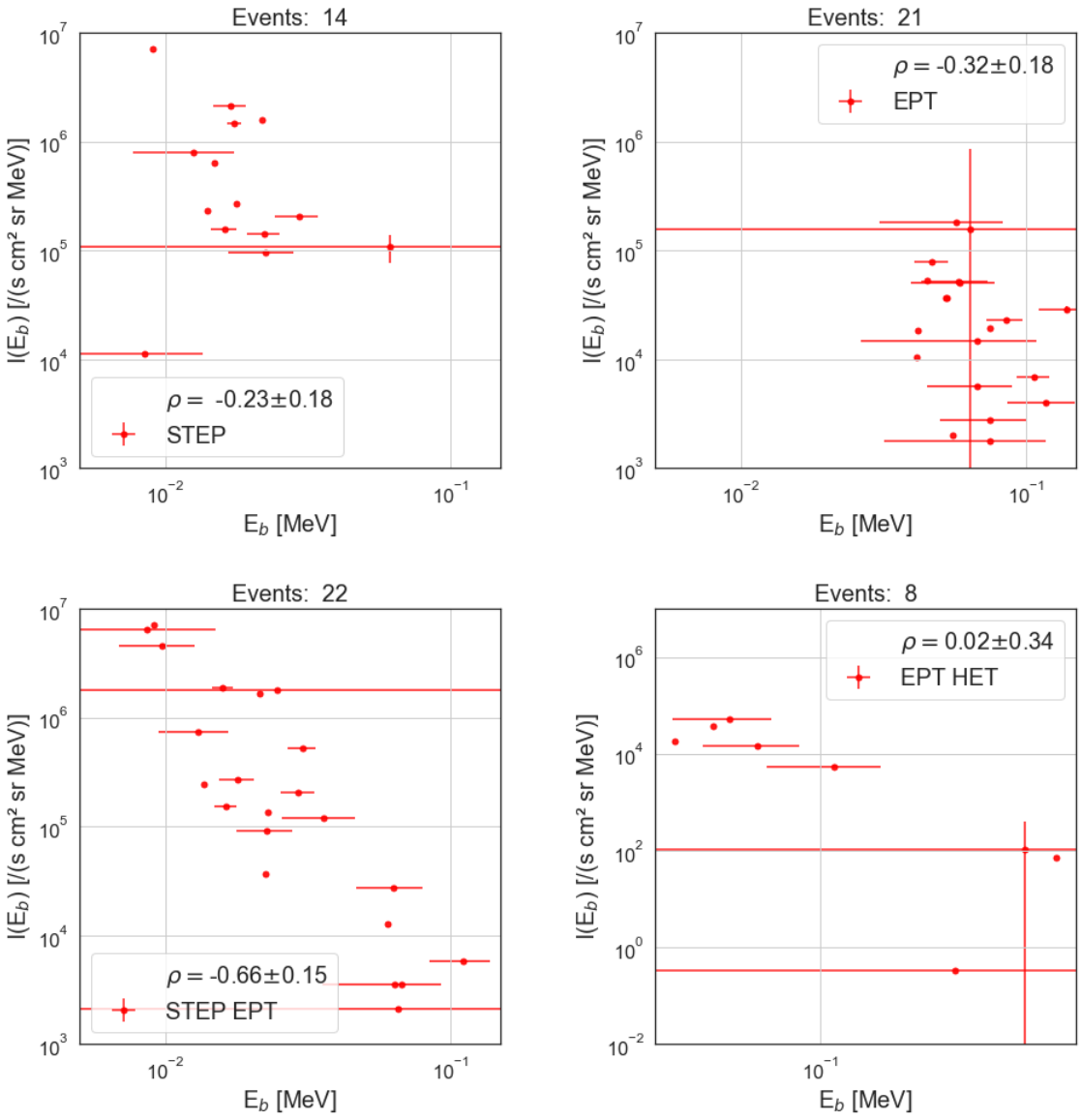

Figure 31. The Figure shows the correlation between the spectral break energies and the intensity found at the corresponding break energies for the fits to different combinations of instruments: STEP (top left panel), STEP+EPT (lower left panel), EPT (top right panel) and EPT+HET (lower right panel). ρ is the Spearman correlation coefficient calculated with a montecarlo method. We note that the bottom right panel does not have the same x- and y-axis ranges as the other panels.

Figures 32 and 33 show the relationship between the difference of the spectral indices $\gamma_2 - \gamma_1$ and the radial distance of SolO from the Sun, and relationship between the break energies and the radial distance of SolO from the Sun, respectively.

We would expect to see a positive correlation between the values in case the break is caused by pitch-angle scattering, but from the Figures it is not possible to identify such a trend in our analysis. One explanation about why we do not see any correlation could be that, since we cannot disentangle the breaks related to one or the other transport effect, we are including them all together. Some of the events are probably not related to pitch-angle scattering.

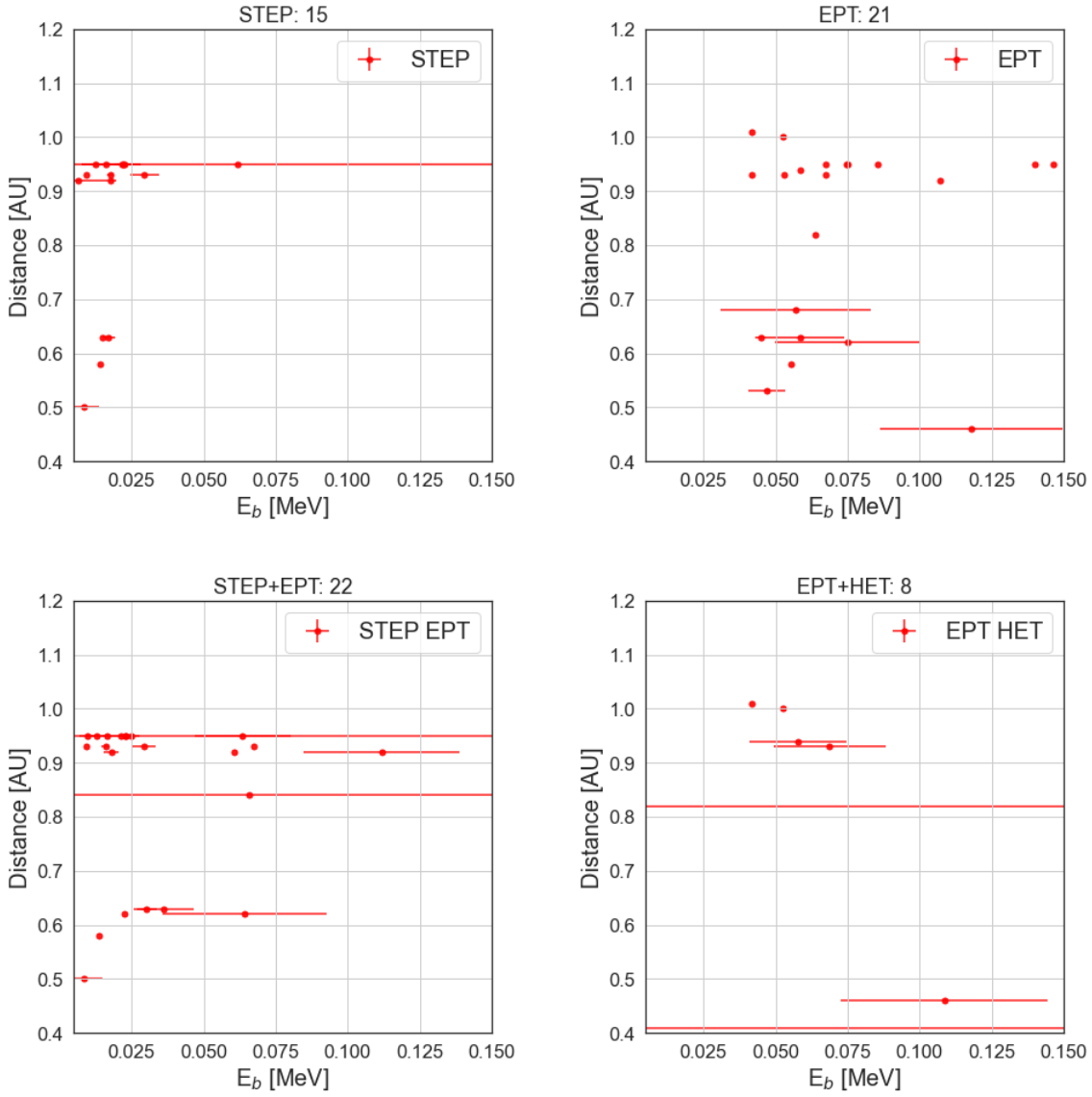

Figure 32. The Figure shows the correlation between the spectral break energies and the radial distance of SolO from the Sun. Each panel represent the fit to a different combination of instruments: STEP (top left panel), STEP+EPT (lower left panel), EPT (top right panel) and EPT+HET (lower right panel).

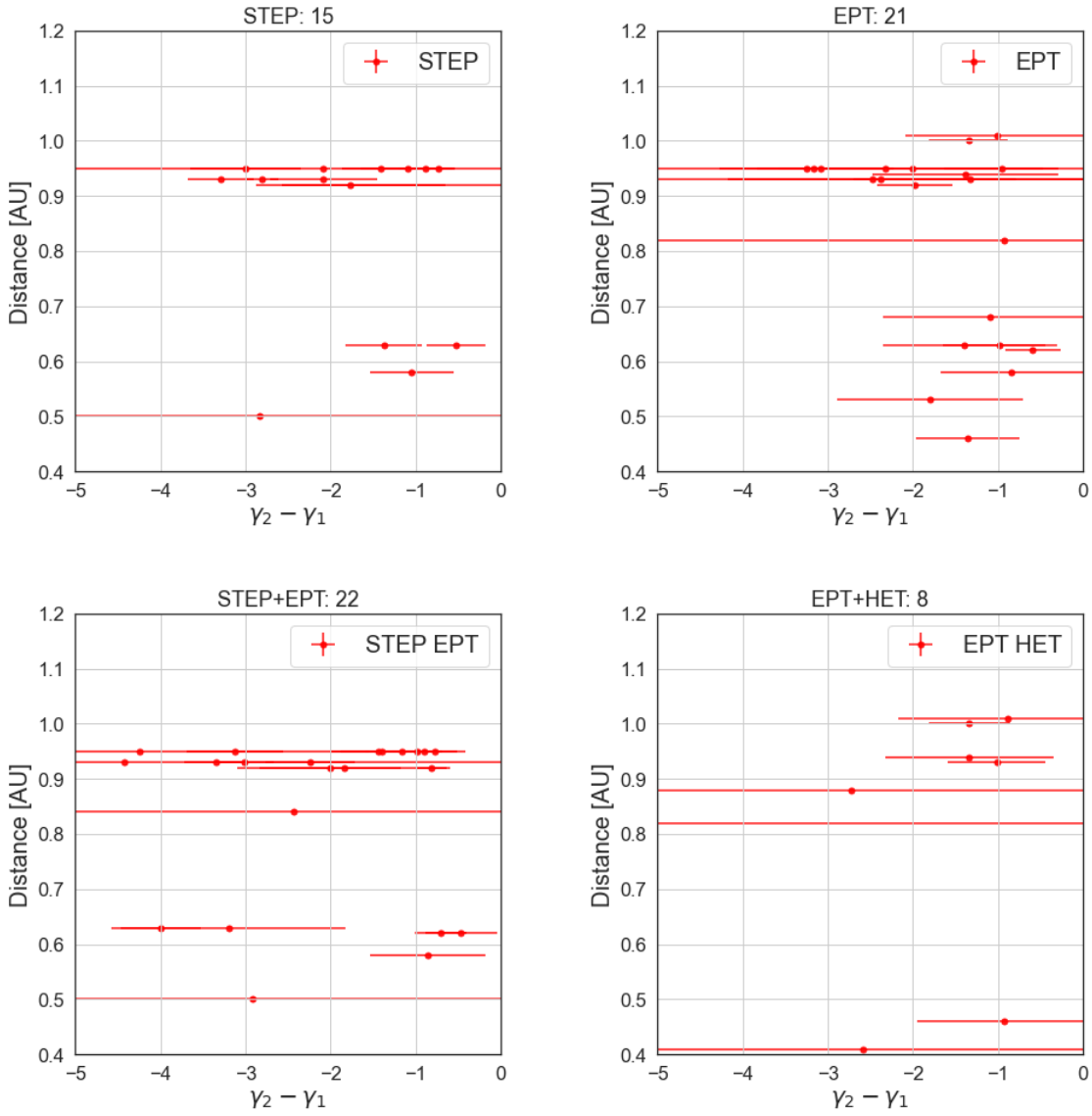

Figure 33. The Figure shows the correlation between the difference of γ_2 and γ_1 and the radial distance of SolO from the Sun. Each panel reprpesent the fit to a different combination of instruments: STEP (top left panel), STEP+EPT (lower left panel), EPT (top right panel) and EPT+HET (lower right panel).

Before deciding to exclude all the HET energy channels for events before October 2021, we also fitted STEP, EPT and HET data together and included these events also in EPT+HET fits. The distribution of the break energies found in such fits, along with the mean values and standard deviation, are shown in Appendix B. The distribution of the spectral indices γ_1 and γ_2 as well as the α value that describes the sharpness of the break, are also shown in Appendix B. We also plotted the

spectral indices against the break energies and the intensities at 0.1 MeV (which comes directly from the fits), but found no correlation. Also, we did not find any correlation between γ_1 and γ_2 (see Appendix B).

6 Discussion and Conclusion

The main focus of the thesis was investigating the presence of two separate spectral breaks and their relationship to two specific transport effects, i.e., Langmuir wave generation and pitch-angle scattering. We also compare the spectral indices found in our analysis to previous results.

The mathematical models used to fit the data in this thesis, were based on models used in previous studies (see Section 3.3.2). For this reason we did not use a triple power-law function that would potentially be able to detect two separate breaks directly. Our method to find these two possible breaks consisted in restricting the fitting process to the energy ranges of the different instruments and fitting them separately. We also fit the instrument data together to study how this impacts the break energy we find.

We fit all events with four instrument combinations: STEP, EPT, STEP+EPT and EPT+HET. For all the events before October 2021, the spectrum always has a double power-law shape for at least one of the fit combinations. The events where, e.g., EPT shows a single power-law shape, a break is found either when fitting STEP data alone or when fitting STEP and EPT data together, and vice versa. Only for events after October 2021, for which we only have EPT and HET data, we find cases where the spectrum does not present a spectral break, but has single power-law shape III). Events where the spectral shape is best described by a double power-law shape for multiple combinations of instruments can be considered as a first sign of the presence of two separate spectral breaks.

The values of the spectral indices γ_1 and γ_2 found in our study, listed in Table

IV, resemble the findings in previous studies within the uncertainties (e.g. $\gamma_1 = -1.9 \pm 0.3$ and $\gamma_2 = -3.6 \pm 0.7$ Krucker et al., 2009).

From the results in Section 5, we can conclude that we do find some evidence of two separate spectral breaks. From Figure 29 in Section 5 we can see how the breaks that we find are part of separate distributions, which are clearly not combining into the same one. The first break is in the STEP energy range, with a mean break energy of $\sim$ 20 keV $\pm$13.2 keV, and the second one is in the EPT energy range, with a mean break energy of $\sim$ 70 keV $\pm$30.5 keV (see table IV and Figure 29). While the 20 keV spectral break cannot be found by EPT only by design, the 70 keV break could still be found by STEP. The gap between the two distributions (Figure 29) is still in the energy range covered by both instruments, which suggests that there really are two different distributions. These values were found by fitting the data from the two instruments separately. When we fit the data of STEP and EPT together, as we do not have a triple power-law function, we only find the most prominent break, which in most cases, seems to be the one at lower energies. For the combined fit we get a mean break energy of $\sim$ 34.0 keV $\pm$26.7 keV. The breaks found for STEP and STEP+EPT fits are surprisingly low and not mentioned in the earlier literature.

We compared our results to the ones found by Krucker et al. (2009); Kontar and Reid (2009); Dresing et al. (2020); Strauss et al. (2020). We checked for a correlation between the break energies and the intensity at the break energies shown in Figure 31. Kontar and Reid (2009) suggest that there should be a an anti-correlation between the fluence and the break energies, if the spectral break is related to Langmuir wave generation. We are not using fluence but peak intensity at the break energy in our analysis, however, the shape of fluence spectra and peak intensity spectra are similar and the power-law indices agree within 0.2 (Krucker et al., 2007). Krucker et al. (2009) also used peak intensity (at 50 keV, close to the break energy)

instead of fluence in their analysis.

The Spearman correlation coefficient ρ is usually calculated without taking into account the uncertainties of the parameters. To get a more accurate description of the correlation between two parameters (e.g. the intensity at the break energy and the break energy), we used a Monte Carlo method to take the uncertainties into account. We consider a coefficient of over 0.6 within the error bars to be significant

We find a correlation coefficient of -0.66 $\pm$0.15 between the intensity at the break and the break energies found by fitting STEP and EPT data together. This correlation suggests that these breaks are consistent with being caused by Langmuir wave generation. As discussed previously, the breaks found by fitting STEP and EPT data together are similar to the ones found by only fitting STEP data alone, with only a few exceptions (see Figures 29, 30 and Table IV). We however do not see such correlation in the STEP fits. This might be caused by mixing of breaks related to different effects. We do not see the correlation for breaks found in the EPT either.

The low energy breaks ($\sim 20 \pm 13.2$ keV) that we found in the STEP energy range are related to highly anisotropic events. This means that we have a small electron beam which is only seen well, if we look along the magnetic field (pitch-angle 0 or 180 degrees) and we lose the beam if the pitch-angle coverage deviates. This break might not be caused by either acceleration mechanisms or transport effects, but might instead be related to the lack of pitch-angle coverage by the instruments. Figure 34 shows an example of the time series of the flux and the corresponding pitch-angle coverage for an event with a low energy spectral break. Figure 19 shows the spectrum and the fit to STEP data for the same event as Figure 34. The break energy found for the event was 23.1 ± 3.0 keV. Looking at the pitch-angle coverage of the sun telescope, which is roughly the same as the STEP viewing direction, shown in the second panel in red it departs from pitch-angle 0° and we clearly see

how it changes during the time we should see the flux peak in the STEP energies, between 19:30 and 20:30. Due to velocity dispersion the electron at lower energies are detected with a certain delay, which can get as large as hours in the STEP energy range. This deviation of the pitch-angle coverage results in a depletion of flux or the detection of an intensity peak, which is not the real one. In the example of Figure 34 we see a peak, but it is not the right one, as we lose the pitch-angle coverage.

We checked the pitch-angle coverage for all events with a low energy break in the STEP energy range. For the majority of the events we did not lose the pitch-angle coverage during the event. This problem is, however, important to take into account also in future work as it can have significant implications on the analysis of energy spectra and it is even possible that this has influenced past spectral analyses. So our finding shows that information on the pitch-angle coverage must be included when determining spectra using instruments that do not cover the whole pitch-angle space, which has never been done until now.

The presence of these breaks, in the low energy range, that are caused by loss of pitch-angle coverage may have affected the correlation between the intensity at the break energies and the corresponding break energy for the fits to STEP data.

As mentioned, we do not lose pitch-angle coverage for all events with a low energy break. So, the majority of the breaks found in the low energy range are not related to this effect. This means that our finding of two separate break energy distributions is not affected.

As mentioned earlier, Kontar and Reid (2009) suggested that there should be a an anti-correlation between the fluence and the break energies, if the spectral break is related to Langmuir wave generation. Dresing et al. (2020) did not find such a correlation in their study and suggested that the high-energy break they found was related to pitch-angle scattering instead. Strauss et al. (2020), who studied these effects on SEE spectra, argue that there should also be a correlation with the radial

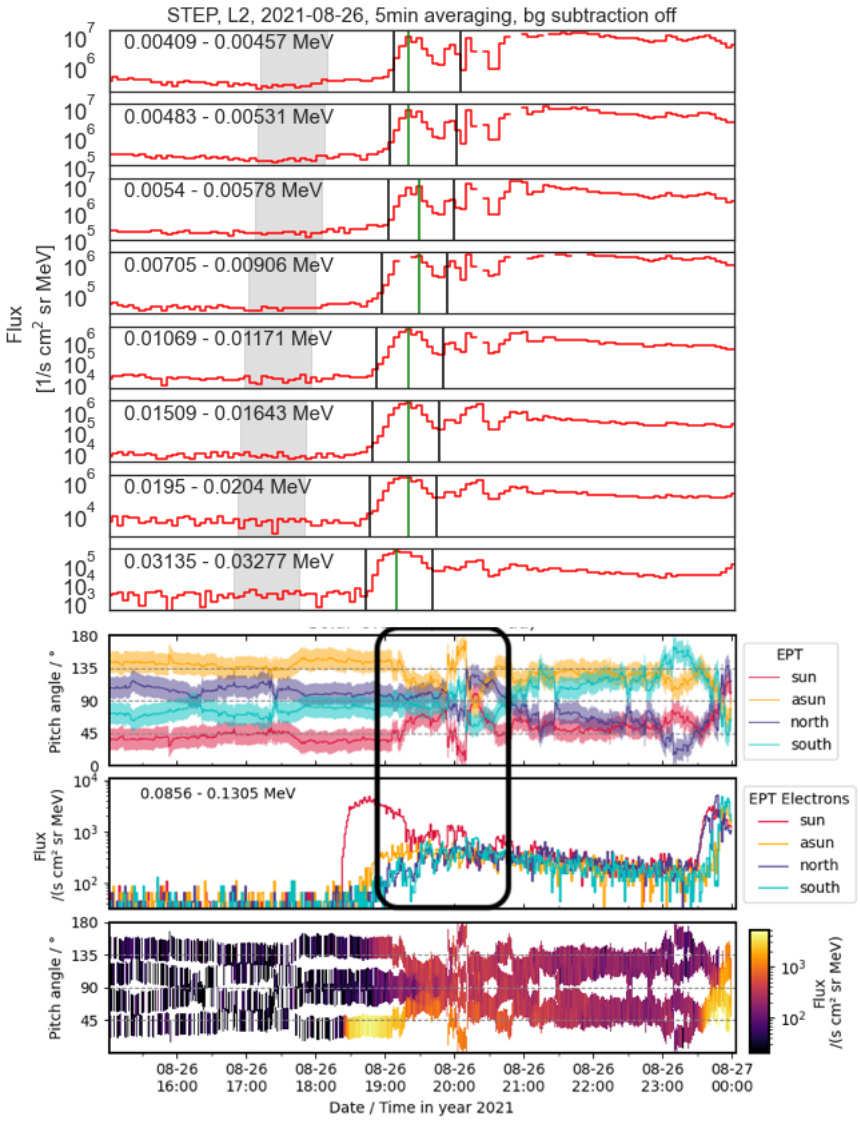

Figure 34. The figure shows the flux measured by eight different energy channels of STEP and the corresponding pitch-angle coverage for an event with a low energy break. The sun telescope (in red) corresponds to the viewing direction of STEP. We can see, in the black box, how the deviation of the pitch-angle coverage results in a depletion of the flux and detection of the wrong peak. The third panel shows the flux measured by the four viewing directions of EPT at 0.0856-0.1305 MeV. The fourth panel shows the pitch-angle coverage and the flux measured at the corresponding pitch-angle by the four viewing directions.

distance to the Sun and that these effects are accentuated the more the distance grows. We checked for such correlation but did not find any (see Figure 32). One explanation for this could again be the mixing of different breaks. The higher break

energy that we found at 70 keV is much lower than the one found by Dresing et al. (2020) at 120 keV. If these breaks are related to the same effects, one explanation could be that the energy range used in the study conducted by Dresing et al. (2020) was not broad enough to detect breaks lower than 60 keV. We have to note that it is extremely difficult to disentangle breaks related to separate effects as it is clear that the energies at which we see these breaks are overlapping.

In Section 4.3 we show how, in some cases, we find an intensity offsets between STEP and EPT. This could be caused by cross-calibration between the two instruments. Alternatively, it could have to do with the different openings of the two instruments and how beamed the pitch-angle distribution is. For STEP we do not have a single measurement, but an average of 15 pixels all together.

In our study, we found evidence of the presence of two distinct spectral breaks. We also found evidence that the lower energy spectral break is caused by Langmuir wave generation. We could not, however, find the expected dependencies for the higher break in terms of pitch-angle scattering. A solution could be removing the spectral breaks related to Langmuir wave generation from the breaks found in EPT and try the correlation to the radial distance from the Sun again. Continuing the analysis with more statistics in the future could also be helpful in finding a correlation to pitch-angle scattering as well as reinforce our findings related to breaks cause by Langmuir wave generation.

7 Outlook

One important application that can be done with the work conducted in this thesis on SEE spectra is the comparison to HXR spectra. These spectra can be compared under the assumption that the electron population measured in situ is the same as the one causing the HXRs. Both are characterized by double power-law shape and display spectral breaks at similar energies. It is also commonly accepted that HXR

spectra contain the footprint of the acceleration mechanism and that the breaks present in HXR spectra are a direct signature of this (Kontar et al., 2002; Krucker et al., 2007; Krucker et al., 2009).

The work done in this thesis can be continued and implemented even further by adding a triple power-law function, which could be instrumental in finding possible double breaks in spectra. Another important implementation would be to develop a method that takes into account the pitch-angle coverage, which is needed in order to avoid finding breaks caused by poor pitch-angle coverage. In the thesis we concentrated on SEEs but our fitting method can also be done using proton or heavy-ion spectra.

References

M. Anderson, T. Appourchaux, F. Auchère, R. Aznar Cuadrado, J. Barbay, F. Baudin, S. Beardsley, K. Bocchialini, B. Borgo, D. Bruzzi, E. Buchlin, G. Burton, V. Büchel, M. Caldwell, S. Caminade, M. Carlsson, W. Curdt, J. Davenne, J. Davila, C. E. Deforest, G. Del Zanna, D. Drummond, J. Dubau, C. Dumesnil, G. Dunn, P. Eccleston, A. Fludra, T. Fredvik, A. Gabriel, A. Giunta, A. Gottwald, D. Griffin, T. Grundy, S. Guest, M. Gyo, M. Haberreiter, V. Hansteen, R. Harrison, D. M. Hassler, S. V. H. Haugan, C. Howe, M. Janvier, R. Klein, S. Koller, T. A. Kucera, D. Kouliche, E. Marsch, A. Marshall, G. Marshall, S. A. Matthews, C. McQuirk, S. Meining, C. Mercier, N. Morris, T. Morse, G. Munro, S. Parenti, C. Pastor-Santos, H. Peter, D. Pfiffner, P. Phelan, A. Philippon, A. Richards, K. Rogers, C. Sawyer, P. Schlatter, W. Schmutz, U. Schühle, B. Shaughnessy, S. Sidher, S. K. Solanki, R. Speight, M. Spescha, N. Szwec, C. Tamiatto, L. Teriaca, W. Thompson, I. Tosh, S. Tustain, J. C. Vial, B. Walls, N. Waltham, R. Wimmer-Schweingruber, S. Woodward, P. Young, A. de Groof, A. Pacros, D. Williams, and D. Müller. The Solar Orbiter SPICE instrument. An extreme UV imaging spectrometer. *Astron. & Astrophys.*, 642:A14, October 2020. doi: 10.1051/0004-6361/201935574.

Ester Antonucci, Marco Romoli, Vincenzo Andretta, Silvano Fineschi, Petr Heinzel, J. Daniel Moses, Giampiero Naletto, Gianalfredo Nicolini, Daniele Spadaro, Luca Teriaca, Arkadiusz Berlicki, Gerardo Capobianco, Giuseppe Crescenzio, Vania Da Deppo, Mauro Focardi, Fabio Frassetto, Klaus Heerlein, Federico Landini, Enrico Magli, Andrea Marco Malvezzi, Giuseppe Massone, Radek Melich, Piergiorgio Nicolosi, Giancarlo Noci, Maurizio Pancrazzi, Maria G. Pelizzo, Luca Poletto, Clementina Sasso, Udo Schühle, Sami K. Solanki, Leonard Strachan, Roberto Susino, Giuseppe Tondello, Michela Uslenghi, Joachim Woch, Lucia Abbo, Alessandro Bemporad, Marta Casti, Sergio Dolei, Catia Grimani, Mauro Messerotti, Marco Ricci, Thomas Straus, Daniele Telloni, Paola Zuppella, Frederic Auchère, Roberto Bruno, Angela Ciaravella, Alain J. Corso, Miguel Alvarez Copano, Regina Aznar Cuadrado, Raffaella D'Amicis, Reiner Enge, Alessio Gravina, Sonja Jejčič, Philippe Lamy, Alessandro Lanzafame, Thimo Meierdierks, Ioanna Papagiannaki, Hardi Peter, German Fernandez Rico, Mewael Giday Sertsu, Jan Staub, Kanaris Tsinganos, Marco Velli, Rita Ventura, Enrico Verroi, Jean-Claude Vial, Sebastien Vives, Antonio Volpicelli, Stephan Werner, Andreas Zerr, Barbara Negri, Marco Castronuovo, Alessandro Gabrielli, Roberto Bertacin, Rita Carpentiero, Silvia Natalucci, Filippo Marliani, Marco Cesa, Philippe Laget, Danilo Morea, Stefano Pieraccini, Paolo Radaelli, Paolo Sandri, Paolo Sarra, Stefano Cesare, Felice Del Forno, Ernesto Massa, Mauro Montabone, Sergio Mottini, Daniele Quattropani, Tiziano Schillaci, Roberto Boccardo, Rosario Brando, Arianna Pandi, Cristian Baietto, Riccardo Bertone, Alberto Alvarez-Herrero, Pilar García Parejo, María Cebollero, Mauro Amoruso, and Vito Centonze. Metis: the Solar Orbiter visible light and ultraviolet coronal imager. *Astron. & Astrophys.*, 642:A10, October 2020. doi: 10.1051/0004-6361/201935338.

Markus J. Aschwanden. *Particle Acceleration and Kinematics in Solar Flares*, volume 101. 2002.

D. Band, J. Matteson, L. Ford, B. Schaefer, D. Palmer, B. Teegarden, T. Cline, M. Briggs, W. Paciesas, G. Pendleton, G. Fishman, C. Kouveliotou, C. Meegan, R. Wilson, and P. Lestrade. BATSE Observations of Gamma-Ray Burst Spectra. I. Spectral Diversity. *Astrophys. J.*, 413:281, August 1993. doi: 10.1086/172995.

L. Barnard and M. Lockwood. A survey of gradual solar energetic particle events. *Journal of Geophysical Research (Space Physics)*, 116(A5):A05103, May 2011. doi: 10.1029/2010JA016133.

A. Bruno, E. R. Christian, G. A. de Nolfo, I. G. Richardson, and J. M. Ryan. Spectral Analysis of the September 2017 Solar Energetic Particle Events. *Space Weather*, 17(3):419–437, March 2019. doi: 10.1029/2018SW002085.

H. V. Cane. Solar Flares, Type III Radio Bursts, CMEs, and Energetic Particles. In Marco Velli, Roberto Bruno, Francesco Malara, and B. Bucci, editors, *Solar Wind Ten*, volume 679 of *American Institute of Physics Conference Series*, pages 589–592, September 2003. doi: 10.1063/1.1618664.

H. V. Cane, D. V. Reames, and T. T. von Rosenvinge. The role of interplanetary shocks in the longitude distribution of solar energetic particles. *J. Geophys. Res.*, 93(A9):9555–9567, September 1988. doi: 10.1029/JA093iA09p09555.

Fernando Carcaboso-Morales, Francisco Espinosa Lara, Ignacio Cernuda, Raul Gomez-Herrero, Javier Rodriguez-Pacheco, Alberto Carrasco, Laura Rodriguez-Garcia, Angel del Pino Jimenez, Robert Wimmer-Schweingruber, Nils Janitzek, Daniel Pacheco, Glenn Mason, George Ho, Alexander Kollhoff, Zigong Xu, G. Andrews, Patrick Kuhl, Lars Berger, Sandra Eldrum, Nina Dresing, David Lario, Olga Malandraki, Angels Aran, Rami Vainio, Johan Freiherr von Forstner, Bernd Heber, Sebastian Boden, Stephan Boettcher, Manuel Prieto, O. Polo, Sebastian Sanchez Prieto, Cesar Martin-Garcia, Ali Ravanbakhsh, Christoph Terasa, Charles Schlemm, Helmut Seifert, and Teresa Nieves-Chinchilla. Solar Orbiter Energetic Particle Detector: Early Results and Science Data Center. In *AGU Fall Meeting Abstracts*, volume 2021, pages SH25B–2085, December 2021.

Federica Chiappetta, Monica Laurenza, Fabio Lepreti, and Giuseppe Consolini. Proton Energy Spectra of Energetic Storm Particle Events and Relation with Shock Parameters and Turbulence. *Astrophys. J.*, 915(1):8, July 2021. doi: 10.3847/1538-4357/abfe09.

E. W. Cliver, S. W. Kahler, and D. V. Reames. Coronal Shocks and Solar Energetic Proton Events. *Astrophys. J.*, 605(2):902–910, April 2004. doi: 10.1086/382651.

C. M. S. Cohen, G. M. Mason, E. C. Stone, R. A. Mewaldt, R. A. Leske, M. I. Desai, A. C. Cummings, T. T. von Rosenvinge, and M. E. Wiedenbeck. Solar Energetic Particle Spectra and Composition in the October/November 2003 Events. In

29th International Cosmic Ray Conference (ICRC29), Volume 1, volume 1 of *International Cosmic Ray Conference*, page 311, January 2005.

Mihir Desai and Joe Giacalone. Large gradual solar energetic particle events. *Living Reviews in Solar Physics*, 13(1):3, September 2016. doi: 10.1007/s41116-016-0002-5.

N. Dresing, R. Gómez-Herrero, B. Heber, A. Klassen, O. Malandraki, W. Dröge, and Y. Kartavykh. Statistical survey of widely spread out solar electron events observed with STEREO and ACE with special attention to anisotropies. *Astron. & Astrophys.*, 567:A27, July 2014. doi: 10.1051/0004-6361/201423789.

N. Dresing, R. Gómez-Herrero, B. Heber, A. Klassen, M. Temmer, and A. Veronig. Long-lasting injection of solar energetic electrons into the heliosphere. *Astron. & Astrophys.*, 613:A21, May 2018. doi: 10.1051/0004-6361/201731573.

N. Dresing, A. Warmuth, F. Effenberger, K. L. Klein, S. Musset, L. Glesener, and M. Brüdern. Connecting solar flare hard X-ray spectra to in situ electron spectra: A comparison of RHESSI and STEREO/SEPT observations. *Astronomy and Astrophysics*, 654:A92, oct 2021. ISSN 14320746. doi: 10.1051/0004-6361/202141365. URL `https://ui.adsabs.harvard.edu/abs/2021A{&}A...654A..92D/abstract`.

Nina Dresing, Frederic Effenberger, Raúl Gómez-Herrero, Bernd Heber, Andreas Klassen, Alexander Kollhoff, Ian Richardson, and Solveig Theesen. Statistical Results for Solar Energetic Electron Spectra Observed over 12 yr with STEREO/SEPT. *Astrophys. J.*, 889(2):143, February 2020. doi: 10.3847/1538-4357/ab64e5.

Nina Dresing, Athanasios Kouloumvakos, Rami Vainio, Alexis Rouillard, Nina Dresing, Athanasios Kouloumvakos, Rami Vainio, and Alexis Rouillard. On the Role of Coronal Shocks for Accelerating Solar Energetic Electrons. *ApJL*, 925 (2):L21, feb 2022. ISSN 0004-637X. doi: 10.3847/2041-8213/AC4CA7. URL `https://ui.adsabs.harvard.edu/abs/2022ApJ...925L..21D/abstract`.

W. Dröge, Y. Y. Kartavykh, L. Wang, D. Telloni, R. Bruno, W. Dröge, Y. Y. Kartavykh, L. Wang, D. Telloni, and R. Bruno. Transport Modeling of Interplanetary Electrons in the 2002 October 20 Solar Particle Event. *ApJ*, 869 (2):168, dec 2018. ISSN 0004-637X. doi: 10.3847/1538-4357/AAEC6C. URL `https://ui.adsabs.harvard.edu/abs/2018ApJ...869..168D/abstract`.

D. C. Ellison. Monte Carlo Simulation of charged particles upstream of the Earth's bow shock. *Geophys. Res. Lett.*, 8(9):991–994, September 1981. doi: 10.1029/GL008i009p00991.

D. C. Ellison and D. Eichler. Monte Carlo shock-like solutions to the Boltzmann equation with collective scattering. *Astrophys. J.*, 286:691–701, November 1984. doi: 10.1086/162644.

D. C. Ellison, R. Ramaty, D. C. Ellison, and R. Ramaty. Shock acceleration of electrons and ions in solar flares. *ApJ*, 298:400–408, nov 1985. ISSN 0004-637X. doi: 10.1086/163623. URL `https://ui.adsabs.harvard.edu/abs/1985ApJ...298..400E/abstract`.

Federico Fraschetti. Effect of Acceleration and Escape of Energetic Particles on Spectral Steepening at Shocks. *Astrophys. J.*, 909(1):42, March 2021. doi: 10.3847/1538-4357/abd699.

V. L. Ginzburg and V. V. Zhelezniakov. On the Possible Mechanisms of Sporadic Solar Radio Emission (Radiation in an Isotropic Plasma). , 2:653, October 1958.

R. Gómez-Herrero, N. Dresing, A. Klassen, B. Heber, D. Lario, N. Agueda, O. E. Malandraki, J. J. Blanco, J. Rodríguez-Pacheco, and S. Banjac. Circumsolar Energetic Particle Distribution on 2011 November 3. *Astrophys. J.*, 799(1):55, January 2015. doi: 10.1088/0004-637X/799/1/55.

J. T. Gosling. The solar flare myth. *J. Geophys. Res.*, 98(A11):18937–18950, November 1993. doi: 10.1029/93JA01896.

J. T. Gosling, R. M. Skoug, and D. J. McComas. Solar electron bursts at very low energies: Evidence for acceleration in the high corona? *Geophys. Res. Lett.*, 30 (13):1697, July 2003. doi: 10.1029/2003GL017079.

Fan Guo and Joe Giacalone. Particle Acceleration at a Flare Termination Shock: Effect of Large-scale Magnetic Turbulence. *Astrophys. J.*, 753(1):28, July 2012. doi: 10.1088/0004-637X/753/1/28.

T. S. Horbury, H. O'Brien, I. Carrasco Blazquez, M. Bendyk, P. Brown, R. Hudson, V. Evans, T. M. Oddy, C. M. Carr, T. J. Beek, E. Cupido, S. Bhattacharya, J. A. Dominguez, L. Matthews, V. R. Myklebust, B. Whiteside, S. D. Bale, W. Baumjohann, D. Burgess, V. Carbone, P. Cargill, J. Eastwood, G. Erdös, L. Fletcher, R. Forsyth, J. Giacalone, K. H. Glassmeier, M. L. Goldstein, T. Hoeksema, M. Lockwood, W. Magnes, M. Maksimovic, E. Marsch, W. H. Matthaeus, N. Murphy, V. M. Nakariakov, C. J. Owen, M. Owens, J. Rodriguez-Pacheco, I. Richter, P. Riley, C. T. Russell, S. Schwartz, R. Vainio, M. Velli, S. Vennerstrom, R. Walsh, R. F. Wimmer-Schweingruber, G. Zank, D. Müller, I. Zouganelis, and A. P. Walsh. The Solar Orbiter magnetometer. *Astron. & Astrophys.*, 642: A9, October 2020. doi: 10.1051/0004-6361/201937257.

R. A. Howard, A. Vourlidas, R. C. Colaninno, C. M. Korendyke, S. P. Plunkett, M. T. Carter, D. Wang, N. Rich, S. Lynch, A. Thurn, D. G. Socker, A. F. Thernisien, D. Chua, M. G. Linton, S. Koss, S. Tun-Beltran, H. Dennison, G. Stenborg, D. R. McMullin, T. Hunt, R. Baugh, G. Clifford, D. Keller, J. R. Janesick, J. Tower, M. Grygon, R. Farkas, R. Hagood, K. Eisenhauer, A. Uhl, S. Yerushalmi, L. Smith, P. C. Liewer, M. C. Velli, J. Linker, V. Bothmer, P. Rochus, J. P. Halain, P. L. Lamy, F. Auchère, R. A. Harrison, A. Rouillard, S. Patsourakos, O. C. St. Cyr, H. Gilbert, H. Maldonado, C. Mariano, and J. Cerullo. The Solar Orbiter

Heliospheric Imager (SoloHI). *Astron. & Astrophys.*, 642:A13, October 2020. doi: 10.1051/0004-6361/201935202.

S. W. Kahler. Solar Sources of Heliospheric Energetic Electron Events—Shocks or Flares? *Space Sci. Rev.*, 129(4):359–390, April 2007. doi: 10.1007/s11214-007-9143-0.

Karl-Ludwig Klein and Gérard Trottet. The Origin of Solar Energetic Particle Events: Coronal Acceleration versus Shock Wave Acceleration. *Space Sci. Rev.*, 95:215–225, January 2001. doi: 10.1023/A:1005236400689.

Eduard P. Kontar. Dynamics of electron beams in the inhomogeneous solar corona plasma. *Sol. Phys.*, 202(1):131–149, August 2001. doi: 10.1023/A:1011894830942.

Eduard P. Kontar and Hamish A.S. Reid. Onsets and spectra of impulsive solar energetic electron events observed near the earth. *Astrophysical Journal*, 695(2): L140–L144, 2009. ISSN 15384357. doi: 10.1088/0004-637X/695/2/L140. URL `https://ui.adsabs.harvard.edu/abs/2009ApJ...695L.140K/abstract`.

Eduard P. Kontar, John C. Brown, and Guillian K. McArthur. Nonuniform Target Ionization and Fitting Thick Target Electron Injection Spectra to RHESSI Data. *Sol. Phys.*, 210(1):419–429, November 2002. doi: 10.1023/A:1022494318540.

A. Kouloumvakos, A. Nindos, E. Valtonen, C. E. Alissandrakis, O. Malandraki, P. Tsitsipis, A. Kontogeorgos, X. Moussas, and A. Hillaris. Properties of solar energetic particle events inferred from their associated radio emission. *Astron. & Astrophys.*, 580:A80, August 2015. doi: 10.1051/0004-6361/201424397.

Säm Krucker, E. P. Kontar, S. Christe, and R. P. Lin. Solar Flare Electron Spectra at the Sun and near the Earth. *ApJ*, 663(2):L109–L112, July 2007. doi: 10.1086/519373.

Säm Krucker, P. H. Oakley, R. P. Lin, Säm Krucker, P. H. Oakley, and R. P. Lin. Spectra of Solar Impulsive Electron Events Observed Near Earth. *ApJ*, 691(1): 806–810, jan 2009. ISSN 0004-637X. doi: 10.1088/0004-637X/691/1/806. URL `https://ui.adsabs.harvard.edu/abs/2009ApJ...691..806K/abstract`.

Säm Krucker, H. S. Hudson, L. Glesener, S. M. White, S. Masuda, J. P. Wuelser, and R. P. Lin. Measurements of the Coronal Acceleration Region of a Solar Flare. *Astrophys. J.*, 714(2):1108–1119, May 2010. doi: 10.1088/0004-637X/714/2/1108.

Säm Krucker, G. J. Hurford, O. Grimm, S. Kögl, H. P. Gröbelbauer, L. Etesi, D. Casadei, A. Csillaghy, A. O. Benz, N. G. Arnold, F. Molendini, P. Orleanski, D. Schori, H. Xiao, M. Kuhar, N. Hochmuth, S. Felix, F. Schramka, S. Marcin, S. Kobler, L. Iseli, M. Dreier, H. J. Wiehl, L. Kleint, M. Battaglia, E. Lastufka, H. Sathiapal, K. Lapadula, M. Bednarzik, G. Birrer, St. Stutz, Ch. Wild, F. Marone, K. R. Skup, A. Cichocki, K. Ber, K. Rutkowski, W. Bujwan, G. Juchnikowski, M. Winkler, M. Darmetko, M. Michalska, K. Seweryn, A. Białek, P. Osica, J. Sylwester, M. Kowalinski, D. Ścisłowski, M. Siarkowski,

M. Stęślicki, T. Mrozek, P. Podgórski, A. Meuris, O. Limousin, O. Gevin, I. Le Mer, S. Brun, A. Strugarek, N. Vilmer, S. Musset, M. Maksimović, F. Fárník, Z. Kozáček, J. Kašparová, G. Mann, H. Önel, A. Warmuth, J. Rendtel, J. Anderson, S. Bauer, F. Dionies, J. Paschke, D. Plüschke, M. Woche, F. Schuller, A. M. Veronig, E. C. M. Dickson, P. T. Gallagher, S. A. Maloney, D. S. Bloomfield, M. Piana, A. M. Massone, F. Benvenuto, P. Massa, R. A. Schwartz, B. R. Dennis, H. F. van Beek, J. Rodríguez-Pacheco, and R. P. Lin. The Spectrometer/Telescope for Imaging X-rays (STIX). *Astron. & Astrophys.*, 642:A15, October 2020. doi: 10.1051/0004-6361/201937362.

D. Lario, R. Y. Kwon, A. Vourlidas, N. E. Raouafi, D. K. Haggerty, G. C. Ho, B. J. Anderson, A. Papaioannou, R. Gómez-Herrero, N. Dresing, and P. Riley. Longitudinal Properties of a Widespread Solar Energetic Particle Event on 2014 February 25: Evolution of the Associated CME Shock. *Astrophys. J.*, 819(1):72, March 2016. doi: 10.3847/0004-637X/819/1/72.

M. Laurenza, G. Consolini, M. Storini, G. Pallocchia, and A. Damiani. The Weibull functional form for the energetic particle spectrum at interplanetary shock waves. In *Journal of Physics Conference Series*, volume 767 of *Journal of Physics Conference Series*, page 012015, November 2016. doi: 10.1088/1742-6596/767/1/012015.

V. G. Ledenev, E. A. Zverev, and A. P. Starygin. Modeling of type III bursts dynamic spectra. *Sol. Phys.*, 222(2):299–310, August 2004. doi: 10.1023/B:SOLA.0000043564.73590.d6.

R. P. Lin. The emission and propagation of 40keV solar flare electrons. , 12:291, May 1970. doi: 10.1007/BF00227122.

R. P. Lin, D. W. Potter, D. A. Gurnett, and F. L. Scarf. Energetic electrons and plasma waves associated with a solar type III radio burst. *Astrophys. J.*, 251: 364–373, December 1981. doi: 10.1086/159471.

R. P. Lin, R. A. Mewaldt, and M. A. I. Van Hollebeke. The energy spectrum of 20 keV - 20 MeV electrons accelerated in large solar flares. *Astrophys. J.*, 253: 949–962, February 1982. doi: 10.1086/159693.

R. P. Lin, K. A. Anderson, S. Ashford, C. Carlson, D. Curtis, R. Ergun, D. Larson, J. McFadden, M. McCarthy, G. K. Parks, H. Rème, J. M. Bosqued, J. Coutelier, F. Cotin, C. D'Uston, K. P. Wenzel, T. R. Sanderson, J. Henrion, J. C. Ronnet, and G. Paschmann. A Three-Dimensional Plasma and Energetic Particle Investigation for the Wind Spacecraft. *Space Sci. Rev.*, 71(1-4):125–153, February 1995. doi: 10.1007/BF00751328.

M. Maksimovic, S. D. Bale, T. Chust, Y. Khotyaintsev, V. Krasnoselskikh, M. Kretzschmar, D. Plettemeier, H. O. Rucker, J. Souček, M. Steller, Š. Štverák, P. Trávníček, A. Vaivads, S. Chaintreuil, M. Dekkali, O. Alexandrova, P. A. Astier, G. Barbary, D. Bérard, X. Bonnin, K. Boughedada, B. Cecconi, F. Chapron, M. Chariet, C. Collin, Y. de Conchy, D. Dias, L. Guéguen, L. Lamy, V. Leray,

S. Lion, L. R. Malac-Allain, L. Matteini, Q. N. Nguyen, F. Pantellini, J. Parisot, P. Plasson, S. Thijs, A. Vecchio, I. Fratter, E. Bellouard, E. Lorfèvre, P. Danto, S. Julien, E. Guilhem, C. Fiachetti, J. Sanisidro, C. Laffaye, F. Gonzalez, B. Pontet, N. Quéruel, G. Jannet, P. Fergeau, J. Y. Brochot, G. Cassam-Chenai, T. Dudok de Wit, M. Timofeeva, T. Vincent, C. Agrapart, G. T. Delory, P. Turin, A. Jeandet, P. Leroy, J. C. Pellion, V. Bouzid, B. Katra, R. Piberne, W. Recart, O. Santolík, I. Kolmašová, V. Krupař, O. Krupařová, D. Píša, L. Uhlíř, R. Lán, J. Baše, L. Ahlèn, M. André, L. Bylander, V. Cripps, C. Cully, A. Eriksson, S. E. Jansson, E. P. G. Johansson, T. Karlsson, W. Puccio, J. Břínek, H. Öttacher, M. Panchenko, M. Berthomier, K. Goetz, P. Hellinger, T. S. Horbury, K. Issautier, E. Kontar, S. Krucker, O. Le Contel, P. Louarn, M. Martinović, C. J. Owen, A. Retino, J. Rodríguez-Pacheco, F. Sahraoui, R. F. Wimmer-Schweingruber, A. Zaslavsky, and I. Zouganelis. The Solar Orbiter Radio and Plasma Waves (RPW) instrument. *Astron. & Astrophys.*, 642:A12, October 2020. doi: 10.1051/0004-6361/201936214.

G. Mann, V. N. Melnik, H. O. Rucker, A. A. Konovalenko, and A. I. Brazhenko. Radio signatures of shock-accelerated electron beams in the solar corona. *Astron. & Astrophys.*, 609:A41, January 2018. doi: 10.1051/0004-6361/201730546.

S. Masuda, T. Kosugi, H. Hara, S. Tsuneta, and Y. Ogawara. A loop-top hard X-ray source in a compact solar flare as evidence for magnetic reconnection. , 371(6497): 495–497, October 1994. doi: 10.1038/371495a0.

R. A. Mewaldt, C. M. S. Cohen, A. W. Labrador, R. A. Leske, G. M. Mason, M. I. Desai, M. D. Looper, J. E. Mazur, R. S. Selesnick, and D. K. Haggerty. Proton, helium, and electron spectra during the large solar particle events of October-November 2003. *Journal of Geophysical Research (Space Physics)*, 110 (A9):A09S18, September 2005. doi: 10.1029/2005JA011038.

R. A. Mewaldt, M. D. Looper, C. M. S. Cohen, D. K. Haggerty, A. W. Labrador, R. A. Leske, G. M. Mason, J. E. Mazur, and T. T. von Rosenvinge. Energy Spectra, Composition, and Other Properties of Ground-Level Events During Solar Cycle 23. *Space Sci. Rev.*, 171(1-4):97–120, October 2012. doi: 10.1007/s11214-012-9884-2.

R. A. Mewaldt, C. M. S. Cohen, G. M. Mason, T. T. von Rosenvinge, R. A. Leske, J. G. Luhmann, D. Odstrcil, and A. Vourlidas. Solar energetic particles and their variability from the sun and beyond. In Gary P. Zank, Joe Borovsky, Roberto Bruno, Jonathan Cirtain, Steve Cranmer, Heather Elliott, Joe Giacalone, Walter Gonzalez, Gang Li, Eckart Marsch, Ebehard Moebius, Nick Pogorelov, Jim Spann, and Olga Verkhoglyadova, editors, *Solar Wind 13*, volume 1539 of *American Institute of Physics Conference Series*, pages 116–121, June 2013. doi: 10.1063/1.4811002.

Rositsa Miteva, Susan W. Samwel, and Vratislav Krupar. Solar energetic particles and radio burst emission. *Journal of Space Weather and Space Climate*, 7:A37, December 2017. doi: 10.1051/swsc/2017035.

Kevin J. Mueller, Larry Di Girolamo, Mike Fromm, and Steven P. Palm. Stereo observations of polar stratospheric clouds. *Geophys. Res. Lett.*, 35(17):L17813, September 2008. doi: 10.1029/2008GL033792.

Müller, D., St. Cyr, O. C., Zouganelis, I., Gilbert, H. R., Marsden, R., Nieves-Chinchilla, T., Antonucci, E., Auchère, F., Berghmans, D., Horbury, T. S., Howard, R. A., Krucker, S., Maksimovic, M., Owen, C. J., Rochus, P., Rodriguez-Pacheco, J., Romoli, M., Solanki, S. K., Bruno, R., Carlsson, M., Fludra, A., Harra, L., Hassler, D. M., Livi, S., Louarn, P., Peter, H., Schühle, U., Teriaca, L., del Toro Iniesta, J. C., Wimmer-Schweingruber, R. F., Marsch, E., Velli, M., De Groof, A., Walsh, A., and Williams, D. The solar orbiter mission - science overview. *A&A*, 642:A1, 2020. doi: 10.1051/0004-6361/202038467. URL `https://doi.org/10.1051/0004-6361/202038467`.

C. J. Owen, R. Bruno, S. Livi, P. Louarn, K. Al Janabi, F. Allegrini, C. Amoros, R. Baruah, A. Barthe, M. Berthomier, S. Bordon, C. Brockley-Blatt, C. Brysbaert, G. Capuano, M. Collier, R. DeMarco, A. Fedorov, J. Ford, V. Fortunato, I. Fratter, A. B. Galvin, B. Hancock, D. Heirtzler, D. Kataria, L. Kistler, S. T. Lepri, G. Lewis, C. Loeffler, W. Marty, R. Mathon, A. Mayall, G. Mele, K. Ogasawara, M. Orlandi, A. Pacros, E. Penou, S. Persyn, M. Petiot, M. Phillips, L. Přech, J. M. Raines, M. Reden, A. P. Rouillard, A. Rousseau, J. Rubiella, H. Seran, A. Spencer, J. W. Thomas, J. Trevino, D. Verscharen, P. Wurz, A. Alapide, L. Amoruso, N. André, C. Anekallu, V. Arciuli, K. L. Arnett, R. Ascolese, C. Bancroft, P. Bland, M. Brysch, R. Calvanese, M. Castronuovo, I. Čermák, D. Chornay, S. Clemens, J. Coker, G. Collinson, R. D'Amicis, I. Dandouras, R. Darnley, D. Davies, G. Davison, A. De Los Santos, P. Devoto, G. Dirks, E. Edlund, A. Fazakerley, M. Ferris, C. Frost, G. Fruit, C. Garat, V. Génot, W. Gibson, J. A. Gilbert, V. de Giosa, S. Gradone, M. Hailey, T. S. Horbury, T. Hunt, C. Jacquey, M. Johnson, B. Lavraud, A. Lawrenson, F. Leblanc, W. Lockhart, M. Maksimovic, A. Malpus, F. Marcucci, C. Mazelle, F. Monti, S. Myers, T. Nguyen, J. Rodriguez-Pacheco, I. Phillips, M. Popecki, K. Rees, S. A. Rogacki, K. Ruane, D. Rust, M. Salatti, J. A. Sauvaud, M. O. Stakhiv, J. Stange, T. Stubbs, T. Taylor, J. D. Techer, G. Terrier, R. Thibodeaux, C. Urdiales, A. Varsani, A. P. Walsh, G. Watson, P. Wheeler, G. Willis, R. F. Wimmer-Schweingruber, B. Winter, J. Yardley, and I. Zouganelis. The Solar Orbiter Solar Wind Analyser (SWA) suite. *Astron. & Astrophys.*, 642:A16, October 2020. doi: 10.1051/0004-6361/201937259.

E. N. Parker. Dynamics of the Interplanetary Gas and Magnetic Fields. *Astrophys. J.*, 128:664, November 1958. doi: 10.1086/146579.

Donald V. Reames. Particle acceleration at the sun and in the heliosphere. *Space Science Reviews*, 90(3-4):413–491, 1999. ISSN 00386308. doi: 10.1023/A:1005105831781.

Donald V. Reames. The Two Sources of Solar Energetic Particles. *Space Sci. Rev.*, 175(1-4):53–92, June 2013. doi: 10.1007/s11214-013-9958-9.

P. Rochus, F. Auchère, D. Berghmans, L. Harra, W. Schmutz, U. Schühle, P. Addison, T. Appourchaux, R. Aznar Cuadrado, D. Baker, J. Barbay, D. Bates, A. Ben-Moussa, M. Bergmann, C. Beurthe, B. Borgo, K. Bonte, M. Bouzit, L. Bradley, V. Büchel, E. Buchlin, J. Büchner, F. Cabé, L. Cadiergues, M. Chaigneau, B. Chares, C. Choque Cortez, P. Coker, M. Condamin, S. Coumar, W. Curdt, J. Cutler, D. Davies, G. Davison, J. M. Defise, G. Del Zanna, F. Delmotte, V. Delouille, L. Dolla, C. Dumesnil, F. Dürig, R. Enge, S. François, J. J. Fourmond, J. M. Gillis, B. Giordanengo, S. Gissot, L. M. Green, N. Guerreiro, A. Guilbaud, M. Gyo, M. Haberreiter, A. Hafiz, M. Hailey, J. P. Halain, J. Hansotte, C. Hecquet, K. Heerlein, M. L. Hellin, S. Hemsley, A. Hermans, V. Hervier, J. F. Hochedez, Y. Houbrechts, K. Ihsan, L. Jacques, A. Jérôme, J. Jones, M. Kahle, T. Kennedy, M. Klaproth, M. Kolleck, S. Koller, E. Kotsialos, E. Kraaikamp, P. Langer, A. Lawrenson, J. C. Le Clech', C. Lenaerts, S. Liebecq, D. Linder, D. M. Long, B. Mampaey, D. Markiewicz-Innes, B. Marquet, E. Marsch, S. Matthews, E. Mazy, A. Mazzoli, S. Meining, E. Meltchakov, R. Mercier, S. Meyer, M. Monecke, F. Monfort, G. Morinaud, F. Moron, L. Mountney, R. Müller, B. Nicula, S. Parenti, H. Peter, D. Pfiffner, A. Philippon, I. Phillips, J. Y. Plesseria, E. Pylyser, F. Rabecki, M. F. Ravet-Krill, J. Rebellato, E. Renotte, L. Rodriguez, S. Roose, J. Rosin, L. Rossi, P. Roth, F. Rouesnel, M. Roulliay, A. Rousseau, K. Ruane, J. Scanlan, P. Schlatter, D. B. Seaton, K. Silliman, S. Smit, P. J. Smith, S. K. Solanki, M. Spescha, A. Spencer, K. Stegen, Y. Stockman, N. Szwec, C. Tamiatto, J. Tandy, L. Teriaca, C. Theobald, I. Tychon, L. van Driel-Gesztelyi, C. Verbeeck, J. C. Vial, S. Werner, M. J. West, D. Westwood, T. Wiegelmann, G. Willis, B. Winter, A. Zerr, X. Zhang, and A. N. Zhukov. The Solar Orbiter EUI instrument: The Extreme Ultraviolet Imager. *Astron. & Astrophys.*, 642: A8, October 2020. doi: 10.1051/0004-6361/201936663.

J. Rodríguez-Pacheco, R. F. Wimmer-Schweingruber, G. M. Mason, G. C. Ho, S. Sánchez-Prieto, M. Prieto, C. Martín, H. Seifert, G. B. Andrews, S. R. Kulkarni, L. Panitzsch, S. Boden, S. I. Böttcher, I. Cernuda, R. Elftmann, F. Espinosa Lara, R. Gómez-Herrero, C. Terasa, J. Almena, S. Begley, E. Böhm, J. J. Blanco, W. Boogaerts, A. Carrasco, R. Castillo, A. da Silva Fariña, V. de Manuel González, C. Drews, A. R. Dupont, S. Eldrum, C. Gordillo, O. Gutiérrez, D. K. Haggerty, J. R. Hayes, B. Heber, M. E. Hill, M. Jüngling, S. Kerem, V. Knierim, J. Köhler, S. Kolbe, A. Kulemzin, D. Lario, W. J. Lees, S. Liang, A. Martínez Hellín, D. Meziat, A. Montalvo, K. S. Nelson, P. Parra, R. Paspirgilis, A. Ravanbakhsh, M. Richards, O. Rodríguez-Polo, A. Russu, I. Sánchez, C. E. Schlemm, B. Schuster, L. Seimetz, J. Steinhagen, J. Tammen, K. Tyagi, T. Varela, M. Yedla, J. Yu, N. Agueda, A. Aran, T. S. Horbury, B. Klecker, K. L. Klein, E. Kontar, S. Krucker, M. Maksimovic, O. Malandraki, C. J. Owen, D. Pacheco, B. Sanahuja, R. Vainio, J. J. Connell, S. Dalla, W. Dröge, O. Gevin, N. Gopalswamy, Y. Y. Kartavykh, K. Kudela, O. Limousin, P. Makela, G. Mann, H. Önel, A. Posner, J. M. Ryan, J. Soucek, S. Hofmeister, N. Vilmer, A. P. Walsh, L. Wang, M. E. Wiedenbeck, K. Wirth, and Q. Zong. The Energetic Particle Detector. Energetic particle instrument suite for the Solar Orbiter mission. *Astron. & Astrophys.*, 642:A7, October 2020. doi: 10.1051/0004-6361/201935287.

S. K. Solanki, J. C. del Toro Iniesta, J. Woch, A. Gandorfer, J. Hirzberger, A. Alvarez-Herrero, T. Appourchaux, V. Martínez Pillet, I. Pérez-Grande, E. Sanchis Kilders, W. Schmidt, J. M. Gómez Cama, H. Michalik, W. Deutsch, G. Fernandez-Rico, B. Grauf, L. Gizon, K. Heerlein, M. Kolleck, A. Lagg, R. Meller, R. Müller, U. Schühle, J. Staub, K. Albert, M. Alvarez Copano, U. Beckmann, J. Bischoff, D. Busse, R. Enge, S. Frahm, D. Germerott, L. Guerrero, B. Löptien, T. Meierdierks, D. Oberdorfer, I. Papagiannaki, S. Ramanath, J. Schou, S. Werner, D. Yang, A. Zerr, M. Bergmann, J. Bochmann, J. Heinrichs, S. Meyer, M. Monecke, M. F. Müller, M. Sperling, D. Álvarez García, B. Aparicio, M. Balaguer Jiménez, L. R. Bellot Rubio, J. P. Cobos Carracosa, F. Girela, D. Hernández Expósito, M. Herranz, P. Labrousse, A. López Jiménez, D. Orozco Suárez, J. L. Ramos, J. Barandiarán, L. Bastide, C. Campuzano, M. Cebollero, B. Dávila, A. Fernández-Medina, P. García Parejo, D. Garranzo-García, H. Laguna, J. A. Martín, R. Navarro, A. Núñez Peral, M. Royo, A. Sánchez, M. Silva-López, I. Vera, J. Villanueva, J. J. Fourmond, C. Ruiz de Galarreta, M. Bouzit, V. Hervier, J. C. Le Clec'h, N. Szwec, M. Chaigneau, V. Buttice, C. Dominguez-Tagle, A. Philippon, P. Boumier, R. Le Cocguen, G. Baranjuk, A. Bell, Th. Berkefeld, J. Baumgartner, F. Heidecke, T. Maue, E. Nakai, T. Scheiffelen, M. Sigwarth, D. Soltau, R. Volkmer, J. Blanco Rodríguez, V. Domingo, A. Ferreres Sabater, J. L. Gasent Blesa, P. Rodríguez Martínez, D. Osorno Caudel, J. Bosch, A. Casas, M. Carmona, A. Herms, D. Roma, G. Alonso, A. Gómez-Sanjuan, J. Piqueras, I. Torralbo, B. Fiethe, Y. Guan, T. Lange, H. Michel, J. A. Bonet, S. Fahmy, D. Müller, and I. Zouganelis. The Polarimetric and Helioseismic Imager on Solar Orbiter. *Astron. & Astrophys.*, 642:A11, October 2020. doi: 10.1051/0004-6361/201935325.

R. D. Strauss, N. Dresing, A. Kollhoff, M. Brüdern, R. D. Strauss, N. Dresing, A. Kollhoff, and M. Brüdern. On the Shape of SEP Electron Spectra: The Role of Interplanetary Transport. *ApJ*, 897(1):24, jun 2020. ISSN 0004-637X. doi: 10.3847/1538-4357/AB91B0. URL `https://ui.adsabs.harvard.edu/abs/2020ApJ...897...24S/abstract`.

Loukas Vlahos, Anastasios Anastasiadis, Athanasios Papaioannou, Athanasios Kouloumvakos, and Heinz Isliker. Sources of solar energetic particles. *Philosophical Transactions of the Royal Society of London Series A*, 377(2148):20180095, July 2019. doi: 10.1098/rsta.2018.0095.

L. Wang, R. P. Lin, S. Krucker, and J. T. Gosling. Evidence for double injections in scatter-free solar impulsive electron events. *Geophys. Res. Lett.*, 33(3):L03106, February 2006. doi: 10.1029/2005GL024434.

J. P. Wild, S. F. Smerd, and A. A. Weiss. Solar Bursts. , 1:291, January 1963. doi: 10.1146/annurev.aa.01.090163.001451.

R. F. Wimmer-Schweingruber, N. P. Janitzek, D. Pacheco, I. Cernuda, F. Espinosa Lara, R. Gómez-Herrero, G. M. Mason, R. C. Allen, Z. G. Xu, F. Carcaboso,

A. Kollhoff, P. Kühl, J. L. Freiherr von Forstner, L. Berger, J. Rodriguez-Pacheco, G. C. Ho, G. B. Andrews, V. Angelini, A. Aran, S. Boden, S. I. Böttcher, A. Carrasco, N. Dresing, S. Eldrum, R. Elftmann, V. Evans, O. Gevin, J. Hayes, B. Heber, T. S. Horbury, S. R. Kulkarni, D. Lario, W. J. Lees, O. Limousin, O. E. Malandraki, C. Martín, H. O'Brien, M. Prieto Mateo, A. Ravanbakhsh, O. Rodriguez-Polo, S. Sánchez Prieto, C. E. Schlemm, H. Seifert, J. C. Terasa, K. Tyagi, R. Vainio, A. Walsh, and M. K. Yedla. First year of energetic particle measurements in the inner heliosphere with Solar Orbiter's Energetic Particle Detector. *Astron. & Astrophys.*, 656:A22, December 2021. doi: 10.1051/0004-6361/202140940.

Feiyu Yu, Xiangliang Kong, Fan Guo, Wenlong Liu, Zelong Jiang, Yao Chen, and Joe Giacalone. Double-power-law Feature of Energetic Particles Accelerated at Coronal Shocks. *The Astrophysical Journal Letters*, 925(2):L13, feb 2022. ISSN 2041-8205. doi: 10.3847/2041-8213/ac4cb3. URL `https://ui.adsabs.harvard.edu/abs/2022ApJ...925L..13Y/abstract`.

Appendix A

Figures 35 and 36 show the comparison between the values of the spectral index γ_1 and the goodness of the fit χ^2, respectively, for different time averagings used to determine the peak intensities for the spectra of the data. The first column of panels on the left, in both figures, shows the difference between values found for one minute averaged data vs the value found for two minutes averaged data. The middle column of panels shows the difference between values found for one minute averaged data vs the value found for five minutes averaged data and the column of panels on the right shows the difference between values found for two minutes averaged data vs the value found for two minutes averaged data. Each row represents the fit to a different combination of instruments: EPT, STEP, STEP+EPT and EPT+HET, respectively. The black line represents equality so, the closer the data points are to the line, the more similar they are. The blue line represents the mean value of the difference of the γ_1 values, for Figure 35, χ^2 values, for Figure 36 . The blue area represents the standard deviation of the difference between the values in each panel.

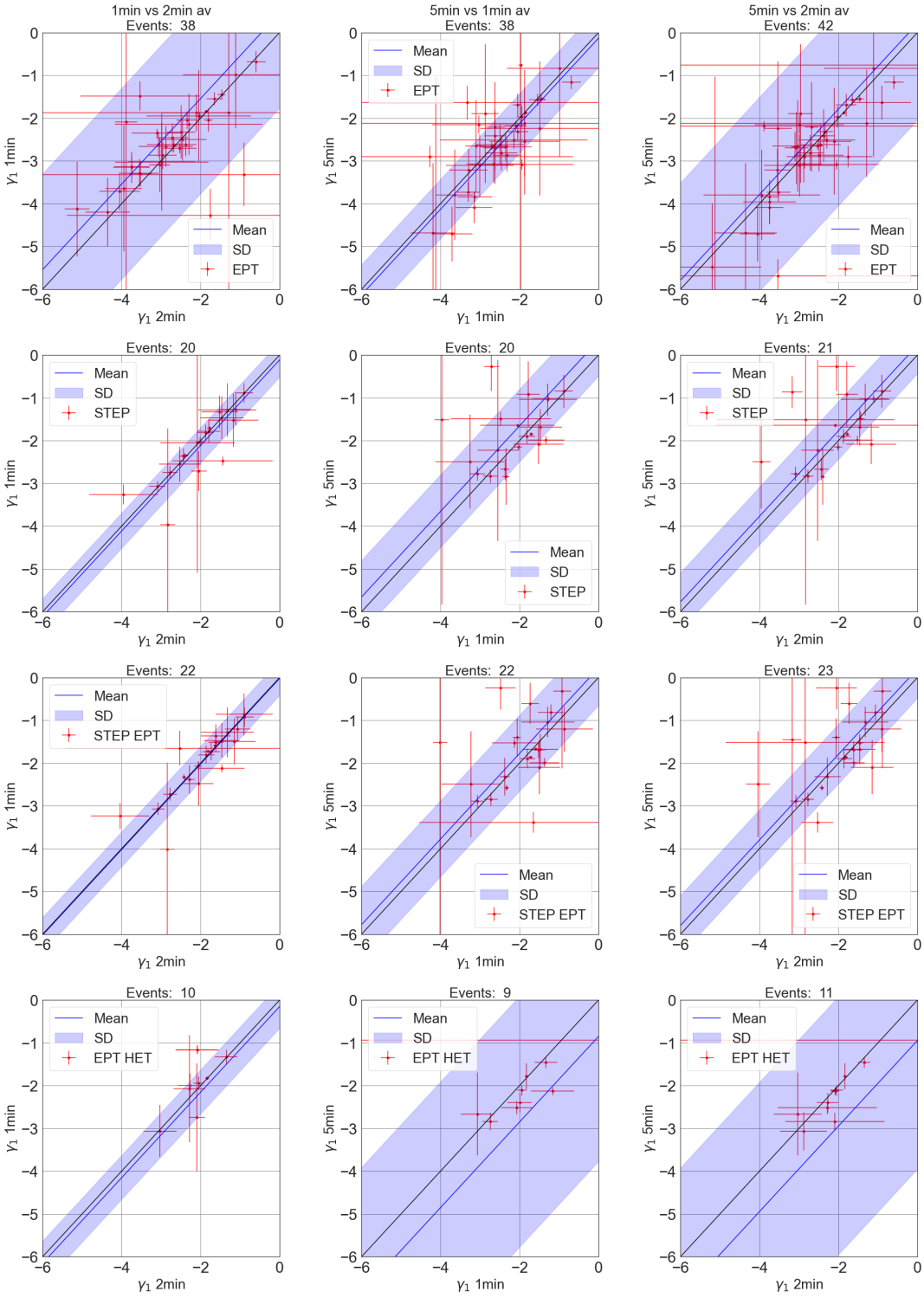

Figure 35. The Figure shows the comparison between the values of the spectral index γ_1 for different averagings of the data. We use one, two and five minutes averaged data. Each column of panels shows the values of γ_1 found for the different averagings compared to each other. Each row represents the fit to a different combination of instruments: EPT, STEP, STEP+EPT and EPT+HET, respectively. The black line represents equality so, the closer the data points are to the line, the more similar they are. The blue line represents the mean value of the difference of the γ_1 values. The blue area represents the standard deviation of the difference between the γ_1 values in each panel.

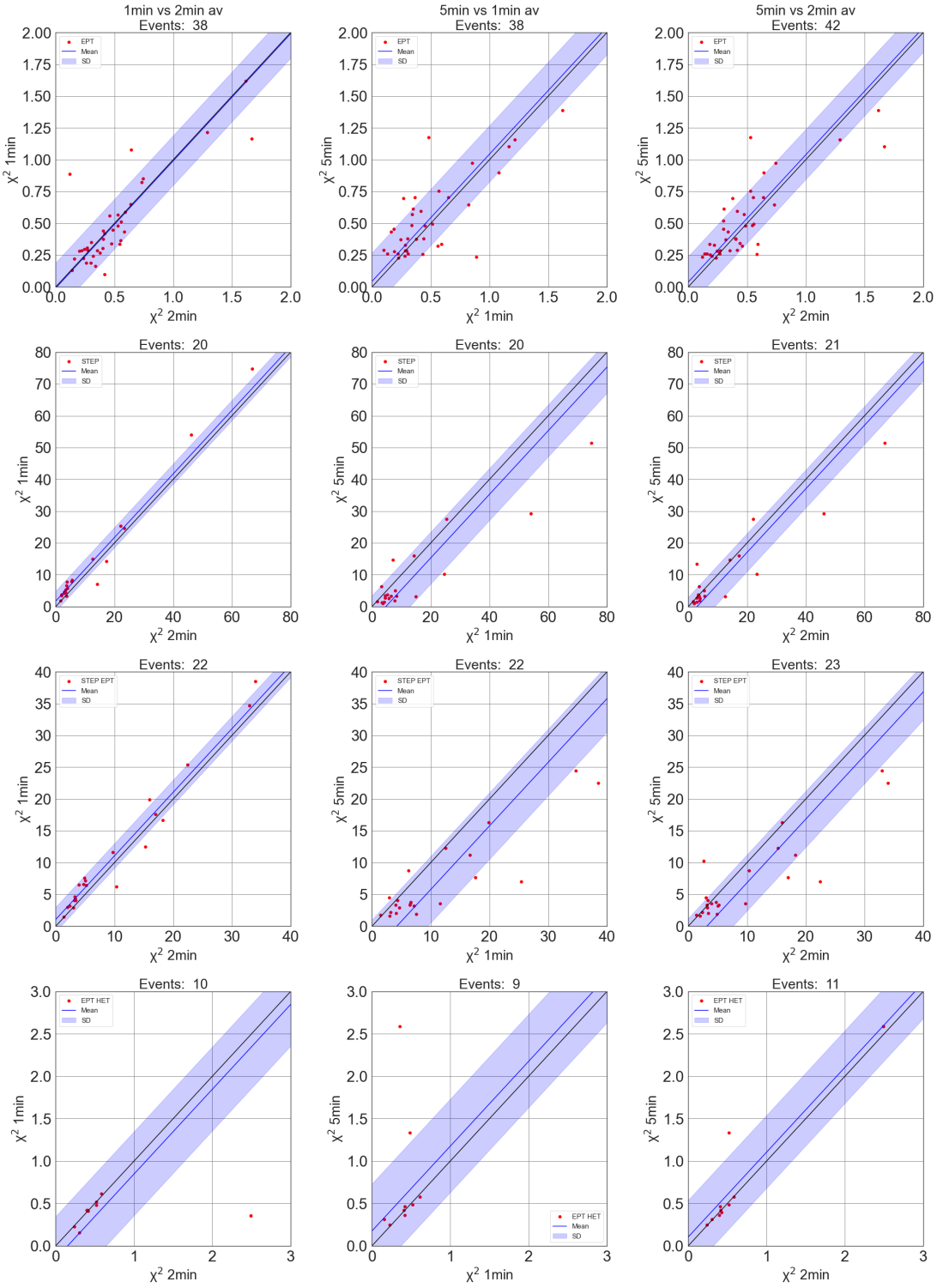

Figure 36. The Figure shows the comparison between the values of the goodness of the fit represented by the reduced χ^2 for different averagings of the data. We use one, two and five minutes averaged data. Each column of panels shows the values of χ^2 found for the different averagings compared to each other. Each row represents the fit to a different combination of instruments: EPT, STEP, STEP+EPT and EPT+HET, respectively. The black line represents equality so, the closer the data points are to the line, the more similar they are. The blue line represents the mean value of the difference of the χ^2 values. The blue area represents the standard deviation of the difference between the χ^2 values in each panel.

Appendix B

The spectra fitting was originally done also using HET data before October 2021. Figure 37 shows the distribution of the spectral breaks found by fitting different combinations of instruments including the HET data. The first HET energy channel is always excluded from the fits because it clearly does not follow the trend of the rest of the data points. The top left panel shows the break energies found with a fit to STEP+EPT+HET data, the bottom left panel shows the same for fits to only STEP data, the bottom right panel to EPT+HET data and the top right panel shows the breaks found for EPT data in purple and the ones for STEP+EPT data in orange. From the distribution of the break energies we can clearly see how this varies depending on whether we fit STEP or EPT separately or together. As mentioned in Section 4.2, when we fit the instruments together, the fitting software finds the most prominent break, which seems to be the one at lower energies.

Fitting STEP and EPT together with or without HET does not seem to have any effect of the distribution of the break energies. This means that even without STEP+EPT+HET fits in our analysis, we are not loosing any important statistics. Above each panel we also show the number of events that were fit using a specific instrument or combination of instruments and the mean break break energy for each fit type.

Table V summarizes the mean break energy found for each type of fit along with the corresponding standard deviation.

Table V. Break energies for all fits.

	Type of Fit				
	STEP	EPT	STEP+EPT	STEP+EPT+HET	EPT+HET
Mean	19.4	72.9	34.0	40.9	259.9
Standard Deviation	13.2	30.5	26.7	29.8	445.4

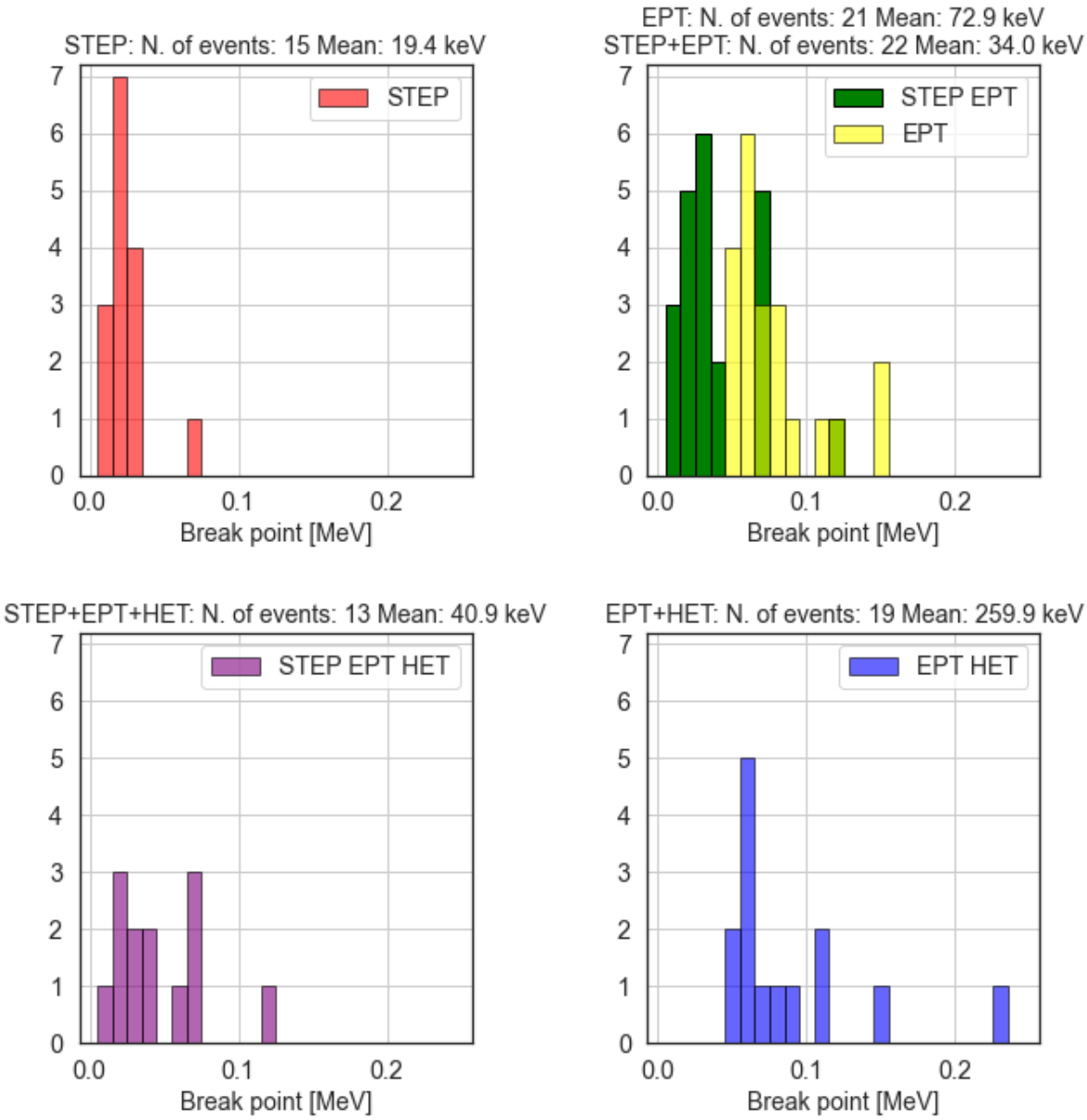

Figure 37. Distribution of the break energies including HET. Top left panel: fit to STEP data. Top right panel: fit to EPT data in yellow and STEP+EPT data in green. Bottom left panel: fit to STEP+EPT+HET data. Bottom right panel: fit to EPT+HET data.

Figure 38 shows the distribution of the spectral index γ_1 for all events including all fit types (i.e. single power-law, broken power-law, single power-law+exponential cutoff and broken power-law+exponential cutoff). The top left panel shows the distribution found in fits to STEP data, the bottom left panel shows the distribution of the values for a fit to STEP+EPT data, the top right panel shows the distribution

of the values for a fit to only EPT data and the bottom right panel shows the distribution of the values for a fit to EPT+HET data. Above each panel we also indicate the mean value found for each fit as well as the number of events fit with the specific combination of instruments corresponding to the panel. We also include the spectral index found for single power-law fits as γ_1.

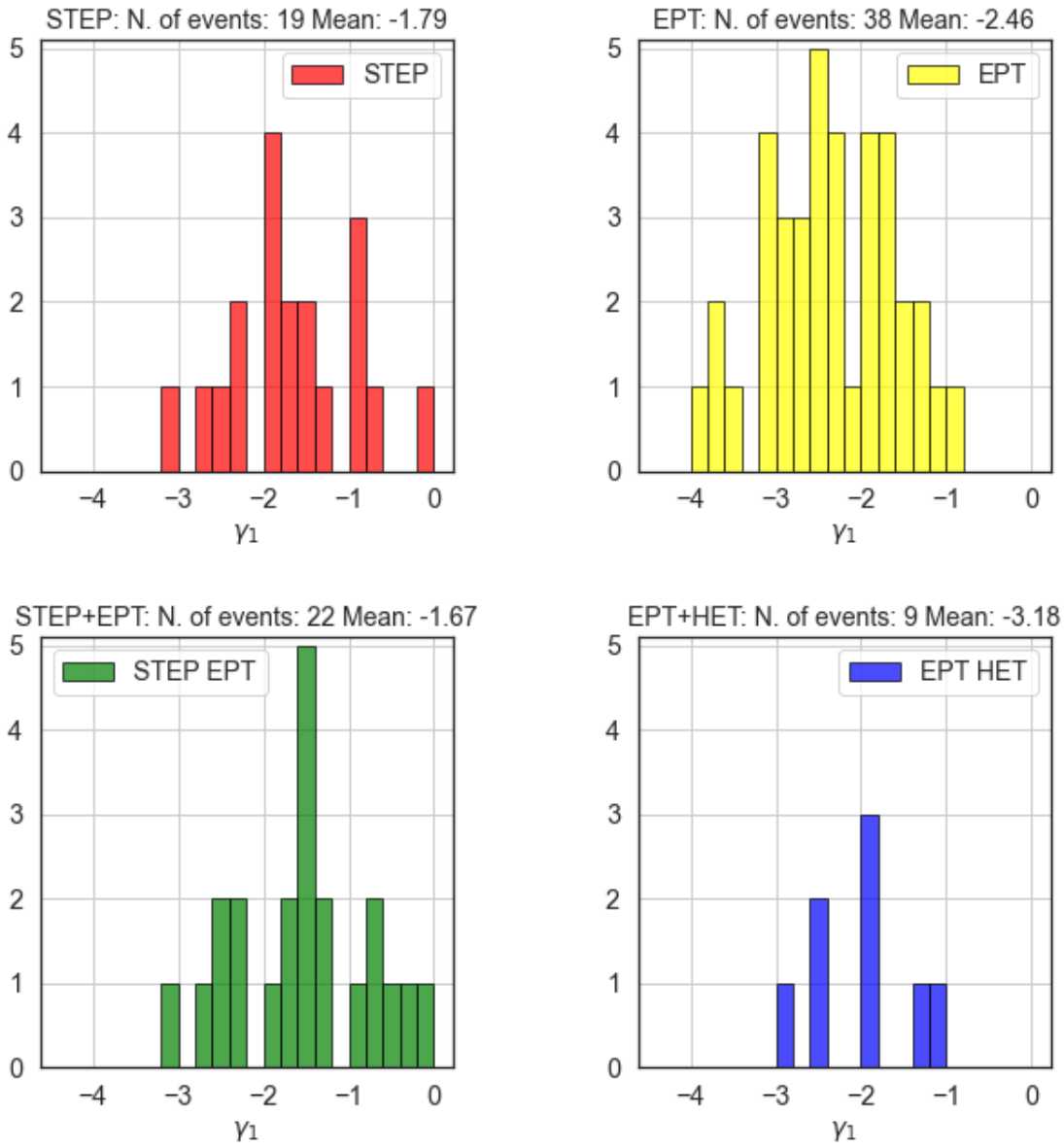

Figure 38. Distribution of the spectral index γ_1. Top left panel: fit to STEP data. Top right panel: fit to EPT data. Bottom left panel: fit to STEP+EPT data. Bottom right panel: fit to EPT+HET data.

Figure 39 shows the distribution of the spectral index γ_1 for all events that were best described by a broken power-law fit or a broken power-law fit with an exponential cutoff. The top left panel shows the distribution found in fits to STEP data, the bottom left panel shows the distribution of the values for a fit to STEP+EPT data, the top right panel shows the distribution of the values for a fit to only EPT data and the bottom right panel shows the distribution of the values for a fit to EPT+HET data. Above each panel we also indicate the mean value found for each fit as well as the number of events fit with the specific combination of instruments corresponding to the panel.

Figure 40 shows the distribution of the spectral index γ_1 for all events that were best described by a single power-law fit. The panel on the left shows the distribution found in fits to STEP data, while the panel on the right shows the distribution of the values for a fit to EPT data. The other combinations of instruments did not show any single power-law fit. Above each panel we also indicate the mean value found for each fit as well as the number of events fit with the specific combination of instruments corresponding to the panel.

Figure 41 shows the distribution of the spectral index γ_2 for all events that were best described by a broken power-law fit or a broken power-law fit with an exponential cutoff. The top left panel shows the distribution found in fits to STEP data, the bottom left panel shows the distribution of the values for a fit to STEP+EPT data, the top right panel shows the distribution of the values for a fit to only EPT data and the bottom right panel shows the distribution of the values for a fit to EPT+HET data. Above each panel we also indicate the mean value found for each fit as well as the number of events fit with the specific combination of instruments corresponding to the panel.

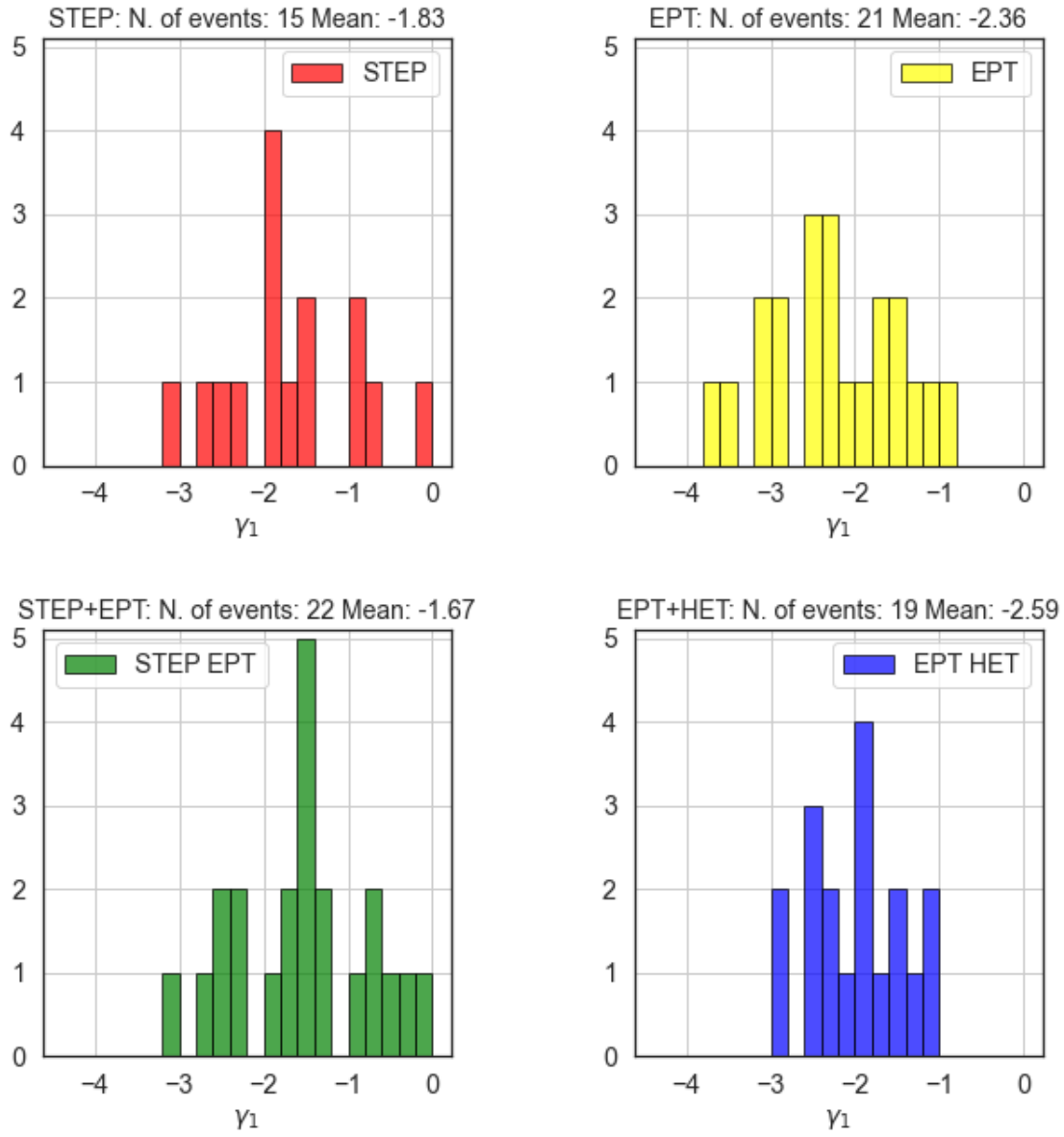

Figure 39. Distribution of the spectral index γ_1 to fits with a broken power-law or broke power-law+cutoff. Top left panel: fit to STEP data. Top right panel: fit to EPT data. Bottom left panel: fit to STEP+EPT data. Bottom right panel: fit to EPT+HET data.

Figure 42 shows the distribution of α, which describes the sharpness on the break. As we can see from the histograms, the values are scattered anywhere between 0 and 500. It is clear that α has no clear distribution, but it is rather just a numerical value.

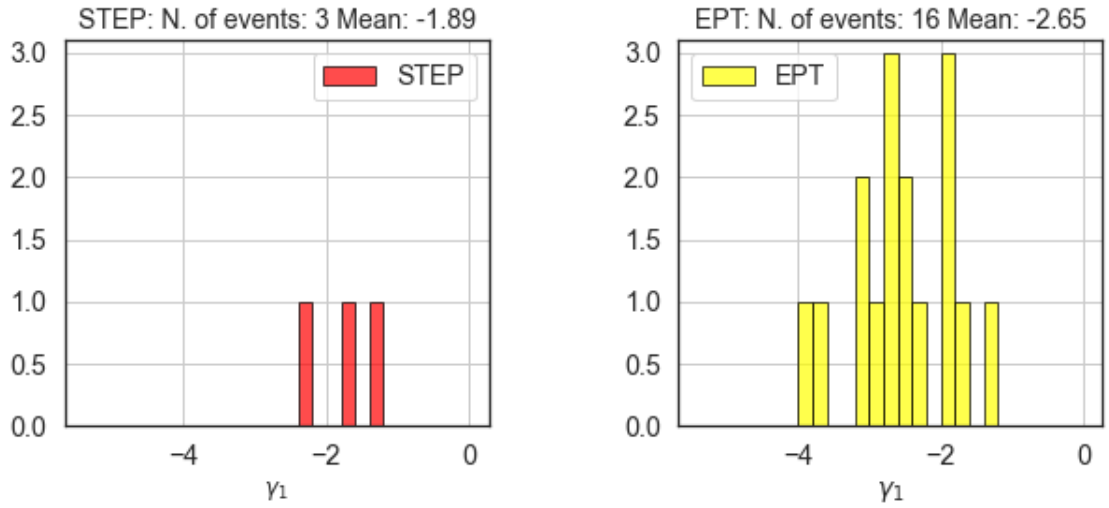

Figure 40. Distribution of the spectral index γ_1 to fits with a single power-law. Right panel: fit to EPT data. Left panel: fit to STEP data.

We also checked for a correlation between the spectral indices γ_1 and γ_2 with the break energies and the intensity at 0.1 MeV, which is calculated during the fitting process automatically. Figure 43 shows the correlation between the spectral index γ_1 and the break energy. Figure 44 shows the correlation between the spectral index γ_2 and the break energy. Figure 45 shows the correlation between the spectral index γ_1 and the intensity at 0.1 MeV. Figure 46 shows the correlation between the spectral index γ_2 and the intensity at 0.1 MeV. In all the figures the top left panel shows the correlation found in fits to STEP data, the bottom left panel shows the correlation of the values for a fit to STEP+EPT data, the top right panel shows the correlation of the values for a fit to only EPT data and the bottom right panel shows the correlation of the values for a fit to EPT+HET data. Above each panel we also indicate the number of events fit with the specific combination of instruments corresponding to the panel. Neither one of the spectral indices showed any correlation to the break energy nor the intensity.

From the bottom left panel of Figure 43 it looks like we can identify different distributions of breaks in the STEP+EPT fits. In top left panel, showing the values for STEP fits only, we see a dependence between E_b and γ_1, but not in the top right

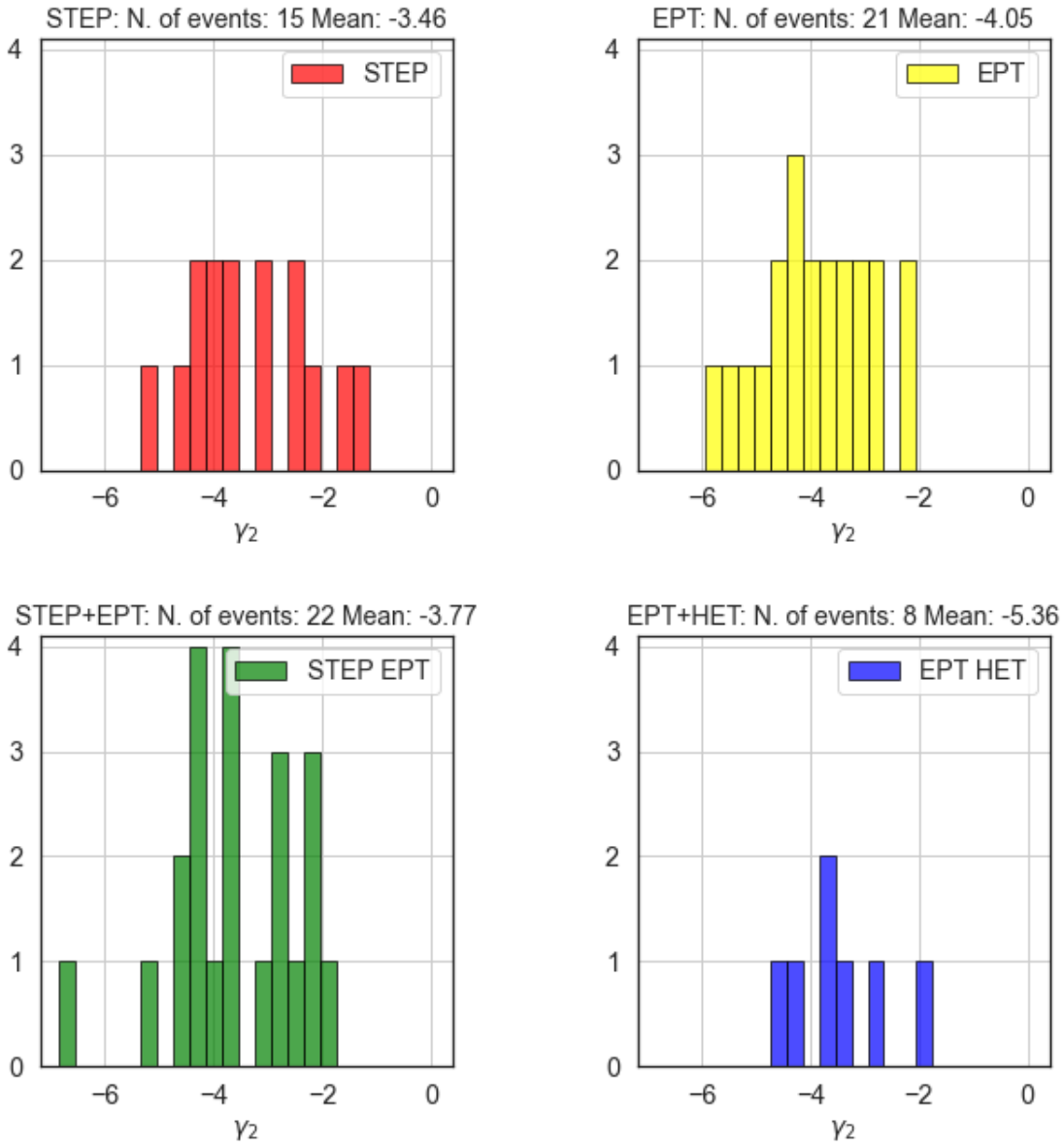

Figure 41. Distribution of the spectral index γ_2. Top left panel: fit to STEP data. Top right panel: fit to EPT data. Bottom left panel: fit to STEP+EPT data. Bottom right panel: fit to EPT+HET data.

panel showing EPT only fits. This could again point towards the different kinds of breaks we found.

In Figures 45 and 46 we see that the data seems to be randomly scattered above 100 /(s cm^2 sr MeV). Only the top right panel in Figure 45, which shows the spectral index γ_1 vs the intensity at 0.1 MeV for fits to EPT data, seems to have a positive correlation to the intensity. This is however only seen until $\sim$ 100 /(s cm^2

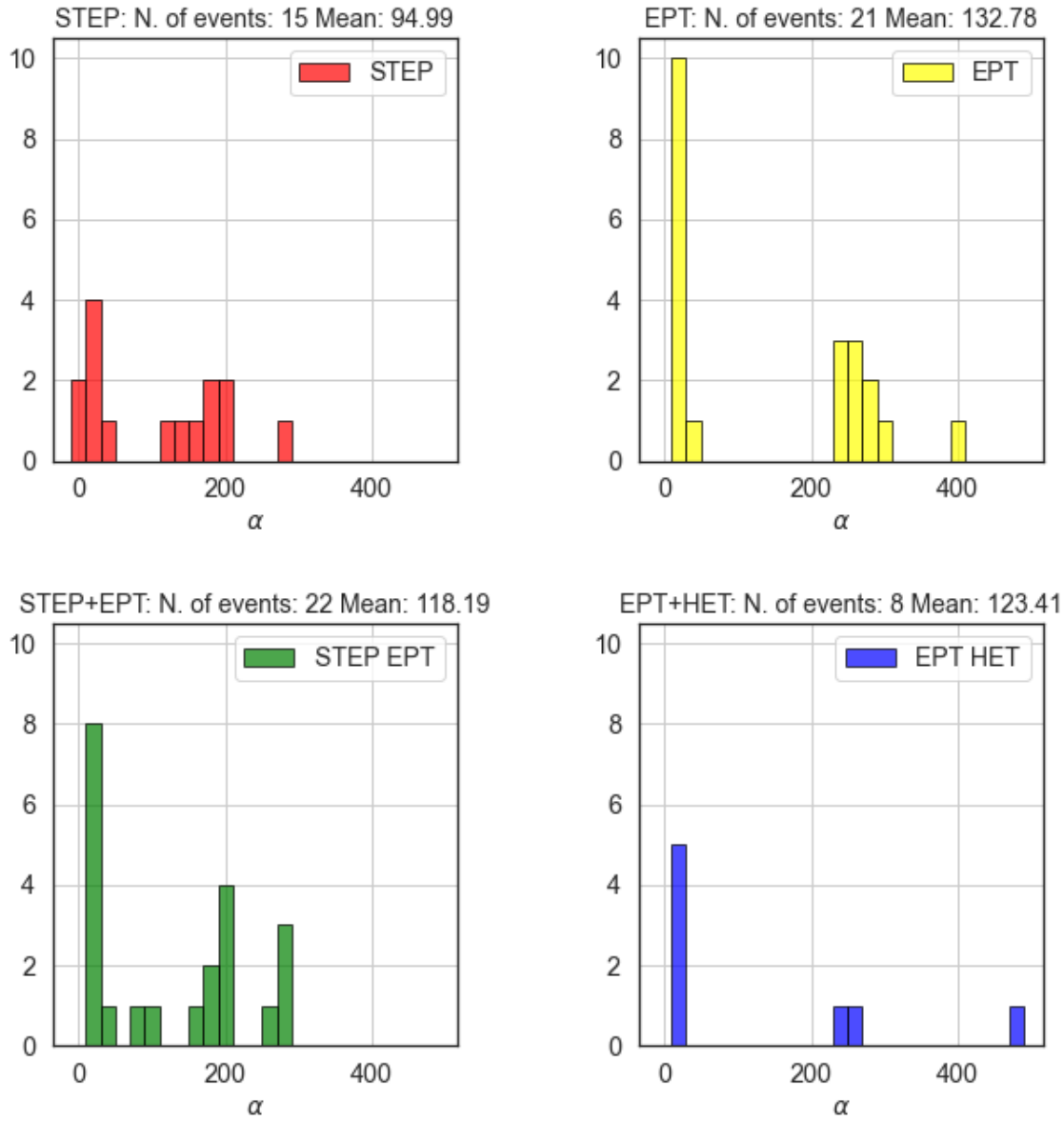

Figure 42. Distribution of α, which represents the sharpness of the break. Top left panel: fit to STEP data. Top right panel: fit to EPT data. Bottom left panel: fit to STEP+EPT data. Bottom right panel: fit to EPT+HET data.

sr MeV), after which the data points are randomly scattered. So, there seem to be two separate particle distributions. The limit of $\sim$ 100 /(s cm^2 sr MeV) most likely comes from the fact that, in order to measure a harder spectrum, we also require a higher intensity otherwise the data would fall behind the background. The first particle distribution above 100 /(s cm^2 sr MeV) has a high enough intensity that this does not matter. The second distribution below 100 /(s cm^2 sr MeV) might be

the part of the spectrum where the intensity at the reference energy of 0.1 MeV falls already into the part of the spectrum corresponding to γ_2, with a softer spectrum.

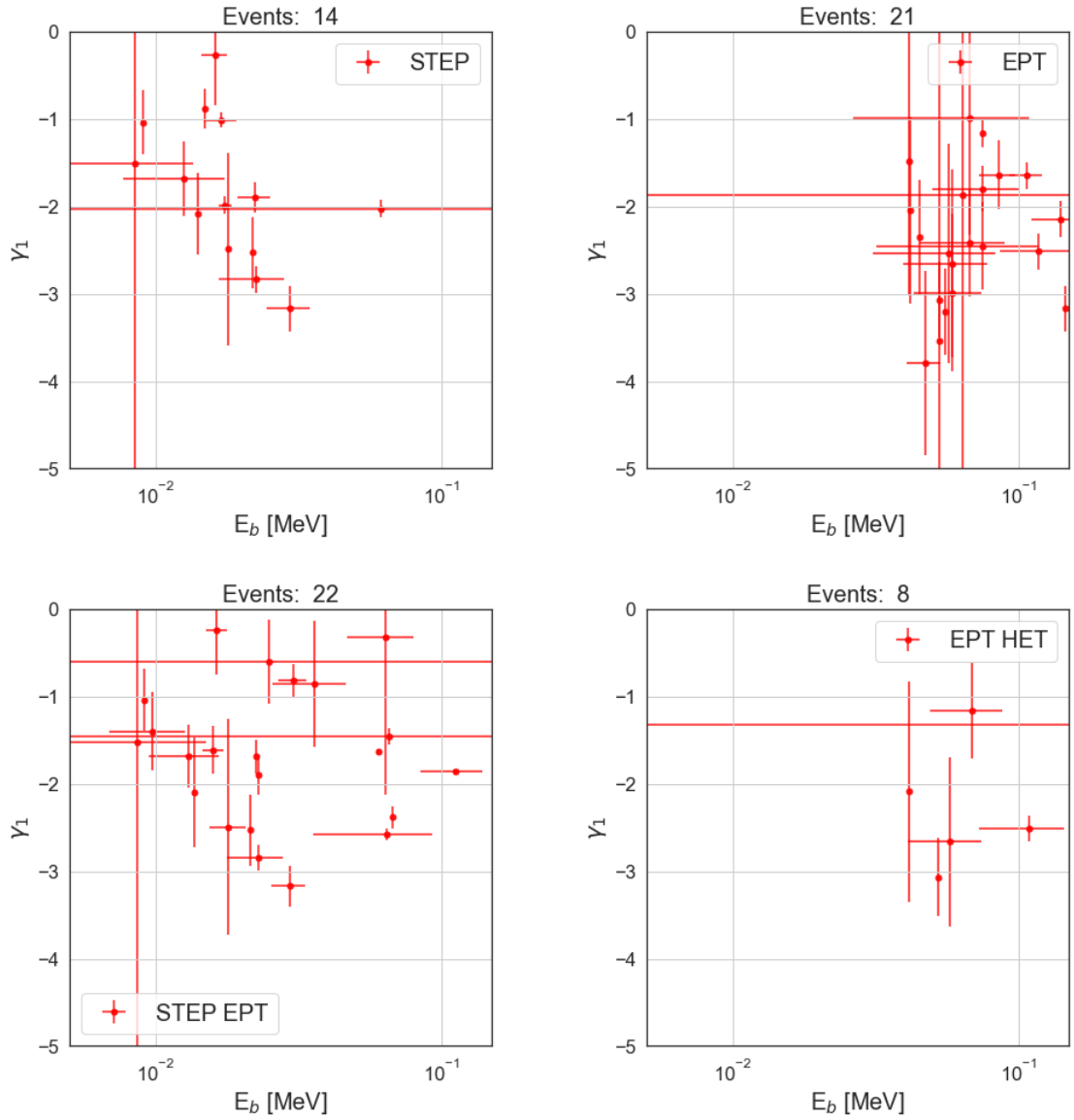

Figure 43. The Figure shows the spectral break energy vs the spectral index γ_1. Top left panel: fit to STEP data. Top right panel: fit to EPT data. Bottom left panel: fit to STEP+EPT data. Bottom right panel: fit to EPT+HET data.

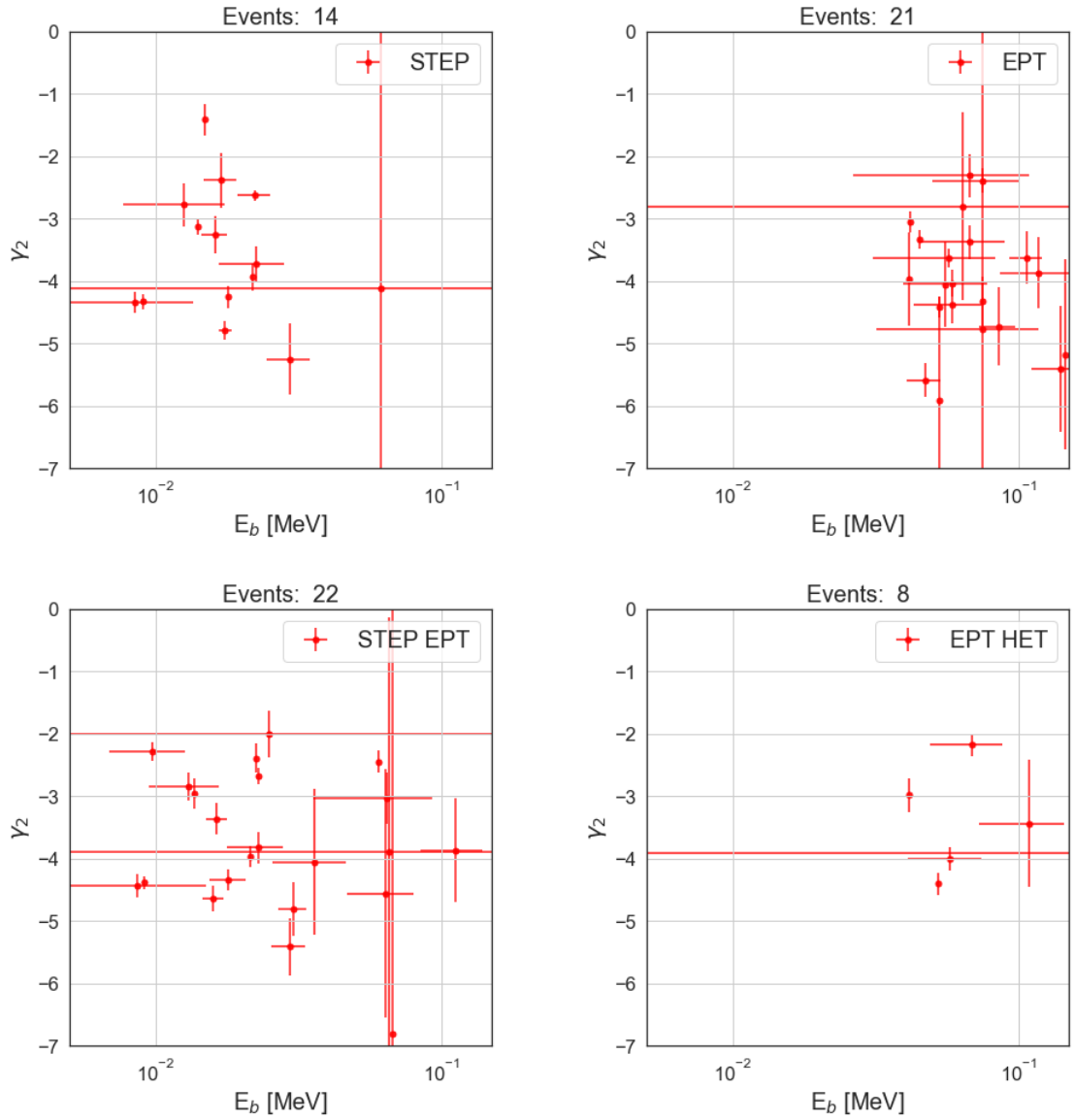

Figure 44. The Figure shows the spectral break energy vs the spectral index γ_2. Top left panel: fit to STEP data. Top right panel: fit to EPT data. Bottom left panel: fit to STEP+EPT data. Bottom right panel: fit to EPT+HET data.

Figure 47 shows the correlation between the two spectral indices for the fits to different instruments: STEP (top left panel), STEP+EPT (lower left panel), EPT (top right panel) and EPT+HET (lower right panel). ρ is the Spearman correlation coefficient (Spearman ρ) calculated with a Monte Carlo method. The Spearman correlation coefficient is usually calculated without taking into account the uncertainties. To get a more accurate description of the correlation between

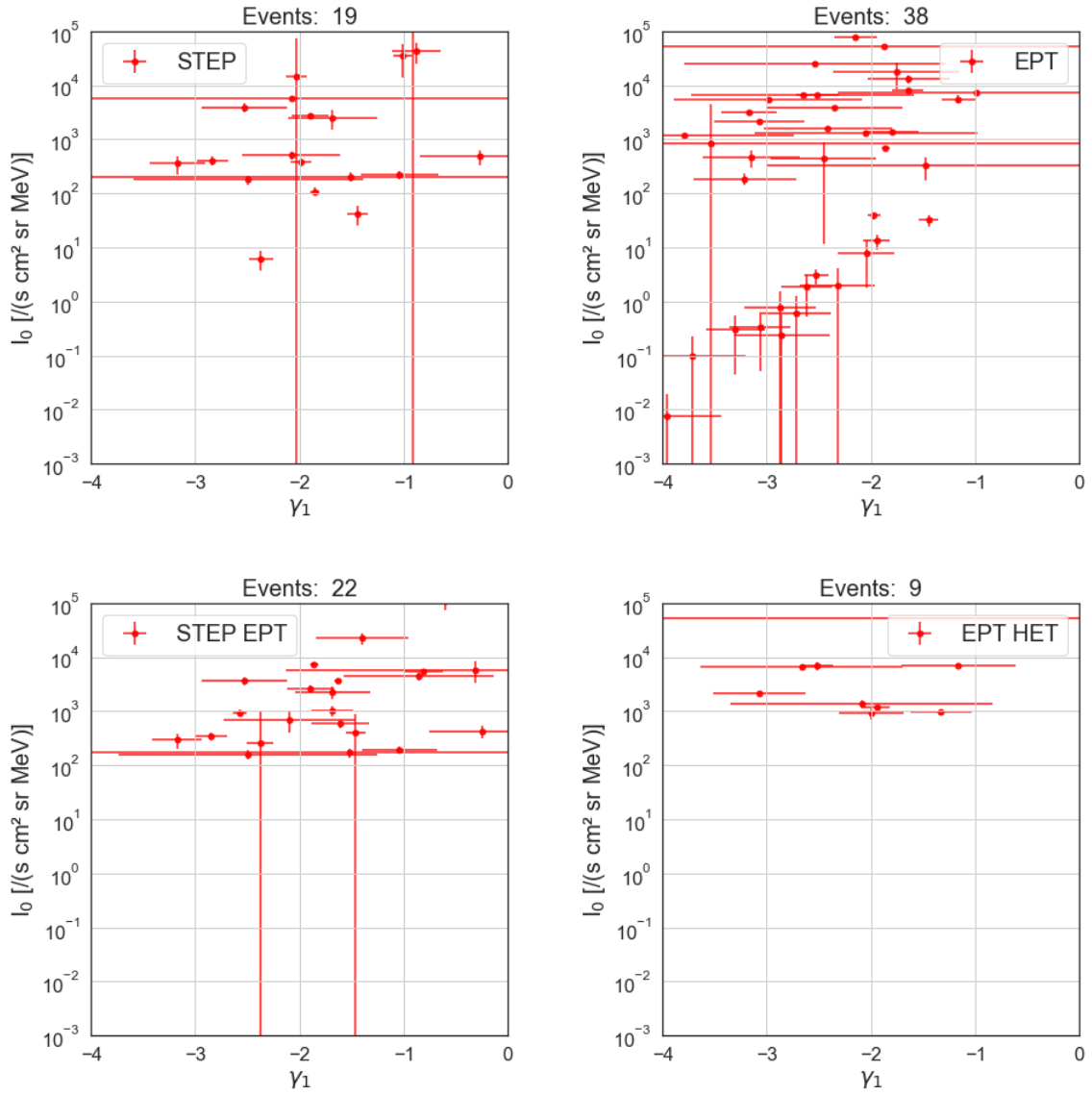

Figure 45. The Figure shows the intensity at 0.1 MeV vs the spectral index γ_1. Top left panel: fit to STEP data. Top right panel: fit to EPT data. Bottom left panel: fit to STEP+EPT data. Bottom right panel: fit to EPT+HET data.

two parameters, given that we sometimes have large uncertainties, we use a Monte Carlo method to take the uncertainties into account. This is done by choosing a value for each parameter randomly within their uncertainty range and by calculating the correlation coefficient by iterating through these values multiple times, in our case 10000 iterations.

From literature (e.g. Strauss et al., 2020), we know that there should be correlation between the two spectral indices, however, from Figure 47 and the values of

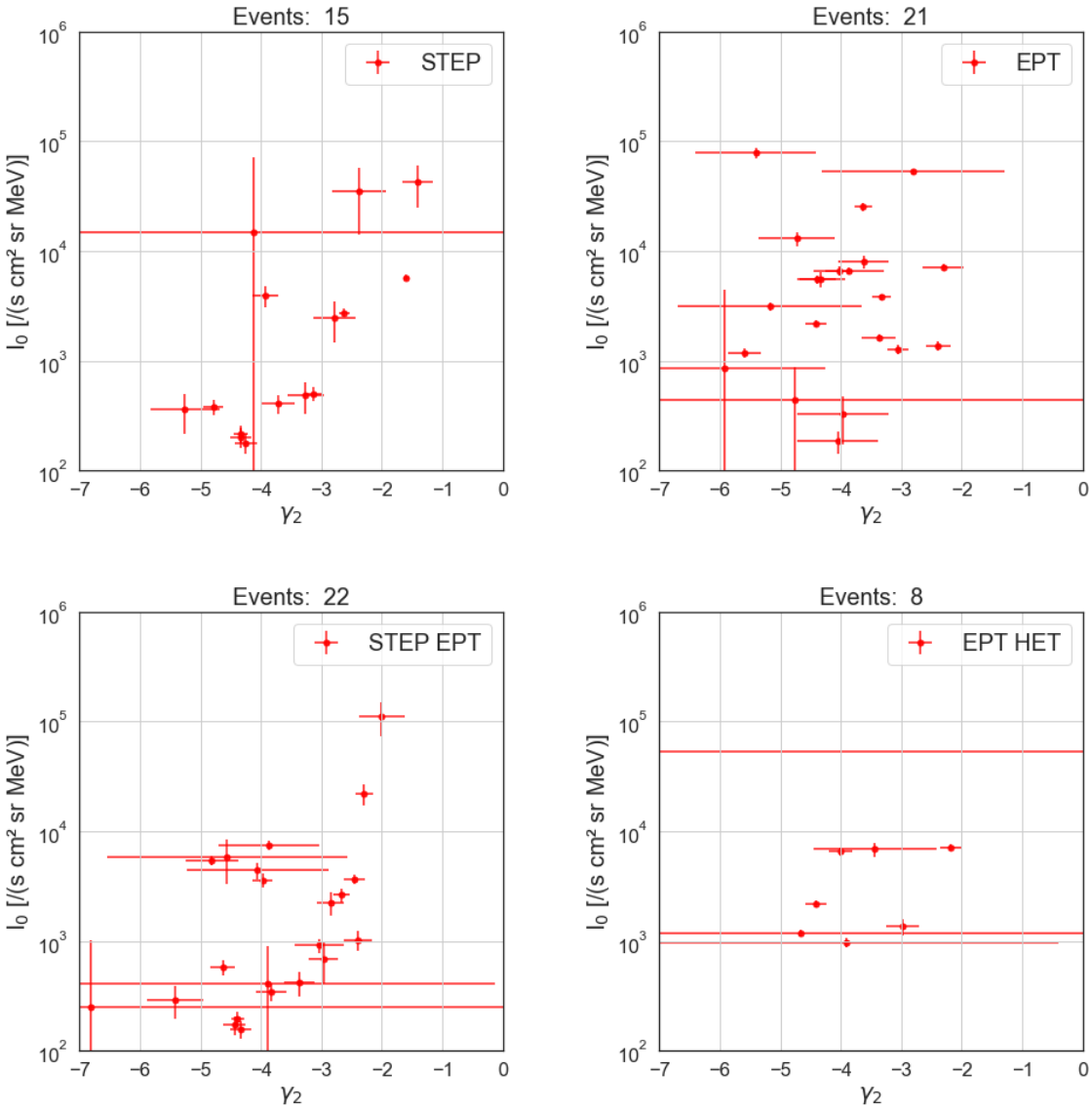

Figure 46. The Figure shows the intensity at 0.1 MeV vs the spectral index γ_2. Top left panel: fit to STEP data. Top right panel: fit to EPT data. Bottom left panel: fit to STEP+EPT data. Bottom right panel: fit to EPT+HET data.

ρ in the legends we do not see any correlation. We consider a coefficient of over 0.6 within the error bars to be significant.

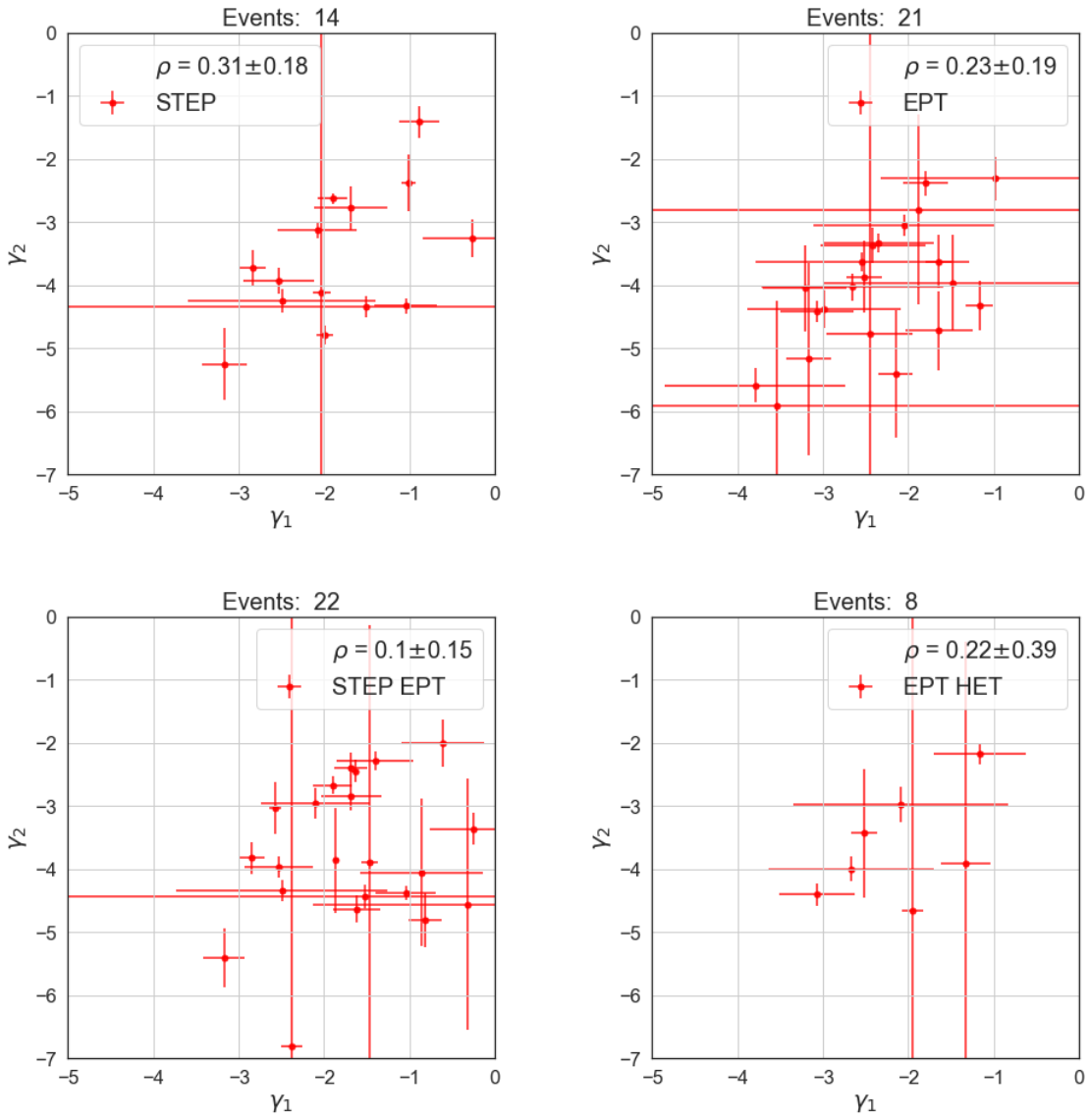

Figure 47. The Figure shows the correlation between the spectral indices γ_1 and γ_2 for the fits to different combinations of instruments: STEP (top left panel), STEP+EPT (lower left panel), EPT (top right panel) and EPT+HET (lower right panel). ρ is the Spearman correlation coefficient calculated with a montecarlo method.